A JAK/STAT-Pdk1-S6K axis bypasses systemic growth restrictions to promote regeneration

Ananthakrishnan Vijayakumar Maya [1,2,3], Lena Neuhaus [4,5], Liyne Nogay [1,2,3], Aakriti Singh[1,2,3], Lara Heckmann [1, 2, 3], Isabelle Grass [1, 2], Jörg Büscher [6], Katrin Kierdorf [4,5], Anne-Kathrin Classen [1, 2, 5, 7] *

* Corresponding author: anne.classen@biologie.uni-freiburg.de

1 Hilde-Mangold-Haus, University of Freiburg, Freiburg, Germany
2 Faculty of Biology, University of Freiburg, Freiburg, Germany
3 International Max Planck Research School for Epigenetics, Biophysics and Metabolism, Freiburg, Germany
4 Spemann Graduate School of Biology and Medicine (SGBM), University of Freiburg, Freiburg, Germany
5 Institute of Neuropathology, Faculty of Medicine, University of Freiburg, Freiburg, Germany
6 Max Planck Institute of Immunobiology and Epigenetics, Freiburg, Germany
7 Signaling Research Centres BIOSS and CIBSS, University of Freiburg, Germany

Abstract

Inflammation triggers systemic signals that induce growth restrictions in distant organs, a process well characterized in tumor cachexia. While mechanisms allowing tumors to circumvent these systemic growth restrictions have been established, the physiological processes that overcome inflammation-induced growth restrictions during regeneration remain largely unexplored. In our study, we use a model of tissue inflammation and regeneration in developing *Drosophila* imaginal discs to dissect key metabolic and signaling adaptations that, in physiological settings, both induce and overcome systemic growth restrictions. We find that expression of *eiger*, the *Drosophila* TNF-α homolog, induces systemic insulin restriction, as evidenced by reduced expression of *dILP2* and *dILP5*, as well as elevated nuclear dFOXO, and reduced protein translation and proliferation in peripheral tissues. Proliferating cells overcome systemic insulin restriction by upregulating Pdk1, which is both necessary and sufficient to promote phosphorylation of ribosomal protein S6 and protein translation via an Insulin/Akt-independent mechanism. We further demonstrate that JAK/STAT signaling acts upstream to increase Pdk1 levels, delineating a novel JAK/STAT-Pdk1-S6K axis essential for regenerative proliferation. The upregulation of amino acid transporters in the proliferative domain further suggests that regenerating cells preferentially import amino acids, fueling mTORC1 activation. Similar metabolic signatures are observed in a *Drosophila* Ras^{V12}, *scrib* tumor model, suggesting that tumors may co-opt these metabolic pathways to sustain growth in an insulin-restricted environment. Our findings reveal a specialized metabolic program that integrates systemic nutrient mobilization with local metabolic reprogramming, with important implications for understanding of physiological tissue repair but also pathologies such as chronic wounds and cancer.

Introduction

Tissue damage and inflammation trigger a dynamic interplay between cellular signals and cell behaviors to promote repair and regeneration. Proper orchestration of these responses is crucial, as failure can lead to chronic wound healing pathologies or diseases like cancer (Eming et al, 2017; Huang et al, 2022; MacCarthy-Morrogh & Martin, 2020; Pena & Martin, 2024; Rybinski et al, 2014). To better understand these diseases, a wide range of recent studies aim to dissect the pathological reprogramming of relevant metabolic circuits (Martinez-Reyes & Chandel, 2021; Stine et al, 2022; Wong & Verheyen, 2021). However, a surprising gap exists in our knowledge about the precise metabolic adaptations employed by the normal physiological programs of tissue repair and regeneration (Eming et al, 2021; Eming et al, 2017; Meacham et al, 2022; Zhu & Thompson, 2019). With this study, we aim to provide insight into the local and systemic metabolic adaptations during physiological tissue repair and regeneration.

Central to both metabolism and cellular growth are the Insulin/PI3K/Akt and mTORC1 signaling pathways, which are evolutionarily conserved from invertebrates to vertebrates. Both pathways converge on their shared effector ribosomal protein S6 kinase (S6K), which drives protein synthesis and cellular growth by activating protein translation. The Insulin/PI3K/Akt signaling branch is activated by binding of Insulin to its receptor, stimulating Phosphoinositide-3-kinase (PI3K) to produce Phosphatidylinositol (3,4,5)-trisphosphate (PIP3). PIP3 recruits Phosphoinositide-dependent kinase 1 (Pdk1) and activates Akt, which inhibits nuclear translocation of the transcription factor FOXO. Pdk1 phosphorylates S6K, initiating its activation, whereas optimal S6K activity requires an additional phosphorylation by mTORC1
(Holz et al, 2005; Hopkins et al, 2020; Hoxhaj & Manning, 2020; Manning & Cantley, 2007; Wu et al, 2022). mTORC1 specifically responds to amino acid availability and is therefore central to anabolic growth (Saxton & Sabatini, 2017). While previous studies implicate a role for Insulin/PI3K/Akt and mTORC1 signaling in tissue repair processes, the precise metabolic adaptations remain to be investigated (Kakanj et al, 2016; Nakamura et al, 2020; Ring et al, 2023; Wei et al, 2019).

Drosophila models have advanced our understanding of tissue repair, regeneration and metabolism (Fox et al, 2020; Worley & Hariharan, 2022). Specifically, studies in developing imaginal discs or the adult gut have highlighted the role of two key signaling pathways - JNK/AP1 and JAK/STAT - in repair and proliferation. These pathways coordinate a range of responses, from senescent-like cell cycle arrest in damaged cells to compensatory proliferation in adjacent cells (Cosolo et al, 2019; Floc'hlay et al, 2023; Jaiswal et al, 2023; Nakamura et al, 2020; Pena & Martin, 2024; Stevens & Page-McCaw, 2012). Importantly, arrested, JNK- signaling cells produce Unpaired (Upd) cytokines, which activate JAK/STAT signaling in in surrounding cells at the site of inflammatory damage, promoting survival and rapid regenerative proliferation (Crucianelli et al, 2022; Floc'hlay et al, 2023; Herrera & Bach, 2019; Herrera et al, 2013; Jaiswal et al, 2023; La Fortezza et al, 2016; Santabarbara-Ruiz et al, 2015; Sustar et al, 2011; Worley et al, 2022). The distinct functional demands of senescent and rapidly proliferating

84 cells raise the question about how these distinct cell populations metabolically adapt to successfully
85 support tissue repair.
86
87 Tissue repair and tumor development share striking similarities; in fact, tumors have long been
88 compared to non-healing wounds (Dvorak, 1986). Accordingly, *Drosophila* tumor models activate
89 JNK/AP1 and JAK/STAT signaling, which promote tumor progression (Enomoto & Igaki, 2022; Herrera
90 & Bach, 2019; La Marca & Richardson, 2020). To support their growth, tumors secrete signaling
91 molecules that initiate inter-organ signaling and systemic metabolic responses (Bilder et al, 2021;
92 Hodgson et al, 2021; Liu et al, 2022). For instance, the Insulin-like peptide 8 (Dilp8), when secreted
93 by tumors, disrupts hormone balance by reducing Ecdysone and Insulin production through direct
94 effects on the ring gland and Insulin-producing cells (IPCs), with the effect of halting developmental
95 progression of the tumor-bearing host (Colombani et al, 2012; Garelli et al, 2012). Other cytokines,
96 such as Ecdysone-inducible gene L2 (ImpL2), or the TNFα homologue Eiger (Egr), directly or indirectly
97 trigger lipolysis and proteolysis to promote nutrient release from muscles as well as the fat body, an
98 adipose tissue central for nutrient storage and energy homeostasis (Agrawal et al, 2016; Ding et al,
99 2021; Figueroa-Clarevega & Bilder, 2015; Gutierrez et al, 2007; Hodgson et al, 2021; Lodge et al,
100 2021; Rajan & Perrimon, 2012; Romao et al, 2021; Song et al, 2019). Amino acids or sugars are
101 released in this manner and subsequently absorbed by tumors and facilitate their anabolic growth
102 (Cong et al, 2021; Khezri et al, 2021; Newton et al, 2020). This inter-organ signaling network and
103 metabolic state resembles cachexia, a clinical syndrome characterized by weight loss, muscle atrophy
104 and fatigue, typically observed in chronic inflammatory conditions, including cancer (Argiles et al, 2014;
105 Bilder et al, 2021; Hodgson et al, 2021; Liu et al, 2022; Setiawan et al, 2023). While these studies
106 reveal oncogenic metabolic signaling networks, the metabolic signaling networks employed during
107 physiological tissue repair and regeneration remain poorly understood. Previous studies demonstrate
108 that systemically acting cytokines may also be released upon tissue damage in the absence of
109 oncogenic transformation (Colombani et al, 2012; Garelli et al, 2012; Gontijo & Garelli, 2018; Hackney
110 & Cherbas, 2014; Halme et al, 2010; Sun & Poss, 2023), and fat body break-down changing
111 Methionine, S-adenosylmethionine and Kynurenine metabolism promotes imaginal disc regeneration
112 (Kashio & Miura, 2020; Kashio et al, 2016). However, the integration of local and systemic metabolic
113 adaptations promoting physiological repair and regeneration remain poorly characterized. In our study
114 we combine genetic analysis, quantitative imaging, untargeted metabolomics and information from
115 single-cell RNA sequencing data to outline the local and systemic adaptations that selectively support
116 fast-proliferating cells during regeneration through an Insulin-independent JAK/STAT-Pdk1-S6K
117 signaling axis.
118
119 **Results**
120
121 **(1) Proliferating cells maintain high levels of protein translation during regeneration**
122 To induce regeneration, we expressed the *Drosophila* homologue of TNF-α, known as Eiger (Egr), for
123 a 24 h period within the imaginal wing pouch using the *rn-GAL4* driver (Smith-Bolton et al, 2009). As

124 expected, *egr*-expression caused significant cell death, accompanied by the activation of the JNK/AP-
125 1 activity reporter TRE-RFP (**Fig 1A-C; Fig S1A,B**) (Chatterjee & Bohmann, 2012; Cosolo et al, 2019;
126 Jaiswal et al, 2023; La Fortezza et al, 2016). The central disc region with high JNK signaling exhibited
127 markers of cellular senescence, including increased senescence-associated β-galactosidase activity
128 (**Fig. S1C,D**), upregulation of the matrix metalloprotease MMP-1 and cytokines of the Upd family, as
129 well as a JNK-signaling induced cell cycle arrest in G2 (Cosolo et al, 2019; Floc'hlay et al, 2023; Harris
130 et al, 2020; Jaiswal et al, 2023; Worley et al, 2018; Worley et al, 2022). In contrast, cells within 40 µm
131 surrounding this central JNK signaling domain were highly proliferative, as detected by EdU
132 incorporation (**Fig 1A,B,D**) (Crucianelli et al, 2022; Smith-Bolton et al, 2009). To facilitate quantification
133 of cell behaviors and account for disc size variation, we defined a conservative 20µm band outside the
134 high JNK signaling domain as the 'proliferative domain' (PD^{egr}) for the remainder of this study.
135
136 How do these proliferating cells meet their metabolic needs? To answer this question, we monitored
137 protein translation using O-propargyl-puromycin (OPP)-incorporation assays (Aviner, 2020). This
138 assay revealed uniform levels of protein synthesis throughout control wing imaginal discs. In *egr*-
139 expressing discs, protein synthesis in the proliferative and the JNK signaling domains proceeded at
140 levels similar to control discs (**Fig 1E-G**). Interestingly, the notum of *egr*-expressing discs exhibited a
141 significant decrease in OPP incorporation, which correlated with a marked reduction in EdU
142 incorporation (**Fig 1G-M**). The contrasting levels of protein synthesis, proliferation and signaling
143 between different regions reveal that inflammatory damage induces at least three distinct cell
144 populations with different cellular programs: 1) a senescent cell population exhibiting high protein
145 synthesis and JNK/AP-1 activity; 2) an cycling cell population exhibiting high protein synthesis and low
146 JNK/AP-1 activation; and 3) notum cells exhibiting low protein synthesis, low JNK/AP-1 activity and
147 slow cell cycling (**Fig 1N**). While these observations mirror proliferation dynamics visualized in earlier
148 studies (Smith-Bolton et al, 2009; Sustar et al, 2011; Sustar & Schubiger, 2005), we wanted to better
149 understand how these differences reflect a need to integrate local and systemic metabolic demands
150 during regeneration.
151
152 **(2) Tissue damage induces systemic insulin restriction**
153 A reduction in protein translation rates in peripheral tissue domains like the notum suggested that
154 insulin signaling, normally supporting protein translation through S6K activation, is reduced. Notably,
155 cells with active JNK signaling express high levels of Dilp8, a known antagonists of insulin production
156 by insulin-producing cells (IPCs) in the larval brain (**Fig 2A,B**) (Garelli et al, 2012; Vallejo et al, 2015).
157 Expression of *eiger* could thus limit anabolic growth despite nutrient intake by feeding (Agrawal et al,
158 2016; Figueroa-Clarevega & Bilder, 2015; Gontijo & Garelli, 2018; Ingaramo et al, 2020; Rajan &
159 Perrimon, 2012; Vallejo et al, 2015; Wang et al, 2005). To determine if *egr*-expressing larvae indeed
160 restrict Insulin expression, we analyzed the expression of the *Drosophila* Insulin-like peptides *dILP2*
161 and *dILP5* (Semaniuk et al, 2020). We found that *dILP2* and *dILP5 expression* was significantly
162 reduced in *egr*-expressing larvae, and approached levels seen in larvae starved for 24 h (**Fig 2C**), a

condition known to reduce insulin expression due nutrient limitation (Semaniuk et al, 2020; Sudhakar et al, 2020).

To understand if this reduction in *dILP2* and *dILP5* expression correlates with reduced Insulin signaling in peripheral tissues, we examined nuclear localization of the dFOXO, a key downstream effector of canonical Insulin signaling (Hoxhaj & Manning, 2020; Manning & Toker, 2017). We observed elevated nuclear dFOXO in the notum of *egr*-expressing discs (**Fig 2D-F**), demonstrating that reduced *dILP2* and *dILP5* expression correlated with systemic attenuation of insulin signaling. This attenuation would explain the low rates of protein translation observed in the notum. In support of this conclusion, we found that low rates of protein translation in nota did not correlate with activation of JNK stress signaling or apoptosis, indicating that low Insulin signaling likely causes the observed reduction in protein synthesis (**Fig S2A,B**). Importantly, this systemic reduction in protein translation was also evident in other imaginal discs, such as the leg and the eye, and this effect was robustly reproduced by *eiger* expressed under the more restricted spatial pattern of *salm-GAL4* (**Fig 2G-T, Fig S2C-K**). In all cases, the reduction in translational capacity correlated with decreased proliferation, with the developing eye showing reduced EdU incorporation overall and in the second mitotic wave, specifically (**Fig S2H,I**). Taken together, these findings reveal a widespread decline in cell proliferation and protein synthesis in *egr*-expressing larvae, which correlates with restricted Insulin production and signaling (**Fig 2U**). These observations are consistent with previous reports of reduced disc sizes following other types of tissues damage and resemble systemic changes induced by inflammatory tumors (Boulan et al, 2019; Ding et al, 2021; Figueroa-Clarevega & Bilder, 2015; Garelli et al, 2012; Hodgson et al, 2021; Jiang et al, 2022; Khezri et al, 2021; Lodge et al, 2021; Smith-Bolton et al, 2009; Song et al, 2019; Sustar & Schubiger, 2005).

(3) Regenerative proliferation is supported by fat body catabolism, amino acid importers and TOR signaling

How can the proliferative domain maintain high rates of protein translation and proliferation in a systemic environment that does not rely on Insulin signaling? In this environment proliferating cells must solve two problems: (1) They must obtain and take up the right nutrients and (2) they must drive protein translation and growth under Insulin-limiting conditions. To address the first question, we investigated if *egr*-driven Insulin restriction may induce nutrient release from the fat body, the largest nutrient storage organ in larvae. Previous studies have shown that fat body breakdown provides nutrients for tumor growth, thereby revealing an ancient program of nutrient supply under inflammatory conditions (Ding et al, 2021; Figueroa-Clarevega & Bilder, 2015; Katheder & Rusten, 2017; Khezri et al, 2021; Lodge et al, 2021; Newton et al, 2020; Song et al, 2019). To understand if similar catabolic changes may be induced in *egr*-expressing larvae, we employed Nile Red staining to visualize lipid droplets within the fat body. We observed morphological changes, such as increased droplet size and 'roundness' (defined as the relationship between area and length of major axis), consistent with molecular changes associated with lipid mobilization (**Fig 3A-C, Fig S3.1 A**) (Beller et al, 2010;

203 Figueroa-Clarevega & Bilder, 2015; Gutierrez et al, 2007; Lodge et al, 2021; Ugrankar et al, 2019).
204 Correspondingly, fat bodies of these larvae exhibited a significant decrease in triglyceride content,
205 similarly to fat bodies from starved larvae (**Fig 3D,E**). Moreover, we find that levels of total and
206 activated p-Akt in fat body from *egr*-expressing larvae were reduced, similar to insulin restriction
207 observed in starved larvae (**Fig S3.1B**). Additionally, levels of nuclear dFOXO-GFP were elevated
208 (**Fig. S3.1 C-E**), supporting the notion that *egr*-induced insulin restriction reduces systemic Insulin
209 signaling and promotes a catabolic fat body state**.**
210
211 Notably, JNK-signaling cells in *egr*-expressing discs also express *ImpL2*, *upd2* and *upd3*, factors
212 previously implicated in fat body break-down during tumor growth in larval and adult hosts (**Fig 3 F-H,**
213 **Fig S3.1 F-H, Fig S3.2**) (Ding et al, 2021; Figueroa-Clarevega & Bilder, 2015; Kwon et al, 2015;
214 Romao et al, 2021). When we ectopically expressed ImpL2 for 24 h using the wing-pouch-specific
215 driver *rn-GAL4*, we found that this was sufficient to induce lipid droplet changes consistent with fat
216 body catabolism (**Fig 3I-K, Fig S3.1 I**). Moreover, *egr*-expressing larvae display activation of
217 JAK/STAT signaling in fat body, which has also been associated with fat body catabolism (**Fig S3.1 J-**
218 **L**) (Ding et al, 2021; Hersperger et al, 2024; Shin et al, 2020). Of note, we did not observe alterations
219 in muscle morphology or evidence of autophagy in imaginal discs, suggesting that these tissues do
220 not serve as a primary source for nutrients after just 24 h of *egr*-expression, different to what is
221 observed in the chronic presence of tumors (**Fig S3.1 M-P**) (Ding et al, 2021; Figueroa-Clarevega &
222 Bilder, 2015; Katheder & Rusten, 2017; Khezri et al, 2021; Lodge et al, 2021; Newton et al, 2020; Song
223 et al, 2019). Combined, we conclude that the combinatorial expression of systemically acting cytokines
224 from JNK-signaling cells in *egr*-expressing discs drives detectable nutrient mobilization from the fat
225 body via multiple pathways.
226
227 To determine if the observed break-down of the fat body could also generate amino acid compounds
228 supporting the high rates of protein translation in the proliferative domain, we performed an untargeted
229 metabolomic analysis of the hemolymph from control and *egr*-expressing larvae. Our results revealed
230 a a shift in the composition of amino acids in in *egr*-expressing larval hemolymph. We observed an
231 enrichment of many amino acids including Leucine, Arginine or Glutamine, which are reported to
232 activate mTORC1 (Lama-Sherpa et al, 2023; Yue et al, 2022). Surprisingly, many come enriched in
233 form of mixed dipeptide species. Furthermore, elevated levels of dipeptide species and free amino
234 acids associated with glutamate metabolism were observed, including increased concentrations of
235 glutamine, glutamate, and glutamyl dipeptides (**Fig 3 L**). Notably, a signature of arginine metabolism
236 emerged, characterized by increased levels of ornithine, N-acetyl-arginine, and aspartate alongside
237 decreased levels of argininosuccinic acid, citrulline, and N-acetyl-ornithine. This altered metabolite
238 profile in the hemolymph represents a flexible supply of building blocks not only for protein synthesis,
239 but also for energy production, co-factor generation, and glutathione-based redox metabolism (Altman
240 et al, 2016; Keshet et al, 2018; Lieu et al, 2020; Marti & Reith, 2021).
241

242 We next examined the ability of proliferating cells to absorb these amino acids. We investigated the
243 expression of solute carrier (SLC) transporters and found that several transcripts were expressed and
244 elevated in *egr*-expressing discs. For instance, *CG15279* (a putative glycine and proline transporter
245 from the SLC6 family), *path* (a potential alanine and glycine transporter from the SLC36 family), *mnd*
246 (an amino acid/polyamine transporter involved in leucine import), and *CG5535* (a putative lysine,
247 arginine, and ornithine transporter from the SLC7 family) were all elevated (**Fig S3.2**). Upregulation of
248 CG5535 was confirmed by immunofluorescence, and we similarly detected increased levels of
249 CG1139 (Arcus), another SLC36 family member that may transport alanine, glycine, and proline (**Fig**
250 **3M-O, Fig S3.1 Q,R**). In addition, a potential sugar transporter, *CG3168* of the SLC22 family, and
251 TRET-1, which is predicted to import trehalose, were strongly upregulated (**Fig S3.1 S-U**) These
252 findings suggest that proliferating cells have an enhanced capacity for importing both amino acids and
253 energy sources.
254
255 One regulatory branch promoting protein translation in response to amino acid availability is mediated
256 by mTORC1 (Jewell et al, 2013; Lama-Sherpa et al, 2023; Liu & Sabatini, 2020; Shimobayashi & Hall,
257 2016; Yue et al, 2022). Moreover, mTORC1 activity itself is promoted by sugar import, boosting ATP
258 production, and hence inhibiting the mTORC1 antagonist AMPK (Jewell et al, 2013; Liu & Sabatini,
259 2020; Shimobayashi & Hall, 2016). The observed upregulation of amino acid and sugar transporters
260 in *egr*-expressing discs could therefore facilitate mTORC1 activation. To demonstrate that the
261 mTORC1 pathway supports protein synthesis during wing disc regeneration, we inhibited mTORC1
262 activity by feeding *egr*-expressing larvae the mTOR inhibitor Rapamycin for 24 h during *egr*-expression
263 (Li et al, 2014; Wu et al, 2022). This treatment resulted in a pronounced reduction in protein synthesis
264 within the proliferative domain of *egr*-expressing discs, demonstrating that mTORC1 activity is
265 essential for protein translation during regeneration, as in wild type control discs (**Fig 3P-R, Fig S3.1**
266 **V,W**). Overall, our data support a model in which fat body catabolism, enhanced amino acid uptake
267 and mTORC1 activation together support the rapid growth and proliferation of the regenerating domain
268 (**Fig 3S**).
269
270 **(4) Pdk1 is upregulated in the proliferating domain**
271 S6K, an important effector of mTORC1, directly activates protein translation (Liu & Sabatini, 2020; Wu
272 et al, 2022). S6K transcripts are upregulated in the wound-associated cell populations of *egr*-
273 expressing discs (**Fig S3.2D**) (Floc'hlay et al, 2023), suggesting that S6K is positively regulated during
274 tissue repair. Importantly, staining for phosphorylated ribosomal S6 (p-S6), a direct target of S6K,
275 revealed that the proliferating domain of *egr*-expressing discs exhibited strongly elevated p-S6 levels
276 (**Fig 4A-C**). However, elevated p-S6 levels cannot be explained solely by mTORC1 activation of S6K
277 because S6K requires co-activation by the Pdk1, a kinase central to canonical Insulin/PI3K signaling
278 (Hopkins et al, 2020; Hoxhaj & Manning, 2020; Wu et al, 2022).
279
280 However, how can proliferating cells promote activation of S6K by Pdk1, considering that *egr*-
281 expressing larvae exhibit insulin restriction? To understand how Pdk1 may be activated, we examined

282 if canonical Insulin/PI3K signaling was active in the proliferating domain of *egr*-expressing discs. We
283 therefore visualized the nuclear localization of dFOXO, the most downstream effector of Insulin/PI3K
284 activity, using two independent GFP-tagged lines. We observed high nuclear levels of dFOXO in the
285 proliferating domain of *egr*-expressing discs, suggesting that Insulin/PI3K signaling there is low, which
286 is consistent with our evidence for systemic Insulin restriction (**Fig 4 D-G, Fig S4A-C**). This conclusion
287 is further supported by unchanged InR levels and even reduced levels of Akt and phosphorylated Akt
288 (P-Akt) in the proliferative domain (**Fig S4D-K**). In contrast, we found that Pdk1 expression is strongly
289 upregulated in the proliferative domain (**Fig 4H-J**) (see Materials & Methods, section *Drosophila*
290 genetics). Similar upregulation of Pdk1 was also observed in other models of tissue damage and
291 regeneration, including those using expression of *hid* or *reaper* to drive cell death. In these models,
292 elevated Pdk1 levels also correlated with high protein translation, demarcating the proliferating
293 domains (**Fig 4K,L, Fig S4L-Q**). In fact, we found that high levels of Pdk1 correlated with high levels
294 of p-S6 staining in *egr*-expressing discs (**Fig 4M,N**). Collectively, these observations suggest that Pdk1
295 levels may play a central role in regenerative proliferation.
296
297 **(5) Pdk1 upregulation is sufficient to drive growth and is necessary for regenerative**
298 **proliferation**
299 To understand if Pdk1 upregulation is a central mechanism driving regenerative proliferation, we
300 expressed either a wild-type or a constitutively active form of Pdk1 in the wing pouch for 24 hours
301 using *rn-GAL4*. Compared to control discs, both forms of Pdk1 resulted in higher levels of protein
302 translation and larger pouch sizes. Larger pouch sizes correlated with more cell proliferation, as EdU
303 incorporation in Pdk1 expressing domains was elevated (**Fig 5 A-F, Fig S5A-D**). These results
304 demonstrate that high Pdk1 levels are sufficient to support a metabolic program characteristic of
305 regenerative proliferation. Notably, the fact that overexpression of a wild-type Pdk1 alone enhances
306 protein synthesis and proliferation, suggests that Pdk1 activity scales with expression levels,
307 functioning independently of other canonical upstream signaling inputs, such as Insulin/PI3K. Of note,
308 Pdk1 can auto-activate via transphosphorylation when recruited to the plasma membrane (Komander
309 et al, 2004; Levina et al, 2022), reflecting potentially Insulin-independent means for Pdk1activation.
310
311 To provide evidence that Pdk1 function is also necessary to support proliferation in *egr*-expressing
312 discs, we genetically reduced Pdk1 function by establishing heterozygosity for a null allele of *Pdk1*
313 (Rintelen et al, 2001). In control discs, this heterozygosity did not affect overall protein synthesis
314 compared to wild type discs, indicating that under normal developmental conditions a single copy of
315 *Pdk1* is sufficient for growth. However, protein synthesis in the proliferating domain of *egr*-expressing
316 discs heterozygous for *Pdk1* was significantly reduced (**Fig 5G-K**). This finding demonstrates that the
317 proliferating domain is particularly sensitive to reductions in Pdk1 levels and underscores the necessity
318 for elevated Pdk1 to support protein synthesis during regeneration. To provide further proof, we
319 expressed a validated RNAi against *Pdk1* specifically in proliferating cells of *egr*-expressing discs
320 under control of the DUAL Control genetic ablation system (**Fig S5E,F**) (Harris et al, 2020). Consistent
321 with our heterozygous mutant results, *Pdk1* knockdown led to a marked decrease in protein translation

322 in the proliferating domain, confirming a cell type specific function for Pdk1 upregulation in the
323 proliferating domain during regeneration (**Fig 5L-N**). Overall, these findings establish that Pdk1
324 upregulation is not only sufficient to drive protein translation and growth but is also critically required
325 to sustain protein translation in the proliferative domain of regenerating imaginal discs under conditions
326 of systemic insulin restriction (**Fig 5O**).
327
328 **(6) Pdk1 is regulated by JAK/STAT signaling**
329 To understand how Pdk1 levels are controlled during regeneration, we examined the role of JAK/STAT
330 signaling, which is activated in the proliferating domain of *egr*-expressing discs to promote cell
331 proliferation and survival (**Fig 6A,B**) (Cosolo et al, 2019; Floc'hlay et al, 2023; Harris et al, 2020;
332 Jaiswal et al, 2023; Worley et al, 2018; Worley et al, 2022). We therefore expressed STAT92E in the
333 posterior compartment of wing imaginal discs, which elevates JAK/STAT signaling, using the *en-GAL4*
334 driver (Jaiswal et al, 2023). This manipulation caused an increase in levels of Pdk1-GFP, phospho-S6
335 and OPP incorporation (**Fig 6C-H, Fig S6C-E**), demonstrating that JAK/STAT activation is sufficient
336 to promote Pdk1 upregulation, S6 activation and protein translation. Conversely, when we expressed
337 a RNAi construct to knock down *STAT92E* in the posterior compartment during normal development,
338 we observed a decrease in both Pdk1-GFP levels and OPP incorporation, suggesting that JAK/STAT
339 activity can limit Pdk1 levels and protein translation (**Fig 6 I-L**). Importantly, the JAK/STAT-Pdk1-
340 S6 axis is also essential for regeneration: we genetically reduced *STAT92E* function in *egr*-expressing
341 discs by establishing heterozygosity for a null allele of *STAT92E* and found that it reduced OPP
342 incorporation specifically in *egr*-expressing discs but not in control discs (**Fig 6M-O, Fig S6F,G**).
343 Moreover, when we expressed a RNAi against *STAT92E* specifically in proliferating cells of *egr*-
344 expressing discs under control of the DUAL Control genetic ablation system (Harris et al, 2020), the
345 elevated protein translation was abrogated (**Fig 6P-R, Fig S6H,I**). Combined, these findings reveal a
346 novel function for JAK/STAT signaling in tissue repair and regeneration by promoting Pdk1
347 upregulation which, together with mTORC1, supports insulin-independent growth in the proliferating
348 domain (**Fig S6J**).
349
350 **(7) Pdk1 upregulation, protein translation and JAK/STAT signaling are linked in tumor growth**
351 We wanted to understand, if the JAK/STAT-Pdk1-S6 signaling axis observed during regenerative
352 proliferation also plays a role in tumor growth, given that tumors often coopt physiological repair
353 processes for their pathological purposes. We thus analyzed imaginal discs in which tumorigenesis
354 was induced by both reducing the function of the tumor-suppressor gene *scrib* (Bilder et al, 2000) and
355 ectopically expressing oncogenic Ras^{V12} (Dillard et al, 2021; Pagliarini & Xu, 2003). We used the *rn-*
356 *GAL4* driver to drive expression of *scrib-RNAi* and Ras^{V12} in the entire wing pouch, which causes
357 pronounced overproliferation (Cong et al, 2021; Jaiswal et al, 2023; Khezri et al, 2021). This tumor
358 model is characterized by the coordinated but spatially separated activation of JNK and JAK/STAT
359 signaling networks, whose regulatory and functional characteristics resemble those active during
360 tissue repair in *egr*-expressing discs (**Fig S7A**) (Jaiswal et al, 2023). In Ras^{V12}*,scrib-RNAi* expressing
361 discs, we found striking correlation between regions of JAK/STAT activation, elevated protein

translation and increased Pdk1 level (**Fig 7A-F**). An independent tumor model of *Psc-Su(z)2* tumors also shows correlated elevation of JAK/STAT activation and protein synthesis (**Fig S7B,C**). Importantly, these tumors, like *egr*-expressing discs, induce all hallmarks of systemic cachexia, including reduced protein translation in the non-transformed notum (**Fig 7G-I**), and must therefore overcome growth restrictions imposed on peripheral tissues (Hodgson et al, 2021; Katheder & Rusten, 2017; Khezri et al, 2021). Our observation demonstrate that tumors likely coopt JAK/STAT activation and Pdk1 elevation to support protein translation and thus tumor proliferation.

(8) Pdk1 downregulation in peripheral discs correlates with systemic growth restriction

Strikingly, Pdk1 levels appear to be a target of systemic regulation during Insulin restriction in imaginal discs. In *egr*-expressing larvae, we consistently observed that Pdk1 levels were significantly lower in peripheral imaginal disc, including the notum, leg and eye, if compared to wild type control discs (**Fig 8A-F, Fig S8**). This observation was not limited to *egr*-expressing larvae; even in the peripheral imaginal discs of Ras^{V12}*,scrib-RNAi* tumor-bearing larvae, Pdk1 levels were markedly reduced (**Fig 8G-I**). This targeted reduction of Pdk1 in peripheral imaginal discs is consistent with the overall decrease in protein synthesis and growth observed in these regions. Such downregulation suggests that systemic signals, maybe even Insulin restriction, actively suppress Pdk1 expression in non-regenerative areas. In contrast, JAK/STAT signaling in regenerative areas can counteract Pdk1 suppression and locally elevate Pdk1 levels and function. This dual regulation -upregulation in regenerative zones and downregulation in non-essential areas -highlights Pdk1's central role in mediating the balance between local regenerative demands and systemic metabolic reprogramming. Consequently, Pdk1 emerges not only as a key driver of insulin-independent regenerative proliferation but also as an integrative node that coordinates systemic growth control during tissue repair and tumorigenesis.

Discussion

Our study reveals how signaling through a JAK/STAT-Pdk1-S6K axis promotes metabolic reprogramming to drive tissue repair and regeneration in an environment of systemic growth restriction (**Fig 8J,K**). We demonstrate that in response to inflammatory damage, a senescent subpopulation of cells at the center of tissue damage induces insulin restriction via action of dILP8 on IPCs, as well as insulin resistance via action of ImpL2 on the fat body. The resulting systemic reduction of insulin signaling is evident from the decreased expression of *dILP2* and *dILP5* in IPCs, as well as the enhanced nuclear localization of dFOXO, low rates of protein synthesis and proliferation in peripheral tissues, or reduced Akt signaling and nutrient mobilization in the fat body. These findings align with previous work suggesting that systemic growth restriction, for example via repression of Ecdysone signaling, helps synchronize regeneration with developmental timing and prevents the overgrowth of undamaged tissues (Cao et al, 2022; Colombani et al, 2012; Garelli et al, 2012; Hackney & Cherbas, 2014; Halme et al, 2010).

402 However, slowing down peripheral growth poses a challenge to the regenerating cell population, which
403 must continue to support high anabolic activity despite reduced canonical Insulin/PI3K/AKT signaling.
404 The regenerating cell population circumvents this limitation by engaging a novel mechanism to sustain
405 protein synthesis. Specifically, we find that Pdk1 is robustly upregulated in the proliferative domain of
406 *egr*-expressing discs, and this upregulation is sufficient and necessary to drive ribosomal S6
407 phosphorylation and activate protein translation, even in the context of low systemic Insulin signaling.
408 The capacity of Pdk1 to function independently of insulin positions Pdk1 as a central regulator of
409 regenerative metabolism. Notably, our results mirror earlier observations of AKT-independent, yet
410 Pdk1-dependent, growth during *Drosophila* development (Radimerski et al, 2002; Rintelen et al, 2001).
411 During regeneration, we identify JAK/STAT as an upstream regulator of Pdk1, and consequently as a
412 regulator for phosphorylation of ribosomal S6 protein and activation of protein synthesis. Our work
413 thus uncovers a pathway whereby JAK/STAT signaling can mediate the known proliferation-promoting
414 function in imaginal disc development, regeneration, and tumor growth (Herrera & Bach, 2019). Of
415 note, the increase in Pdk1 protein levels likely arises from JAK/STAT regulated post-translational
416 mechanisms affecting Pdk1 stability, as we did not observe an increase in *Pdk1* transcripts in *egr*-
417 expressing discs (Floc'hlay et al, 2023). Such post-translational regulation of Pdk1 may also underlie
418 the differential regulation of Pdk1 between regenerative and peripheral tissues. While we find that the
419 proliferative domain actively upregulates Pdk1 to overcome insulin restrictions, we also find that the
420 peripheral imaginal discs downregulate Pdk1. Based on our experiments demonstrating that Pdk1
421 levels are limiting for protein translation, the peripheral reduction in Pdk1 may contribute to the
422 reduction in protein synthesis and growth of other imaginal discs. This dual regulation emphasizes the
423 surprisingly central role of Pdk1 in integrating local demands for regeneration with systemic constraints
424 on growth.
425
426 Furthermore, our work reveals that fat body catabolism, which mobilizes nutrients necessary for
427 regeneration, is activated in *egr*-expressing larvae. In addition to remodeling of the lipid stores, proteins
428 may also be catabolized, as suggested by an altered amino acid signature in the hemolymph. The
429 upregulation of amino acid and carbohydrate transporters in the proliferative domain further suggests
430 that regenerating cells actively import these mobilized nutrients, thereby fueling mTORC1 activation
431 and subsequent protein synthesis. Earlier studies find elevated levels of ornithine, glutamate, and
432 glutamine in rat wound fluids (Albina et al, 1993), similar to the ornithine, glutamate, and glutamine
433 signature in hemolymph from egr-expressing larvae. Our observations suggest that glutamate
434 metabolism may be important for regeneration, consistent with its described roles in tumor growth,
435 inflammation, and defense against oxidative stress (Altman et al, 2016; Ling et al, 2023; Zhu &
436 Thompson, 2019).
437
438 Together, our results support a model in which *egr*-induced inflammation induces systemic insulin
439 restriction and insulin resistance, thereby limiting resource availability in peripheral tissues. At the
440 same time, local activation of pathways such as JAK/STAT, Pdk1, or nutrient importers prioritizes
441 tissue repair at the damage site. A potential limitation of our study lies in the high levels of *eiger*-

expression used in this genetic model, which may not fully reflect physiological conditions. In fact, as we previously reported, *egr*-expressing discs can resemble chronic wound states, where prolonged inflammatory signaling impairs effective tissue regeneration (Jaiswal et al, 2023). However, in the widely studied *Ras^{V12},scrib-RNAi* tumor model, we observe that regions with high JAK/STAT activity also exhibit elevated Pdk1 expression and protein translation, suggesting that tumors which can induce cachexia also exploit this pathway to sustain growth despite low systemic insulin signaling. Given that Pdk1 can bypass the need for Insulin/AKT/FOXO signaling, it may not be surprising that Pdk1 upregulation is found in many cancers (Zheng et al, 2023). While oncogenic mutations may facilitate nutrient use in such a cachexic tumor environment (Lee et al, 2021; Newton et al, 2020; Santabarbara-Ruiz & Leopold, 2021; Song et al, 2019), our work specifically reveals how wild type tissues adapt within a physiological repair program to overcome systemic inhibition of growth.

In summary, our study uncovers a regulatory network wherein fat body catabolism, enhanced nutrient uptake, mTORC1 activation, and the instructive JAK/STAT-Pdk1 axis converge to support regenerative proliferation in cachexic environment. Undoubtedly, this is an ancient stress response and repair program designed to distribute nutrients from an energy store to the site of tissue damage. These findings not only advance our understanding of tissue repair mechanisms in *Drosophila* but may also offer insights into conserved pathways in mammals, as a domain characterized by ribosomal S6 protein phosphorylation was recently described in mouse and pig skin wounds, suggesting potential similarities in regenerative programs across species (Ring et al, 2023).

464 **Materials and Methods**

465

466 ***Drosophila* maintenance**

467 All experiments were performed on *Drosophila melanogaster*. Fly strains (see **Table S1**) were
468 maintained on standard fly food (10L water, 74,5g agar, 243g dry yeast, 580g corn flour, 552ml
469 molasses, 20.7g Nipagin, 35ml propionic acid) at 18°C – 22°C. Larvae from experimental crosses were
470 allowed to feed on Bloomington formulation (175.7g Nutry-Fly,1100ml water 20g dry yeast, 1.45g
471 Nipagin in 15ml Ethanol, 4.8ml Propionic acid) and raised at 18°C or 30°C to control GAL80ts-
472 dependent induction of GAL4/UAS. Our experimental design did not consider differences between
473 sexes unless for genetic crossing schemes.

474

475 ***Drosophila* genetics**

476 To induce expression of UAS-constructs, such as *UAS-egr*, under the control of rn-GAL4 in the wing
477 pouch, experiments were carried out as described in (Cosolo et al, 2019; La Fortezza et al, 2016;
478 Smith-Bolton et al, 2009) with minor modifications. Briefly, larvae of genotype *rn-GAL4, tub-GAL80^{ts}*
479 and carrying the desired *UAS*-transgenes were staged with a 6h egg collection and raised at 18°C at
480 a density of 50 larvae/vial. Overexpression of transgenes was induced by shifting the temperature to
481 30°C for 24h on the seventh day (D7) after egg deposition (AED) to relieve temperature-sensitive
482 GAL80ts repression of GAL4. Larvae were dissected after 24 h of *egr*-expression. Control genotypes
483 were generated by crossing rn-GAL4, tub-GAL80ts into a wild type background. The DUAL Control
484 genetic ablation system (DCS) was employed, wherein a single heat shock simultaneously activates
485 genetic cell ablation by egr-expression within the *salm* domain and GAL4 expression in the *dve-GAL4*
486 domain (*hsFLP; hs-p65::zip, lexAOp-egrNI/CyO; salm-zip::LexA-DBD, DVE>>GAL4)* (Harris et al,
487 2020). Specifically, larvae were raised at 25°C and subjected to a 1-hour heat shock at 37°C on Day
488 4.5, followed by dissection 24 hours post-heat shock. The Pdk1-GFP line (BDSC: 59836) was
489 characterized using the following approaches: a complex expression pattern can be observed in wild
490 type tissues in immunofluorescence, where GFP is detected in the cytoplasm but also at membranes
491 (see for example, Fig 6C). Tissues form larvae produce a band of the expected size on Western blot.
492 Three independent RNAi lines (BDSC: 27725, BDSC: 34936, BDSC: 36071) targeting the 3' region of
493 the Pdk1 transcript downstream of the GFP-cassette insertion site can robustly knock-down GFP
494 expression (see for example Fig 5E). We conclude that a full-length, membrane-recruitable and
495 genetically tractable protein is produced from the endogenous locus. Thus. the annotation of the
496 insertion site in FlyBase is incorrectly oriented.

497

498 **Immunohistochemistry of wing imaginal discs**

499 Wing discs from third instar larvae were dissected and fixed for 15 minutes at room temperature in 4%
500 paraformaldehyde in PBS. Washes were performed in PBS containing 0.1% TritonX-100 (PBT). The
501 discs were then incubated with primary antibodies (listed in **Table S2**) in 0.1% PBT, gently mixed
502 overnight at 4°C. During incubation with cross-absorbed secondary antibodies coupled to Alexa
503 Fluorophores at room temperature for 2 hours, tissues were counterstained with DAPI (0.25 ng/µL,

504 Sigma, D9542). Tissues were mounted using SlowFade Gold Antifade (Invitrogen, S36936). To ensure
505 comparability in staining between different genotypes, experimental and control discs were processed
506 in the same vial and mounted on the same slides whenever possible. Images were acquired using the
507 Leica TCS SP8 Microscope, using the same confocal settings for linked samples and processed using
508 tools in Fiji.
509
510 **Protein synthesis assays using OPP- Click-iT staining**
511 OPP Assays were performed using Click-iT® Plus OPP Protein Synthesis Assay Kits (Invitrogen
512 Molecular Probe) according to manufacturer's instructions. Briefly, larvae were dissected and inverted
513 cuticles were incubated with a 1:1000 dilution of Component A in Schneider's medium for 15 minutes
514 on a nutator. Larval cuticles were fixed with 4% paraformaldehyde for 15 minutes, rinsed twice in 0.1%
515 PBT, and permeabilized with 0.5% PBT for 15 minutes. The cuticles were then stained with the Click-
516 iT® cocktail for 30 minutes at room temperature, protected from light. Further immunohistochemistry
517 analysis and sample mounting was performed as described above.
518
519 **EdU labelling**
520 EdU incorporation was performed using the Click-iT Plus EdU Alexa Fluor 647 Imaging Kit. Briefly,
521 larval cuticles were inverted in Schneider's medium and incubated with EdU (10μM final concentration)
522 at RT for 15 minutes. Cuticles were then fixed in 4% PFA/PBS for 15 minutes, washed for 30 minutes
523 in PBT 0.5%. EdU-Click-iT labeling was performed according to manufacturer's guidelines. Further
524 immunohistochemistry analysis and sample mounting was performed as described above.
525
526 **SA-β-Gal staining**
527 Cell senescence detection kit from Invitrogen (C10850) was used to analyze senescence-associated
528 β-galactosidase activity. Briefly, larval cuticles were inverted in PBS, fixed with 4% PFA, washed with
529 1% BSA (in PBS) and then incubated in working solution for 2h at 37°C, according to manufacturer's
530 instructions. Washing steps were performed in PBS and PBS containing 0.1% TritonX-100 (PBT).
531 Further immunohistochemistry analysis and sample mounting was performed as described above.
532
533 **Fat body Nile Red staining**
534 Early third instar larvae were collected in PBS and dissected, leaving the gut intact to prevent fat body
535 loss. Inverted cuticles were transferred to an Eppendorf tube and fixed with 4% paraformaldehyde/PBS
536 for 15 minutes. Samples were washed in 0.1% PBT. Cuticles were incubated with Nile Red (2 μg/mL
537 in PBS) for 1 hour, protected from light. Following incubation, samples were washed in PBS, the fat
538 body was dissected and mounted as described above.
539
540 **Hemolymph sample preparation**
541 Fifteen larvae were collected and thoroughly washed with Milli-Q water to remove any fly food particles.
542 Care was taken to ensure no food particles remained on the larvae surfaces, and they were dried
543 using Kim Tech paper wipes. Each larva was punctured in the center using forceps and transferred to

544 a 0.5 mL microcentrifuge tube with three 1 mm holes at the bottom. The 0.5 mL microcentrifuge tube
545 was then placed into a pre-cooled 1.5 mL microcentrifuge tube. One larva at a time was processed in
546 this assembly and centrifuged in a microfuge for 10 seconds. After each centrifugation, the larval
547 carcass was removed from the 0.5 mL microcentrifuge tube to prevent blockage of the holes.
548 Hemolymph isolated from the 15 larvae was collected in the bottom 1.5 mL tube. From the total
549 collected hemolymph, 8 µL was transferred to a fresh 1.5 mL tube, and 10 µL of ultrapure Milli-Q water,
550 30 µL of methanol, an internal standard, and 50 µL of MTBE were added. The solution was mixed
551 thoroughly and centrifuged at 1000g for 10 minutes at 4°C. After centrifugation, the organic and polar
552 phases were collected separately in different tubes for metabolite measurement.
553
554 **Hemolymph metabolomic analyses**
555 Non-targeted analysis of polar metabolites by LC-MS was carried out as described previously
556 (Edwards-Hicks et al, 2020) using an Agilent 1290 Infinity II UHPLC in line with a Bruker Impact II
557 QTOF-MS operating in negative and positive ion mode. Scan range was from 20 to 1050 Da and mass
558 calibration was performed at the beginning of each run. LC separation was on a Waters Atlantis
559 Premier BEH ZHILIC column (100 x 2.1 mm, 1.7 µm particles), buffer A was 20 mM ammonium
560 carbonate and 5 µM medronic acid in milliQ H2O and buffer B was 90:10 acetonitrile:buffer A and the
561 solvent gradient was from 95% to 55% buffer B over 14 minutes. Flow rate was 180 µL/min, column
562 temperature was 35 °C, autosampler temperature was 5 °C and injection volume was 3 µL. Data
563 processing including feature detection, feature deconvolution, and annotation of features was
564 performed using MetaboScape (version 2023b). Quantile normalization was performed to minimize
565 sample size effects and further statistical processing were performed with R. Metabolites with missing
566 values were eliminated from the dataset. Both, the Shapiro-Wilk test and the Q-Q plot, showed that
567 the data was not normally distributed. Therefore, a two-sided, unpaired Wilcoxon rank-sum test was
568 performed on the quantile normalized data. Only metabolites with at least <0.75 and >1.5-fold change
569 and a p-value < 0.19 and were selected for further analysis and were displayed in a heatmap with row-
570 wise normalization (Fig 3L).
571
572 **Thin Layer Chromatography (TLC)**
573 Fat bodies were dissected in cold PBS from third instar (L3) control (rn-GAL4, tubGAL80ts) and egr-
574 expressing (rn-GAL4, UAS-egr, tubGAL80ts)larvae, and from wild type larvae starved for 24 h. Three
575 fat bodies were pooled per sample and immediately transferred into 100µL chloroform: methanol (3:1)
576 solution, followed by storage on ice. Samples were mechanically homogenized and centrifuged at
577 15,000 × g for 5 minutes at 4°C. For semi-quantitative analysis of triglycerides, a standard curve was
578 prepared using lard as a reference material, dissolved in chloroform : methanol (3:1) at the following
579 concentrations: STD1 (75 µg/µL); STD2 (60 µg/µL); STD3 (50 µg/µL); STD4 (37.5 µg/µL); STD5 (25
580 µg/µL); STD6 (15 µg/µL); STD7 (10 µg/µL). A blank control containing only the solvent mixture
581 (chloroform:methanol (3:1)) was included. Samples and standards were loaded onto a glass silica gel
582 TLC plate (Millipore). The mobile phase consisted of a hexane:diethyl ether (4:1) solvent system.
583 Chromatography was performed and after air-drying, the TLC plate was treated with ceric ammonium

584 heptamolybdate (CAM) staining solution and developed at 80°C, with band development monitored at
585 5-minute intervals. Images were captured using a gel documentation system (gelONE); image analysis
586 and quantification were performed using ImageJ. Automatic image thresholding was applied using the
587 Otsu method, and regions of interest (ROIs) were defined for each band. Integrated intensity analysis
588 was performed, and triglyceride density was quantified based on the standard curve.
589
590 **Real-Time PCR**
591 Third instar (L3) control (rn-GAL4, tubGAL80ts), egr expressing (rn-GAL4, UAS-egr, tubGAL80ts), and
592 wild type larvae starved for 24 h larvae were carefully collected from the food and pooled in groups of
593 three male larvae per sample. Samples were homogenized in 100 µL of TRIzol, and RNA was
594 extracted using chloroform (20 µL), followed by precipitation with 50 µL of isopropanol. The purified
595 RNA was suspended in nuclease-free water, subjected to DNase treatment and reverse transcription
596 was performed using RevertAid Reverse Transcriptase (Thermo Fisher Scientific) according to
597 manufacturer's guidelines. qPCR was performed using the Blue S'Green qPCR Kit Separate ROX
598 (Biozym) on a LightCycler 480 (Roche). Standard dilution series (1:5) were generated for each primer
599 pair to determine primer efficiency based on the regression curve. The following primers were used
600 (for, rev 5'-3'): Rpl1 (TCCACCTTGAAGAAGGGCTA, TTGCGGATCTCCTCAGACTT), Ilp2
601 (ATCCCGTGATTCCACCACAAG, GCGGTTCCGATATCGAGTTA), Ilp5
602 (GCCTTGATGGACATGCTGA, AGCTATCCAAATCCGCCA). Gene expression levels were
603 normalized to the reference gene Rpl1, and relative expression was calculated using the Pfaffl method.
604 Statistical outliers were identified using the ROUT test (Q = 1%) and were removed to maintain data
605 consistency. Statistical analysis was performed using the Kruskal-Wallis test.
606
607 **Western Blot Analysis**
608 Fat bodies were dissected in cold PBS from third-instar (L3) control (rn-GAL4, tubGAL80ts) and egr-
609 expressing (rn-GAL4, UAS-egr, tubGAL80ts) larvae, and from wild type larvae starved for 24 h. Five
610 fat bodies were lysed on ice (300mM NaCl, 50mM Tris-HCl ph 7,5, 1% Triton X-100, 0.1mM EDTA,
611 0.1% SDS,
612 5% Glycerol, Roche Complete protease inhibitor cocktail and Complete phosphate inhibitor cocktail).
613 Tissues were further homogenized and centrifuged at 6000g for 3 minutes at 4°C. Supernatants were
614 incubated in Laemmli buffer at 85°C for 5 minutes. Samples were loaded onto Mini-PROTEAN TGX
615 gels (4–15%) corresponding to one fat body per lane. After electrophoresis, proteins were transferred
616 onto a nitrocellulose membrane, blocked in 1× Tris-buffered saline containing bovine serum albumin,
617 incubated overnight with primary antibodies at 4°C and secondary antibody for 1 h at RT. Proteins
618 were visualized using SuperSignal West Femto Maximum Sensitivity Substrate and a Bio-Rad
619 ChemiDoc-MP imaging system.
620 **Image quantification and statistical analysis - General comments**
621 For all quantifications, control and experimental samples were processed together and imaged in
622 parallel, using the same confocal settings. Images were processed, analyzed and quantified using
623 tools in Fiji (ImageJ 2.14) (Schindelin et al, 2012). Extreme care was taken to apply consistent methods

624 to control and experimental samples (i.e., number of projected sections, thresholding methods,
625 processing) for image analysis and quantifications. See **File S1** for macros used in FIJI during image
626 segmentation and quantifications. Further details on segmentation and quantifications are provided
627 below. Figure panels were assembled using Affinity Designer 2.4.0. Statistical analyses were
628 performed in Graphpad Prism. Illustrations were done in Biorender.
629 To quantify fluorescence intensities inside the proliferative domain (PD^{egr}), a mask of the high JNK-
630 signaling domain region was generated, followed by creating a 20µm band on the outside to mark the
631 proliferative domain. Fluorescence intensities in proliferative domains was always compared to
632 fluorescence intensities within the pouch domain of control discs, unless otherwise noted.
633
634 **Quantification of cycling cells using EdU incorporation**
635
636 **(a) EdU quantification in notum:** An xy-section with the maximum number of notum epithelial cells
637 was selected, excluding any myoblast cells. A mask was created from the DAPI staining to represent
638 nuclei and saved as ROI. A binary operation (AND) was used to compute a notum DAPI mask with
639 the aid of a manually selected notum region (FileS1, Macro-1L(a)). This mask was then used to
640 measure EdU intensity.
641 **(b) EdU quantification within 10µm bands:** In *egr*-expressing discs, TRE-RFP expression was used
642 to generate a mask of the high JNK-signaling domain (FileS1, Macro-1D(a)). The boundary of this
643 mask defined the regions inside and outside the high JNK region. Five 10µm bands were created
644 outside the high JNK-signaling domain, and three 10µm bands inside of the JNK-signaling domain.
645 Also applying a DAPI mask to each band (FileS1, Macro-1D(b)), the mean EdU intensity in each of
646 the 10µm bands was measured. Consistent with previous studies (Cosolo et al, 2019; Jaiswal et al,
647 2023), the highest EdU intensities were observed in 3 bands outside the JNK-signaling domain, which
648 was denoted as proliferative domain.
649 **(c) EdU quantification in eye disc:** For the eye disc, an EdU mask (FileS1, Macro-2T(a)) was
650 generated using the EdU staining, which was then applied to measure EdU intensity in the entire visible
651 eye disc.
652
653 **Quantification of Upd3-LacZ levels**
654 A maximum projection of TRE-RFP expression was used to generate a mask of the high JNK-signaling
655 domain in *egr*-expressing disc (FileS1, Macro-S3H(a)). Upd3-LacZ intensity was measured within the
656 TRE-RFP mask of the high JNK-signaling domain in *egr*-expressing disc, while for the control disc,
657 Upd3-LacZ intensity was measured in the pouch.
658
659 **Quantification of ImpL2-GFP levels**
660 A pouch mask was generated using the maximum projection of an anti-Nubbin staining (FileS1, Macro-
661 3H(a)) for both control and *egr*-expressing discs. ImpL2-GFP intensities were measured within the
662 Nubbin mask on the sum projection of the ImpL2-GFP signals within the stack (seven slices in each
663 disc).

664

665 **Quantification of OPP levels**

666 **(a) in different regions of wing imaginal disc:** In the control disc, mean OPP intensity was measured
667 separately in the pouch, hinge, and notum regions. In *egr*-expressing discs, mean OPP intensity was
668 measured in the high JNK signaling region (TRE-RFP mask), the proliferative region (20μm band
669 around the TRE-RFP mask), and the notum region. In control discs, the pouch, hinge, and notum
670 regions were selected using wing fold landmarks. In *egr*-expressing discs, a max projection of TRE-
671 RFP intensities was used to create a mask of the high JNK signaling domain (FileS1, Macro-1G(a)),
672 which was applied to measure OPP intensity in the high JNK region. A 20μm band outside the high
673 JNK region was generated to mark the proliferative region, and OPP intensity in this domain was
674 measured. For the notum, a manual selection along the first notum fold and outlining the edges of the
675 notum was carried out.

676 **(b) in the eye disc**: For the eye-antennal disc, the DAPI staining was used to generate a mask of the
677 tissue outline (FileS1, Macro-2Q(a)) and combined with a manual selection of the eye disc to generate
678 a region of interest (ROI) within which we measured OPP intensity.

679

680 **Quantification of nuclear dFOXO levels**

681 In control discs, a slice with the maximum number of pouch cells was selected and a DAPI mask
682 (FileS1, Macro-4G(a)) was generated and combined with manual pouch selection to create a pouch
683 nuclear mask. This mask was used to measure mean dFOXO intensity in the pouch nucleus. In *egr*-
684 expressing discs, a single slice from the Z-stack with the maximum number of cells in the proliferative
685 domain was selected. A max projection of TRE-RFP intensities was used to create a mask of the high
686 JNK signaling domain, and a 20μm band was created to locate the proliferative region. A DAPI mask
687 (FileS1, Macro-4G(b)) was generated from the selected slice and combined with the 20μm band to
688 create a new mask for the proliferative cell nuclei, which was used to measure dFOXO intensity in the
689 nucleus. For the analysis of nuclear dFOXO in the notum, a Z-slice containing the maximum number
690 of notum cells was selected. A DAPI mask (File S1, Macro-2F(a)) was generated and combined with
691 manual selection of notum, guided by wing fold, to create a notum nuclear mask. Please note that
692 discs and fat body were treated with Leptomycin B (413nM) for 30 min before dissection to block
693 nuclear export.

694

695 **Quantification of Pdk1 GFP, p-S6 and OPP levels in the en-GAL4 domain**

696 The slice with the maximum number of pouch cells was selected, and masks of the anterior and
697 posterior pouch compartments were generated by segmenting the enGAL4, UAS-RFP expression
698 domain. Levels of p-S6(File S1, Macro 6F(a)) and Pdk1-GFP intensities were measured within these
699 masks and the P/A ratio (en-GAL4 region/non-en-GAL4 region) was calculated. Mean OPP intensity
700 in the control and experimental pouch en-GAL4 domain was measured and reported.

701

702 **Quantification of 10xStat92E-GFP levels in the fat body**

703 A single slice from the Z-stack with the maximum number of nuclei was selected. A 200x200 pixel
704 square region was defined and used as a standard area for measurement of GFP intensities.
705
706 **Quantification of lipid droplet size and shape**
707 A single slice from the Z-stack through the most anterior fat body containing the maximum number of
708 nuclei was selected. A published STAR protocol was applied to measure lipid droplet area and the
709 'roundness' of lipid droplets (defined as the relationship between area and length of major droplet axis)
710 in both control and experimental samples (Dark et al, 2022).
711

Data availability

All data, workflows and FIJI based algorhithms necessary to interpret the data are included within the manuscript. Original microscopy image files and intermediate segmentation results will be made available upon request. Requests should be addressed to and will be fulfilled by AKC.

Inclusion & ethics statement

All authors fulfill the criteria to be included as co-authors. All authors agreed to their roles and responsibilities in the study design.

Author Contributions

Conceptualization AVM, AKC; Data curation AVM, LNe, LNo, LH, AKC; Formal analysis AVM, LNe, LH, JB, AKC; Funding acquisition KK, AKC; Investigation AVM, LNe, LNo, AS, AKC; Methodology AVM, LNe, LNo, AS, IG, JB, AKC; Project administration IG, AKC; Supervision KK, AKC; Validation AVM, LNe, LNo, AS, KK, AKC; Visualization AVM, LNe, LH; Writing – original draft AVM, AKC; Writing – review & editing AVM, KK, AKC

Acknowledgements

We thank the staff of the Life Imaging Center (LIC) in the Hilde Mangold House (HMH) of the Albert-Ludwigs-University of Freiburg for help with their confocal microscopy resources, and the excellent support in image recording. We specifically thank the DFG for supporting our imaging work through project number 414136422. We thank the Lighthouse Core Facility and its staff, as well as Elisabeth Savkova, Janhvi Jaiswal and Carlo Crucianelli for help with our experimental work. We thank Robin Harris, Susumi Hirobayashi, Hugo Stocker, Aurelio Teleman and Hong Xu, Iswar Hariharan, Dirk Bohmann for sharing reagents and the Bloomington *Drosophila* Stock Center (BDSC), the Vienna *Drosophila* Stock Collection (VDRC), the University of Zurich ORFeome Project (FlyORF), the Developmental Studies Hybridoma Bank (DSHB) and the Monoclonal Antibody Core Facility at the Helmholtz Zentrum Munich for providing fly stocks and antibodies. We thank the IMPRS-EBM and SGBM graduate schools for supporting our doctoral researchers.

Funding

Funding for this work was provided by the Deutsche Forschungsgemeinschaft (DFG, German Research Foundation) under Germany´s Excellence Strategy (CIBSS – EXC-2189) to KK and AKC, and by the DFG Heisenberg Program to AKC (668189) and to KK (544402801), as well as DFG grants to AKC (667603) and to KK (529943809). Funding was furthermore provided by the Boehringer

Ingelheim Foundation (BIF Plus3 & Rise Up) to AKC. The funders had no role in study design, data collection and analysis, decision to publish, or preparation of the manuscript.

Declaration of Interest

The authors declare no competing interests.

758 **References**

759

760 Agrawal, N., Delanoue, R., Mauri, A., Basco, D., Pasco, M., Thorens, B. & Leopold, P. (2016) The Drosophila TNF
761 Eiger Is an Adipokine that Acts on Insulin-Producing Cells to Mediate Nutrient Response. *Cell Metab*, 23(4), 675-
762 84.

763 Albina, J. E., Abate, J. A. & Mastrofrancesco, B. (1993) Role of ornithine as a proline precursor in healing wounds.
764 *J Surg Res*, 55(1), 97-102.

765 Altman, B. J., Stine, Z. E. & Dang, C. V. (2016) From Krebs to clinic: glutamine metabolism to cancer therapy.
766 *Nat Rev Cancer*, 16(10), 619-34.

767 Argiles, J. M., Busquets, S., Stemmler, B. & Lopez-Soriano, F. J. (2014) Cancer cachexia: understanding the
768 molecular basis. *Nat Rev Cancer*, 14(11), 754-62.

769 Aviner, R. (2020) The science of puromycin: From studies of ribosome function to applications in biotechnology.
770 *Comput Struct Biotechnol J*, 18, 1074-1083.

771 Beller, M., Bulankina, A. V., Hsiao, H. H., Urlaub, H., Jackle, H. & Kuhnlein, R. P. (2010) PERILIPIN-dependent
772 control of lipid droplet structure and fat storage in Drosophila. *Cell Metab*, 12(5), 521-32.

773 Bilder, D., Li, M. & Perrimon, N. (2000) Cooperative regulation of cell polarity and growth by Drosophila tumor
774 suppressors. *Science*, 289(5476), 113-6.

775 Bilder, D., Ong, K., Hsi, T. C., Adiga, K. & Kim, J. (2021) Tumour-host interactions through the lens of Drosophila.
776 *Nat Rev Cancer*, 21(11), 687-700.

777 Boulan, L., Andersen, D., Colombani, J., Boone, E. & Leopold, P. (2019) Inter-Organ Growth Coordination Is
778 Mediated by the Xrp1-Dilp8 Axis in Drosophila. *Dev Cell*, 49(5), 811-818 e4.

779 Cao, X., Rojas, M. & Pastor-Pareja, J. C. (2022) Intrinsic and damage-induced JAK/STAT signaling regulate
780 developmental timing by the Drosophila prothoracic gland. *Dis Model Mech*, 15(1).

781 Chatterjee, N. & Bohmann, D. (2012) A versatile PhiC31 based reporter system for measuring AP-1 and Nrf2
782 signaling in Drosophila and in tissue culture. *PLoS One*, 7(4), e34063.

783 Colombani, J., Andersen, D. S. & Leopold, P. (2012) Secreted peptide Dilp8 coordinates Drosophila tissue growth
784 with developmental timing. *Science*, 336(6081), 582-5.

785 Cong, B., Nakamura, M., Sando, Y., Kondo, T., Ohsawa, S. & Igaki, T. (2021) JNK and Yorkie drive tumor
786 malignancy by inducing L-amino acid transporter 1 in Drosophila. *PLoS Genet*, 17(11), e1009893.

787 Cosolo, A., Jaiswal, J., Csordas, G., Grass, I., Uhlirova, M. & Classen, A. K. (2019) JNK-dependent cell cycle stalling
788 in G2 promotes survival and senescence-like phenotypes in tissue stress. *Elife*, 8.

789 Crucianelli, C., Jaiswal, J., Vijayakumar Maya, A., Nogay, L., Cosolo, A., Grass, I. & Classen, A. K. (2022) Distinct
790 signaling signatures drive compensatory proliferation via S-phase acceleration. *PLoS Genet*, 18(12), e1010516.

791 Dark, C., Cheung, S. & Cheng, L. Y. (2022) Analyzing cachectic phenotypes in the muscle and fat body of
792 Drosophila larvae. *STAR Protoc*, 3(1), 101230.

793 Dillard, C., Reis, J. G. T. & Rusten, T. E. (2021) Ras(V12); scrib(-/-) Tumors: A Cooperative Oncogenesis Model
794 Fueled by Tumor/Host Interactions. *Int J Mol Sci*, 22(16).

795 Ding, G., Xiang, X., Hu, Y., Xiao, G., Chen, Y., Binari, R., Comjean, A., Li, J., Rushworth, E., Fu, Z., Mohr, S. E.,
796 Perrimon, N. & Song, W. (2021) Coordination of tumor growth and host wasting by tumor-derived Upd3. *Cell*
797 *Rep*, 36(7), 109553.

798 Dvorak, H. F. (1986) Tumors: wounds that do not heal. Similarities between tumor stroma generation and
799 wound healing. *N Engl J Med*, 315(26), 1650-9.

800 Edwards-Hicks, J., Mitterer, M., Pearce, E. L. & Buescher, J. M. (2020) Metabolic Dynamics of In Vitro CD8+ T
801 Cell Activation. *Metabolites*, 11(1).

802 Eming, S. A., Murray, P. J. & Pearce, E. J. (2021) Metabolic orchestration of the wound healing response. *Cell*
803 *Metab*, 33(9), 1726-1743.

804 Eming, S. A., Wynn, T. A. & Martin, P. (2017) Inflammation and metabolism in tissue repair and regeneration.
805 *Science*, 356(6342), 1026-1030.

806 Enomoto, M. & Igaki, T. (2022) Cell-cell interactions that drive tumorigenesis in Drosophila. *Fly (Austin)*, 16(1),
807 367-381.

808 Figueroa-Clarevega, A. & Bilder, D. (2015) Malignant Drosophila tumors interrupt insulin signaling to induce
809 cachexia-like wasting. *Dev Cell*, 33(1), 47-55.

810 Floc'hlay, S., Balaji, R., Stankovic, D., Christiaens, V. M., Bravo Gonzalez-Blas, C., De Winter, S., Hulselmans, G.
811 J., De Waegeneer, M., Quan, X., Koldere, D., Atkins, M., Halder, G., Uhlirova, M., Classen, A. K. & Aerts, S. (2023)
812 Shared enhancer gene regulatory networks between wound and oncogenic programs. *Elife*, 12.

813 Fox, D. T., Cohen, E. & Smith-Bolton, R. (2020) Model systems for regeneration: Drosophila. *Development*,
814 147(7).

815 Garelli, A., Gontijo, A. M., Miguela, V., Caparros, E. & Dominguez, M. (2012) Imaginal discs secrete insulin-like
816 peptide 8 to mediate plasticity of growth and maturation. *Science*, 336(6081), 579-82.

817 Gontijo, A. M. & Garelli, A. (2018) The biology and evolution of the Dilp8-Lgr3 pathway: A relaxin-like pathway
818 coupling tissue growth and developmental timing control. *Mechanisms of Development.* Elsevier Ireland Ltd.

819 Gutierrez, E., Wiggins, D., Fielding, B. & Gould, A. P. (2007) Specialized hepatocyte-like cells regulate Drosophila
820 lipid metabolism. *Nature*, 445(7125), 275-80.

821 Hackney, J. F. & Cherbas, P. (2014) Injury response checkpoint and developmental timing in insects. *Fly (Austin)*,
822 8(4), 226-31.

823 Halme, A., Cheng, M. & Hariharan, I. K. (2010) Retinoids regulate a developmental checkpoint for tissue
824 regeneration in Drosophila. *Curr Biol*, 20(5), 458-63.

825 Harris, R. E., Stinchfield, M. J., Nystrom, S. L., McKay, D. J. & Hariharan, I. K. (2020) Damage-responsive,
826 maturity-silenced enhancers regulate multiple genes that direct regeneration in Drosophila. *Elife*, 9.

827 Herrera, S. C. & Bach, E. A. (2019) JAK/STAT signaling in stem cells and regeneration: from Drosophila to
828 vertebrates. *Development*, 146(2).

829 Herrera, S. C., Martin, R. & Morata, G. (2013) Tissue homeostasis in the wing disc of Drosophila melanogaster:
830 immediate response to massive damage during development. *PLoS Genet*, 9(4), e1003446.

831 Hersperger, F., Meyring, T., Weber, P., Chhatbar, C., Monaco, G., Dionne, M. S., Paeschke, K., Prinz, M., Gross,
832 O., Classen, A. K. & Kierdorf, K. (2024) DNA damage signaling in Drosophila macrophages modulates systemic
833 cytokine levels in response to oxidative stress. *Elife*, 12.

834 Hodgson, J. A., Parvy, J. P., Yu, Y., Vidal, M. & Cordero, J. B. (2021) Drosophila Larval Models of Invasive
835 Tumorigenesis for In Vivo Studies on Tumour/Peripheral Host Tissue Interactions during Cancer Cachexia. *Int J*
836 *Mol Sci*, 22(15).

837 Holz, M. K., Ballif, B. A., Gygi, S. P. & Blenis, J. (2005) mTOR and S6K1 mediate assembly of the translation
838 preinitiation complex through dynamic protein interchange and ordered phosphorylation events. *Cell*, 123(4),
839 569-80.

840 Hopkins, B. D., Goncalves, M. D. & Cantley, L. C. (2020) Insulin-PI3K signalling: an evolutionarily insulated
841 metabolic driver of cancer. *Nat Rev Endocrinol*, 16(5), 276-283.

842 Hoxhaj, G. & Manning, B. D. (2020) The PI3K-AKT network at the interface of oncogenic signalling and cancer
843 metabolism. *Nat Rev Cancer*, 20(2), 74-88.

844 Huang, W., Hickson, L. J., Eirin, A., Kirkland, J. L. & Lerman, L. O. (2022) Cellular senescence: the good, the bad
845 and the unknown. *Nat Rev Nephrol*, 18(10), 611-627.

846 Ingaramo, M. C., Sanchez, J. A., Perrimon, N. & Dekanty, A. (2020) Fat Body p53 Regulates Systemic Insulin
847 Signaling and Autophagy under Nutrient Stress via Drosophila Upd2 Repression. *Cell Rep*, 33(4), 108321.

848 Jaiswal, J., Egert, J., Engesser, R., Peyroton, A. A., Nogay, L., Weichselberger, V., Crucianelli, C., Grass, I., Kreutz,
849 C., Timmer, J. & Classen, A. K. (2023) Mutual repression between JNK/AP-1 and JAK/STAT stratifies senescent
850 and proliferative cell behaviors during tissue regeneration. *PLoS Biol*, 21(5), e3001665.

851 Jewell, J. L., Russell, R. C. & Guan, K. L. (2013) Amino acid signalling upstream of mTOR. *Nat Rev Mol Cell Biol*,
852 14(3), 133-9.

853 Jiang, H., Kimura, T., Hai, H., Yamamura, R. & Sonoshita, M. (2022) Drosophila as a toolkit to tackle cancer and
854 its metabolism. *Front Oncol*, 12, 982751.

855 Kakanj, P., Moussian, B., Gronke, S., Bustos, V., Eming, S. A., Partridge, L. & Leptin, M. (2016) Insulin and TOR
856 signal in parallel through FOXO and S6K to promote epithelial wound healing. *Nat Commun*, 7, 12972.

857 Kashio, S. & Miura, M. (2020) Kynurenine Metabolism in the Fat Body Non-autonomously Regulates Imaginal
858 Disc Repair in Drosophila. *iScience*, 23(12), 101738.

859 Kashio, S., Obata, F., Zhang, L., Katsuyama, T., Chihara, T. & Miura, M. (2016) Tissue nonautonomous effects of
860 fat body methionine metabolism on imaginal disc repair in Drosophila. *Proc Natl Acad Sci U S A*, 113(7), 1835-
861 40.

862 Katheder, N. S. & Rusten, T. E. (2017) Microenvironment and tumors-a nurturing relationship. *Autophagy*,
863 13(7), 1241-1243.

864 Keshet, R., Szlosarek, P., Carracedo, A. & Erez, A. (2018) Rewiring urea cycle metabolism in cancer to support
865 anabolism. *Nat Rev Cancer*, 18(10), 634-645.

866 Khezri, R., Holland, P., Schoborg, T. A., Abramovich, I., Takats, S., Dillard, C., Jain, A., O'Farrell, F., Schultz, S. W.,
867 Hagopian, W. M., Quintana, E. M., Ng, R., Katheder, N. S., Rahman, M. M., Teles Reis, J. G., Brech, A., Jasper, H.,
868 Rusan, N. M., Jahren, A. H., Gottlieb, E. & Rusten, T. E. (2021) Host autophagy mediates organ wasting and
869 nutrient mobilization for tumor growth. *EMBO J*, 40(18), e107336.

870 Komander, D., Fairservice, A., Deak, M., Kular, G. S., Prescott, A. R., Peter Downes, C., Safrany, S. T., Alessi, D.
871 R. & van Aalten, D. M. (2004) Structural insights into the regulation of PDK1 by phosphoinositides and inositol
872 phosphates. *EMBO J*, 23(20), 3918-28.

873 Kwon, Y., Song, W., Droujinine, I. A., Hu, Y., Asara, J. M. & Perrimon, N. (2015) Systemic organ wasting induced
874 by localized expression of the secreted insulin/IGF antagonist ImpL2. *Dev Cell*, 33(1), 36-46.

875 La Fortezza, M., Schenk, M., Cosolo, A., Kolybaba, A., Grass, I. & Classen, A. K. (2016) JAK/STAT signalling
876 mediates cell survival in response to tissue stress. *Development*, 143(16), 2907-19.

877 La Marca, J. E. & Richardson, H. E. (2020) Two-Faced: Roles of JNK Signalling During Tumourigenesis in the
878 Drosophila Model. *Front Cell Dev Biol*, 8, 42.

879 Lama-Sherpa, T. D., Jeong, M. H. & Jewell, J. L. (2023) Regulation of mTORC1 by the Rag GTPases. *Biochem Soc*
880 *Trans*, 51(2), 655-664.

881 Lee, J., Ng, K. G., Dombek, K. M., Eom, D. S. & Kwon, Y. V. (2021) Tumors overcome the action of the wasting
882 factor ImpL2 by locally elevating Wnt/Wingless. *Proc Natl Acad Sci U S A*, 118(23).

883 Levina, A., Fleming, K. D., Burke, J. E. & Leonard, T. A. (2022) Activation of the essential kinase PDK1 by
884 phosphoinositide-driven trans-autophosphorylation. *Nat Commun*, 13(1), 1874.

885 Li, J., Kim, S. G. & Blenis, J. (2014) Rapamycin: One drug, many effects. *Cell Metabolism.*

886 Lieu, E. L., Nguyen, T., Rhyne, S. & Kim, J. (2020) Amino acids in cancer. *Exp Mol Med*, 52(1), 15-30.

887 Ling, Z. N., Jiang, Y. F., Ru, J. N., Lu, J. H., Ding, B. & Wu, J. (2023) Amino acid metabolism in health and disease.
888 *Signal Transduct Target Ther*, 8(1), 345.

889 Liu, G. Y. & Sabatini, D. M. (2020) mTOR at the nexus of nutrition, growth, ageing and disease. *Nat Rev Mol Cell*
890 *Biol*, 21(4), 183-203.

891 Liu, Y., Saavedra, P. & Perrimon, N. (2022) Cancer cachexia: lessons from Drosophila. *Dis Model Mech*, 15(3).

892 Lodge, W., Zavortink, M., Golenkina, S., Froldi, F., Dark, C., Cheung, S., Parker, B. L., Blazev, R., Bakopoulos, D.,
893 Christie, E. L., Wimmer, V. C., Duckworth, B. C., Richardson, H. E. & Cheng, L. Y. (2021) Tumor-derived MMPs
894 regulate cachexia in a Drosophila cancer model. *Dev Cell*, 56(18), 2664-2680 e6.

895 MacCarthy-Morrogh, L. & Martin, P. (2020) *W O U N D H E A L I N G The hallmarks of cancer are also the*
896 *hallmarks of wound healing*.

897 Manning, B. D. & Cantley, L. C. (2007) AKT/PKB signaling: navigating downstream. *Cell*, 129(7), 1261-74.

898 Manning, B. D. & Toker, A. (2017) AKT/PKB Signaling: Navigating the Network. *Cell.* Cell Press.

899 Marti, I. L. A. A. & Reith, W. (2021) Arginine-dependent immune responses. *Cell Mol Life Sci*, 78(13), 5303-5324.

900 Martinez-Reyes, I. & Chandel, N. S. (2021) Cancer metabolism: looking forward. *Nat Rev Cancer*, 21(10), 669-
901 680.

902 Meacham, C. E., DeVilbiss, A. W. & Morrison, S. J. (2022) Metabolic regulation of somatic stem cells in vivo. *Nat*
903 *Rev Mol Cell Biol*, 23(6), 428-443.

904 Nakamura, M., Verboon, J. M., Allen, T. E., Abreu-Blanco, M. T., Liu, R., Dominguez, A. N. M., Delrow, J. J. &
905 Parkhurst, S. M. (2020) Autocrine insulin pathway signaling regulates actin dynamics in cell wound repair. *PLoS*
906 *Genet*, 16(12), e1009186.

907 Newton, H., Wang, Y. F., Camplese, L., Mokochinski, J. B., Kramer, H. B., Brown, A. E. X., Fets, L. & Hirabayashi,
908 S. (2020) Systemic muscle wasting and coordinated tumour response drive tumourigenesis. *Nat Commun*,
909 11(1), 4653.

910 Pagliarini, R. A. & Xu, T. (2003) A genetic screen in Drosophila for metastatic behavior. *Science*, 302(5648), 1227-
911 31.

912 Pena, O. A. & Martin, P. (2024) Cellular and molecular mechanisms of skin wound healing. *Nat Rev Mol Cell*
913 *Biol*.

914 Radimerski, T., Montagne, J., Rintelen, F., Stocker, H., van der Kaay, J., Downes, C. P., Hafen, E. & Thomas, G.
915 (2002) dS6K-regulated cell growth is dPKB/dPI(3)K-independent, but requires dPDK1. *Nat Cell Biol*, 4(3), 251-5.

916 Rajan, A. & Perrimon, N. (2012) Drosophila cytokine unpaired 2 regulates physiological homeostasis by
917 remotely controlling insulin secretion. *Cell*, 151(1), 123-37.

918 Ring, N. A. R., Dworak, H., Bachmann, B., Schadl, B., Valdivieso, K., Rozmaric, T., Heimel, P., Fischer, I., Klinaki,
919 E., Gutasi, A., Schuetzenberger, K., Leinfellner, G., Ferguson, J., Drechsler, S., Mildner, M., Schosserer, M.,
920 Slezak, P., Meyuhas, O., Gruber, F., Grillari, J., Redl, H. & Ogrodnik, M. (2023) The p-rpS6-zone delineates
921 wounding responses and the healing process. *Dev Cell*, 58(11), 981-992 e6.

922 Rintelen, F., Stocker, H., Thomas, G. & Hafen, E. (2001) PDK1 regulates growth through Akt and S6K in
923 Drosophila. *Proc Natl Acad Sci U S A*, 98(26), 15020-5.

924 Romao, D., Muzzopappa, M., Barrio, L. & Milan, M. (2021) The Upd3 cytokine couples inflammation to
925 maturation defects in Drosophila. *Curr Biol*, 31(8), 1780-1787 e6.

926 Rybinski, B., Franco-Barraza, J. & Cukierman, E. (2014) The wound healing, chronic fibrosis, and cancer
927 progression triad. *Physiol Genomics*, 46(7), 223-44.

928 Santabarbara-Ruiz, P. & Leopold, P. (2021) An Oatp transporter-mediated steroid sink promotes tumor-induced
929 cachexia in Drosophila. *Dev Cell*, 56(19), 2741-2751 e7.

930 Santabarbara-Ruiz, P., Lopez-Santillan, M., Martinez-Rodriguez, I., Binagui-Casas, A., Perez, L., Milan, M.,
931 Corominas, M. & Serras, F. (2015) ROS-Induced JNK and p38 Signaling Is Required for Unpaired Cytokine
932 Activation during Drosophila Regeneration. *PLoS Genet*, 11(10), e1005595.

933 Saxton, R. A. & Sabatini, D. M. (2017) mTOR Signaling in Growth, Metabolism, and Disease. *Cell*, 168(6), 960-
934 976.

935 Schindelin, J., Arganda-Carreras, I., Frise, E., Kaynig, V., Longair, M., Pietzsch, T., Preibisch, S., Rueden, C.,
936 Saalfeld, S., Schmid, B., Tinevez, J. Y., White, D. J., Hartenstein, V., Eliceiri, K., Tomancak, P. & Cardona, A. (2012)
937 Fiji: an open-source platform for biological-image analysis. *Nat Methods*, 9(7), 676-82.

938 Semaniuk, U., Piskovatska, V., Strilbytska, O., Strutynska, T., Burdyliuk, N., Vaiserman, A., Bubalo, V., Storey, K.
939 B. & Lushchak, O. (2020) Drosophila insulin-like peptides: from expression to functions – a review. *Entomologia*
940 *Experimentalis et Applicata*, 169(2), 195-208.

941 Setiawan, T., Sari, I. N., Wijaya, Y. T., Julianto, N. M., Muhammad, J. A., Lee, H., Chae, J. H. & Kwon, H. Y. (2023)
942 Cancer cachexia: molecular mechanisms and treatment strategies. *J Hematol Oncol*, 16(1), 54.

943 Shimobayashi, M. & Hall, M. N. (2016) Multiple amino acid sensing inputs to mTORC1. *Cell Research.* Nature
944 Publishing Group.

945 Shin, M., Cha, N., Koranteng, F., Cho, B. & Shim, J. (2020) Subpopulation of Macrophage-Like Plasmatocytes
946 Attenuates Systemic Growth via JAK/STAT in the Drosophila Fat Body. *Front Immunol*, 11, 63.

947 Smith-Bolton, R. K., Worley, M. I., Kanda, H. & Hariharan, I. K. (2009) Regenerative growth in Drosophila
948 imaginal discs is regulated by Wingless and Myc. *Dev Cell*, 16(6), 797-809.

949 Song, W., Kir, S., Hong, S., Hu, Y., Wang, X., Binari, R., Tang, H. W., Chung, V., Banks, A. S., Spiegelman, B. &
950 Perrimon, N. (2019) Tumor-Derived Ligands Trigger Tumor Growth and Host Wasting via Differential MEK
951 Activation. *Dev Cell*, 48(2), 277-286 e6.

952 Stevens, L. J. & Page-McCaw, A. (2012) A secreted MMP is required for reepithelialization during wound
953 healing. *Mol Biol Cell*, 23(6), 1068-79.

954 Stine, Z. E., Schug, Z. T., Salvino, J. M. & Dang, C. V. (2022) Targeting cancer metabolism in the era of precision
955 oncology. *Nat Rev Drug Discov*, 21(2), 141-162.

956 Sudhakar, S. R., Pathak, H., Rehman, N., Fernandes, J., Vishnu, S. & Varghese, J. (2020) Insulin signalling elicits
957 hunger-induced feeding in Drosophila. *Dev Biol*, 459(2), 87-99.

958 Sun, F. & Poss, K. D. (2023) Inter-organ communication during tissue regeneration. *Development*, 150(23).

959 Sustar, A., Bonvin, M., Schubiger, M. & Schubiger, G. (2011) Drosophila twin spot clones reveal cell division
960 dynamics in regenerating imaginal discs. *Dev Biol*, 356(2), 576-87.

961 Sustar, A. & Schubiger, G. (2005) A transient cell cycle shift in Drosophila imaginal disc cells precedes
962 multipotency. *Cell*, 120(3), 383-93.

963 Ugrankar, R., Bowerman, J., Hariri, H., Chandra, M., Chen, K., Bossanyi, M. F., Datta, S., Rogers, S., Eckert, K. M.,
964 Vale, G., Victoria, A., Fresquez, J., McDonald, J. G., Jean, S., Collins, B. M. & Henne, W. M. (2019) Drosophila
965 Snazarus Regulates a Lipid Droplet Population at Plasma Membrane-Droplet Contacts in Adipocytes. *Dev Cell*,
966 50(5), 557-572 e5.

967 Vallejo, D. M., Juarez-Carreno, S., Bolivar, J., Morante, J. & Dominguez, M. (2015) A brain circuit that
968 synchronizes growth and maturation revealed through Dilp8 binding to Lgr3. *Science*, 350(6262), aac6767.

969 Wang, M. C., Bohmann, D. & Jasper, H. (2005) JNK extends life span and limits growth by antagonizing cellular
970 and organism-wide responses to insulin signaling. *Cell*, 121(1), 115-25.

971 Wei, X., Luo, L. & Chen, J. (2019) Roles of mTOR Signaling in Tissue Regeneration. *Cells*, 8(9).

972 Wong, K. K. L. & Verheyen, E. M. (2021) Metabolic reprogramming in cancer: Mechanistic insights from
973 Drosophila. *DMM Disease Models and Mechanisms.* Company of Biologists Ltd.

974 Worley, M. I., Alexander, L. A. & Hariharan, I. K. (2018) CtBP impedes JNK- and Upd/STAT-driven cell fate
975 misspecifications in regenerating Drosophila imaginal discs. *Elife*, 7.

976 Worley, M. I., Everetts, N. J., Yasutomi, R., Chang, R. J., Saretha, S., Yosef, N. & Hariharan, I. K. (2022) Ets21C
977 sustains a pro-regenerative transcriptional program in blastema cells of Drosophila imaginal discs. *Curr Biol*,
978 32(15), 3350-3364 e6.

979 Worley, M. I. & Hariharan, I. K. (2022) Imaginal Disc Regeneration: Something Old, Something New. *Cold Spring*
980 *Harb Perspect Biol*, 14(11).

981 Wu, X., Xie, W., Xie, W., Wei, W. & Guo, J. (2022) Beyond controlling cell size: functional analyses of S6K in
982 tumorigenesis. *Cell Death Dis*, 13(7), 646.

983 Yue, S., Li, G., He, S. & Li, T. (2022) The Central Role of mTORC1 in Amino Acid Sensing. *Cancer Res*, 82(17),
984 2964-2974.

985 Zheng, N., Wei, J., Wu, D., Xu, Y. & Guo, J. (2023) Master kinase PDK1 in tumorigenesis. *Biochim Biophys Acta*
986 *Rev Cancer*, 1878(6), 188971.

987 Zhu, J. & Thompson, C. B. (2019) Metabolic regulation of cell growth and proliferation. *Nat Rev Mol Cell Biol*,
988 20(7), 436-450.
989
990
991
992
993
994
995

996 **MAIN FIGURE LEGENDS**
997
998
999 **Figure 1. Spatial organization of cell proliferation and protein synthesis induced by**
1000 **inflammatory damage in wing imaginal disc.**
1001
1002 **A,B.** Control wing disc (A) and a genetically ablated wing disc (B) after 24 hours of *egr*-expression in
1003 the wing pouch domain (see Fig. 1C) under the control of the *rn*-GAL4 driver (rn^{ts} and rn^{ts}>*egr*,
1004 respectively). TRE-RFP visualizes JNK-pathway activity (magenta or grey), and EdU incorporation
1005 visualizes DNA replication (cyan or grey). Discs were stained with DAPI to visualize nuclei.
1006 **C.** Schematic representation of a third instar wing imaginal disc, highlighting different regions (pouch,
1007 notum, and hinge) on the left. On the right, schematic representation of a wing imaginal disc after 24
1008 hours of *egr*-expression in the pouch. The magenta area identifies the JNK-signaling domain
1009 representing inflammatory tissue damage.
1010 **D.** Quantification of average EdU intensity in the DAPI area contained within 10µm bands segmented
1011 inward and outward from the edge of the high JNK-signaling domain in *egr*-expressing discs. The high
1012 JNK-signaling domain is shaded in magenta, the proliferative domain marking the regenerating region
1013 is shaded in cyan. Mean and 95% CI (confidence interval) are shown. Statistical significance was
1014 tested using a one-way ANOVA followed by Tukey's post-hoc test for multiple comparisons (n=7). P-
1015 values: Band 1 vs Band 5 = 0.0001; Band 5 vs Band 8 = 0.0004; Band 1 vs Band 8 = 0.9984 (ns)
1016 **E,F.** Protein synthesis visualized by O-proparyl-puromycin (OPP) incorporation into newly synthesized
1017 proteins in a control wing disc (E) and an *egr*-expressing disc (F). Discs were stained with DAPI to
1018 visualize nuclei.
1019 **G.** Quantification of mean OPP intensity in three different regions of control and *egr*-expressing discs.
1020 In control disc, OPP intensity was measured in the pouch, hinge, and notum, while in *egr*-expressing
1021 discs, OPP intensity was measured in the high JNK signaling domain (approximating the central
1022 pouch), the proliferating region (approximating the peripheral pouch and hinge), and the notum. Mean
1023 and 95% CI are shown. Statistical significance was tested using a one-way ANOVA followed by
1024 Tukey's post-hoc test for multiple comparisons (control: n=8, *egr*-expressing disc: n=8). P-values:
1025 Proliferative region vs Quiescent notum < 0.0001; Notum vs Quiescent notum < 0.0001; Pouch vs JNK
1026 domain = 0.9992 (ns).
1027 **H, I.** Protein synthesis visualized by OPP incorporation in the notum of control (H) and *egr*-expressing
1028 discs (I).
1029 **J,K.** EdU incorporation to visualize DNA replication in the notum of control (J) and *egr*-expressing
1030 discs (K).
1031 **L.** EdU area per DAPI area quantified in the notum of control and *egr*-expressing discs, serving as a
1032 proxy for the number of cells undergoing DNA replication. Mean and 95% CI are shown. Statistical
1033 significance was tested using a two-tailed Unpaired t-test (control: n=9, *egr*-expressing disc: n=8), with
1034 a p-value = 0.0001.
1035 **M.** Mean EdU intensity per EdU-positive area quantified in the notum of control and *egr*-expressing
1036 discs, serving as a proxy for DNA replication speed. Mean and 95% CI are shown. Statistical
1037 significance was tested using a two-tailed Unpaired t-test (control: n=9, *egr*-expressing disc: n=8), with
1038 a p-value = 0.0011.
1039 **N.** Schematic representation of protein synthesis rates (blue shades) and mitotic activity (black dots)
1040 in control disc (left) and *egr*-expressing discs (right).
1041
1042 Scale bars: 100 µm. Fluorescence intensities are reported as arbitrary units.
1043
1044
1045 **Figure 2. Inflammatory tissue damage induces Insulin restriction and a systemic reduction in**
1046 **growth and cell proliferation.**
1047

A, B. Expression of Dilp8-GFP (cyan) in control (A) and *egr*-expressing discs (B). TRE-RFP visualizes JNK-pathway activity (magenta). Discs were stained with DAPI to visualize nuclei. dFOXO-GFP expression is visualized using BDSC 38644 fly line.

C. Levels of *dilp2* and *dilp5* mRNA relative to *Rpl1* mRNA were quantified in control, *egr*-expressing, and starved male larvae using quantitative PCR (qPCR). Day6 larvae were used for all conditions. Both genotypes, except starved larvae, undergo temperature shift for 24 hours. For experimental larvae *egr* expression was induced for 24h in the wing pouch using *rn*-GAL4 driver, while starved larvae underwent 24 h starvation. Mean and 95% CI are shown. Statistical significance was tested using the Kruskal-Wallis test followed by Dunn's multiple comparison test (control larvae: n=13, *egr*-expressing larvae: n=11, starved larvae: n=11). P-values for *dilp2*: Control vs egr = 0.0075; Control vs Starved < 0.0001; egr vs Starved = 0.1138 (ns). P-values for *dilp5*: Control vs egr = 0.0440; Control vs Starved < 0.0001; egr vs Starved = 0.0073.

D, E. Expression of dFOXO-GFP (cyan and grey) in the notum of control (D) and *egr*-expressing wing imaginal discs (E). Both genotypes were temperature-shifted for 24hours; in panel E, egr expression is restricted to the rotund domain of the wing disc. Discs were stained with DAPI (magenta and grey) to visualize nuclei. High nuclear translocation of dFOXO indicates low insulin signaling. BDSC: 38644 fly line was used. D' and E' show magnified view of the regions indicated by the yellow dotted boxes in panels D and E respectively.

F. Quantification of mean nuclear dFOXO-GFP intensity in the notum of control (D) and *egr*-expressing wing imaginal discs (E). Mean and 95% CI are shown. Statistical significance was tested using a two-tailed Unpaired t-test, p-value = 0.0427 (control: n=6, *egr*-expressing disc: n=8).

G, H. Protein synthesis visualized by OPP incorporation in the eye-antennal imaginal disc, dissected from larvae with control (G) or *egr*-expressing (H) wing imaginal discs using *salm*-GAL4 driver. The expression of *salm-GAL4* is localized to the central pouch.

I, J. EdU incorporation to visualizes DNA replication in eye-antennal imaginal discs, dissected from larvae with control (I) or *egr*-expressing (J) wing imaginal discs using *salm*-GAL4 driver. The dotted yellow line outlines the eye-antennal disc.

K, L. Protein synthesis visualized by OPP incorporation in the leg imaginal disc, dissected from larvae with control (K) or *egr*-expressing (L) wing imaginal discs using *salm*-GAL4 driver.

M, N. EdU incorporation to visualizes DNA replication in leg imaginal discs, dissected from larvae with control (M) or *egr*-expressing (N) wing imaginal discs using *salm*-GAL4 driver. The dotted yellow line outlines the leg disc.

O, P. Protein synthesis visualized by OPP incorporation in the eye imaginal disc, dissected from larvae with control (O) or *egr*-expressing (P) wing imaginal discs using *rn*-GAL4 driver.

Q. Quantification of mean OPP intensity in eye imaginal discs, dissected from larvae with control or *egr*-expressing wing imaginal discs. Mean and 95% CI are shown. Statistical significance was tested using a two-tailed Unpaired t-test, p-value = 0.0002 (control: n=5, *egr*-expressing disc: n=5).

R, S. EdU incorporation (magenta) to visualizes DNA replication in eye imaginal discs, dissected from larvae with control (R) or *egr*-expressing (S) wing imaginal discs using *rn*-GAL4 driver. Eye disc differentiating photoreceptors are marked with Elav staining (cyan).

T. Quantification of mean EdU intensity per EdU-positive area serving as a proxy for DNA replication speed, quantified in the eye imaginal discs dissected from larvae with control or *egr*-expressing wing imaginal discs. Mean and 95% CI are shown. Statistical significance was tested using the two-tailed Unpaired t-test, p-value = 0.0015 (control: n=6, *egr*-expressing disc: n=6).

U. A model illustrating expression of dILP-8 from senescent-like cells in the high JNK signaling domain. DILP-8 causes the downregulation of insulin-like peptides (dILP-2 and dILP-5) from insulin producing cells (IPCs) in the larval brain. This results in a systemic reduction of Insulin/Akt/FOXO signaling, leading to reduced protein synthesis and proliferation in peripheral tissues.

Scale bars: 100 µm. Fluorescence intensities are reported as arbitrary units.

Figure 3. Fat body catabolism and nutrient release to hemolymph facilitates regenerative proliferation through mTORC signaling pathway.

A, B. Nile Red staining (cyan or grey) of fat body, dissected from larvae with control (A) or *egr*-expressing (B) wing discs. Fat bodies were stained with DAPI (magenta) to visualize nuclei.

C. Quantification of area of lipid droplets in the fat body dissected from larvae with control (A) or *egr*-expressing (B) wing imaginal discs. Mean and 95% CI are shown. Statistical significance of was tested using a two-tailed Unpaired t-test. Mean area, p-value = 0.0004. (control: n=15, *egr*-expression in discs: n=18).

D, E. Triacylglycerides (TAG) levels were measured in *Drosophila* fat bodies dissected from third-instar larvae with *egr*-expressing wing disc, control larvae or starved larvae using thin-layer chromatography (TLC). Fat bodies from third instar larvae starved for 16hrs were used as a positive control. TAG levels were quantified per fat body in control, *egr*-expressing and starved larvae. Mean and 95% CI are shown. Statistical significance was tested using a one-way ANOVA followed by Dunnett's test for multiple comparison.(control larvae: n=9, *egr*-expressing larvae: n=9 and starved larvae: n=4). p-values: control vs egr = 0.0353; control vs starved =0.0076.

F, G. Expression of ImpL2-GFP in control (A) and *egr*-expressing discs (B). Discs were stained with DAPI to visualize nuclei.

H. Quantification of ImpL2-GFP intensity in control (**F**) and *egr*-expressing discs (**G**). Mean and 95% CI are shown, and statistical significance was tested using two-tailed Welch's t-test, p-value = 0.0001 (control: n=9, *egr*-expressing discs: n=11)

I, J. Nile Red staining of fat body (cyan or grey), dissected from larvae with control (I) or ImpL2-expressing under *rn*-GAL4 (J) in wing imaginal discs. Fat bodies were stained with DAPI (magenta) to visualize nuclei.

K. Quantification of area of lipid droplets in the fat body dissected from larvae with either control discs or wing imaginal discs expressing ImpL2 for 24 h under the control of *rn*-GAL4. For lipid droplet area, statistical significance was tested using the two-tailed Mann-Whitney test, p-value < 0.0001 (control: n=23, experiment: n=18). Mean and 95% CI are shown.

L. Heat map representing relative concentration changes of metabolites identified in the larval hemolymph isolated from control larvae and *egr*-expressing larvae. The heat map was generated using quantile normalized data, and statistical analysis was performed using a two-sided, unpaired Wilcoxon rank-sum test (see Materials and Methods) and metabolites with at least <0.75 and >1.5-fold change were selected for further analysis. Metabolites in the heat map are ordered based on the log2 fold change between control and *egr*-expressing larval samples and Z-scores were visualized. Sample size was n=3 for both control and *egr*-expressing larvae.

M, N. Expression of CG5535-GFP in control (cyan or grey) (M) and *egr*-expressing discs (N). TRE-RFP visualizes JNK-pathway activity (magenta).

O. Quantification of mean CG5535-GFP intensity quantified in the pouch of control discs and the proliferative domain of *egr*-expressing discs (PD^{egr}). Mean and 95% CI are shown. Statistical significance was tested using the two-tailed Unpaired t-test, p-value = 0.0092 (control: n=4, *egr*-expressing discs: n=5).

P, Q. Protein synthesis visualized by OPP incorporation in *egr*-expressing wing discs from larvae fed on food without (P) or with rapamycin (200 μM) (Q) for 24 h during the 24 h period of *egr*-expression in wing discs.

R. Quantification of mean OPP intensity in the pouch of control discs and the proliferative domain of *egr*-expressing discs (PD^{egr}) from larvae fed on food without or with rapamycin (200 μM) for 24 hours during the 24 h period of *egr*-expression in wing discs. Mean and 95% CI are shown. Statistical significance was tested using a one-way ANOVA followed by Tukey's post-hoc test for multiple comparisons (control: non-fed: n=9, fed: n=10 ; *egr*-expressing disc: non-fed: n=10, fed: n=10). PD^{egr} vs PD^{egr} + Rapamycin: $p < 0.0001$, Control + Rapamycin vs PD^{egr} + Rapamycin: $p = 0.0167$ and Control vs Control + Rapamycin: $p = 0.0017$.

S. A scheme highlighting the branch of TORC1 signaling driving S6K activation. Model illustrates how ImpL2 is secreted from senescent-like cells in the high JNK signaling domain, repressing fat body anabolism possibly via inducing insulin resistance, and thereby inducing nutrient mobilization from fat body. This branch may reinforce the metabolic switch induced by Insulin restriction. The released nutrients such as amino acids, enter the hemolymph and are subsequently taken up by the proliferative domain cells promoting mTORC1 growth signaling and S6K activation.

Scale bars: 100 μm. Fluorescence intensities are reported as arbitrary units.

Figure 4. Pdk1 is upregulated in the proliferative domain

A, B. Immunostaining for phosphorylated-S6 (pS6, cyan or grey) in control (A) and *egr*-expressing wing discs (B). TRE-RFP visualizes JNK-pathway activity (magenta or grey). Discs were stained with DAPI to visualize nuclei.
C. Quantification of mean p-S6 intensity in the pouch of control discs and the proliferative domain of *egr*-expressing discs (PD^{egr}). Mean and 95% CI are shown. Statistical significance was tested using the two-tailed Mann-Whitney test, p-value < 0.0001 (control: n=9, *egr*-expressing discs: n=9).
D. Schematic representation of canonical insulin signaling pathway, highlighting the insulin/Akt/FOXO axis. Phosphatidylinositol kinase-1 (Pdk1) is key serine/threonine kinase in this pathway.
E, F. Expression of dFOXO-GFP (cyan or grey) in control (E) and *egr*-expressing wing discs (F). TRE-RFP visualizes JNK-pathway activity (magenta or grey), and discs were stained with DAPI to visualize nuclei. Yellow dotted box marks the inset region. BDSC: 38644 fly line was used.
G. Quantification of mean nuclear dFOXO-GFP intensity in the pouch of control discs or the proliferative domain of *egr*-expressing discs (PD^{egr}). Mean and 95% CI are shown, and statistical significance was tested using the two-tailed Mann-Whitney test, p-value = 0.0006 (control: n=7, *egr*-expressing disc: n=7).
H, I. Expression of Pdk1-GFP (cyan or grey) in control (H) and *egr*-expressing discs (I). TRE-RFP visualizes JNK-pathway activity (magenta or grey), and discs were stained with DAPI to visualize nuclei. Yellow dotted box marks the inset region.
J. Quantification of Pdk1-GFP intensity in the pouch of control discs or the proliferative domain of *egr*-expressing discs (PD^{egr}). Statistical significance was tested using a two-tailed Welch's t-test, p-value = 0.0025 (control: n=10, *egr*-expressing disc: n=10). Mean and 95% CI are shown.
K. Expression of Pdk1-GFP in pro-apoptotic gene *hid*-expressing discs and DAPI visualizes nuclei. The yellow asterisk marks the damage or *hid*-expressing region. Discs were stained with DAPI to visualize nuclei.
L. Protein synthesis visualized by OPP incorporation in *hid*-expressing discs and DAPI visualizes nuclei. The yellow asterisk marks the damage or *hid*-expressing region. Discs were stained with DAPI to visualize nuclei.
M, N. Expression of Pdk1-GFP (cyan or grey) and p-S6 (magenta) in control (M) and *egr*-expressing wing discs (N).
Scale bars: 100 μm. Fluorescence intensities are reported as arbitrary units.

Figure 5. Pdk1 upregulation is sufficient and necessary for regenerative growth and proliferation.

A,B. Protein synthesis visualized by OPP incorporation in control wing discs (A) and discs expressing Pdk1 for 24 h under the control of *rn*-GAL4 driver (B). DAPI staining visualizes nuclei. The dotted yellow line indicates the boundary of the wing pouch based on landmark tissue folds, approximating the *rn*-GAL4 expression domain

C, D. EdU incorporation in control (C) and discs expressing UAS-Pdk1 for 24 h under the control of *rn*-GAL4 driver (D). DAPI staining visualizes nuclei. The dotted yellow line indicates the boundary of the wing pouch based on landmark tissue folds, approximating the *rn*-GAL4 expression domain

E. Quantification of mean OPP intensity in the pouch of control and *Pdk1*-expressing wing discs. Mean and 95% CI are shown, and statistical significance was tested using a two-tailed Unpaired t-test, p-value < 0.0001 (control: n=6, *Pdk1*-expressing disc: n=6).

F. Quantification of mean EdU intensity per DAPI area serving as a proxy for DNA replication speed, in the pouch of control and *Pdk1*-expressing wing discs. Mean and 95% CI are shown. Statistical significance was tested using the two-tailed Welch's t-test, p-value = 0.0078 (control: n=8, *Pdk1*-expressing disc: n=8).

G-J. Protein synthesis visualized by OPP incorporation in control (G, H) and *egr*-expressing wing discs (I, J) that were either wild type (G, I) or heterozygous mutant for the $Pdk1^5$ null allele (H, J). Discs were stained with DAPI to visualize nuclei.

K. Quantification of mean OPP intensity in the pouch of control or the proliferative domain of *egr*-expressing discs (PD^{egr}) that were either wild type or heterozygous mutant for the $Pdk1^5$ null allele. Statistical significance was tested using a one-way ANOVA followed by Tukey's post-hoc test for multiple comparisons. (control:n=6, control, $Pdk1^5$/+: n=6 ; *egr*:n=8, *egr,* $Pdk1^5$/+: n=7). PD^{egr} vs PD^{egr}*:* $Pdk1^5$/+ : p-value = 0.0300 and Control: $Pdk1^5$/+ vs PD^{egr} *:* $Pdk1^5$/+ : p-value= 0.0350. Mean and 95% CI are shown.

L, M. DUAL Control genetic ablation system (DCS) was used to manipulate gene expression in the proliferative domain. Early third instar (L3) larvae were heat shocked at 37°C for 1h and dissected after 24 h. A single heat shock activates both ablation (region inside the magenta dotted line) in the *salm* domain and gene manipulation in the proliferative domain via *dve*-GAL4 (the *dve-GAL4* expressing region is marked with a cyan dotted line). MMP1 is a target gene of JNK activated by eiger expression, thereby demarcating the ablated domain. Protein synthesis is visualized by OPP incorporation in wing imaginal discs in control (L) and Pdk1 knockdown (M) wing imaginal disc.

N. Quantification of mean OPP intensity in the proliferative domain using a 20 µm band around the ablated region of control (DCS^{egr}, ctrl) and *Pdk1* knockdown (DCS^{egr}*, Pdk1 RNAi*) wing imaginal discs with *egr* expression in the *salm* domain. On top, a simplified schematic illustrating the *egr*-expressed region (magenta) and the *dve-GAL4* expressing region (cyan) used for Pdk1 knockdown. Statistical significance was assessed using a two-tailed unpaired *t*-test ($p < 0.0001$). (*DCSegr*, control: $n = 10$; *DCSegr, Pdk1 RNAi*: $n = 9$). Mean and 95% CI are shown.

O. A scheme highlighting the branch of Pdk1 signaling driving S6K activation.

Scale bars: 100 µm. Fluorescence intensities are reported as arbitrary units.

1238 **Figure 6. Pdk1 is regulated by JAK/STAT signaling**

1239

1240 **A, B.** A control and *egr*-expressing wing imaginal disc with TRE-RFP (magenta) and Stat92E-dGFP
1241 (cyan) reporter. Discs were stained with DAPI to visualize nuclei.
1242 **C, E, G.** Wing imaginal discs expressing *STAT92E* in the posterior compartment under the control *en*-
1243 GAL4 driver which also drives expression of UAS-RFP. Discs were assayed for expression of Pdk1-
1244 GFP (C), levels of p-S6 (E), and protein synthesis using OPP incorporation assays (G). Discs were
1245 stained with DAPI to visualize nuclei.
1246 **D, F, H.** Quantifications of levels of Pdk1-GFP (D), p-S6 (F) and protein synthesis using OPP
1247 incorporation assays (H) using the posterior to anterior (P/A) ratio in control wing imaginal discs and
1248 wing imaginal discs expressing *STAT92E* in the posterior compartment under the control *en*-GAL4. In
1249 the graph displaying Pdk1-GFP intensity (D), statistical significance was tested using the two-tailed
1250 Unpaired t-test, p-value < 0.0001 (control: n=5, experiment: n=8). In the graph displaying p-S6 intensity
1251 (F), statistical significance was tested using two-tailed Welch's t-test, p-value = 0.0033 (control: n=5,
1252 experiment: n=8). In the graph displaying OPP intensity (H), statistical significance was tested using
1253 the two-tailed Unpaired t-test, p-value = 0.0004 (control: n=5, experiment: n=5). Mean and 95% CI are
1254 shown.
1255 **I, J.** Control wing disc (I) and wing imaginal discs expressing *STAT92E-RNAi* (J) in the posterior
1256 compartment under the control *en*-GAL4 driver which also drives expression of UAS-RFP. Discs were
1257 assayed for expression of Pdk1-GFP and protein synthesis using OPP incorporation assays. Discs
1258 were stained with DAPI to visualize nuclei.
1259 **K.** Quantifications of Pdk1-GFP levels using the posterior to anterior (P/A) ratio in control wing imaginal
1260 discs and wing imaginal discs expressing *STAT92E-RNAi* in the posterior compartment under the
1261 control *en*-GAL4 driver. Statistical significance was tested using the two-tailed Welch's t-test, p-value
1262 = 0.0004 (control: n=8, experiment: n=10). Mean and 95% CI are shown.
1263 **L.** Quantifications protein synthesis levels using the OPP posterior to anterior (P/A) ratio in control
1264 wing imaginal discs and wing imaginal discs expressing *STAT92E-RNAi* in the posterior compartment
1265 under the control *en*-GAL4 driver. Statistical significance was tested using the two-tailed Unpaired t-
1266 test, p-value < 0.0001 (control: n=8, experiment: n=10). Mean and 95% CI are shown.
1267 **M, N.** Protein synthesis visualized by OPP incorporation in *egr*-expressing discs that were either wild
1268 type (M) or heterozygous mutant for the $Stat92E^{85C9}$ null allele (N). Discs were stained with DAPI to
1269 visualize nuclei.
1270 **O.** Quantification of mean OPP intensity in the pouch of control and the proliferative domain of *egr*-
1271 expressing discs (PD^{egr}) that were either wild type or heterozygous mutant for the $Stat92E^{85C9}$ null
1272 allele. Statistical significance was tested using a one-way ANOVA followed by Tukey's post-hoc test
1273 for multiple comparisons. (control:n=7, control, $Stat92E^{85C9}$/+: n=7 ; *egr*:n=7, *egr,* $Stat92E^{85C9}$/+: n=7).
1274 PD^{egr} vs PD^{egr} *:*$Stat92E^{85C9}$/+ : p-value = 0.0080 and Control*:* $Stat92E^{85C9}$/+ vs PD^{egr} *:* $Stat92E^{85C9}$/+ :
1275 p-value =0.0005. Mean and 95% CI are shown.
1276 **P, Q.** A DUAL Control genetic ablation system (DCS) was used to manipulate gene expression in the
1277 proliferative domain. Early third instar (L3) larvae were heat shocked at 37°C for 75min and dissected
1278 after 40 h. A single heat shock activated both ablation (region inside the magenta dotted line) in the
1279 *salm* domain and gene manipulation in the proliferative domain via *dve*-GAL4 (*dve-GAL4* expressing
1280 region is marked with a cyan dotted line). Protein synthesis visualized by OPP incorporation in control
1281 (P) and *Stat92E* knockdown (Q) wing imaginal disc.
1282 **R.** Quantification of mean OPP intensity in the proliferative domain using a 20 µm band around the
1283 ablated region of control (DCS^{egr}) and *STAT92E* knockdown (*DCS*^{egr}*, Stat92E-RNAi*) wing imaginal
1284 discs with *egr* expression in the *salm* domain. Mean and 95% CI are shown. Statistical significance
1285 was assessed using a two-tailed Mann-Whitney's test, *p value* = 0.0006. (*DCSegr*, control: *n* = 7;
1286 *DCSegr, Stat92E- RNAi*: *n* = 8).
1287 **S.** A scheme highlighting that JAK/STAT activation positively affects Pdk1 activity towards S6K.

1288

1289 Scale bars: 100 µm. Fluorescence intensities are reported as arbitrary units.

1290
1291
1292 **Figure 7. Pdk1 upregulation, protein translation and JAK/STAT signaling are linked in tumor**
1293 **growth**
1294
1295 **A, B.** Control wing disc (A) and wing disc expressing *Ras^{V12}, scrib-RNAi* (B) for 44h starting at Day6
1296 AED. Protein synthesis is visualized by OPP incorporation (cyan or grey) in control (A) and *Ras^{V12},*
1297 *scrib-RNAi* expressing wing disc (B) along with expression of the JAK/STAT reporter Stat92E-dGFP
1298 (magenta or grey). Discs were stained with DAPI to visualize nuclei.
1299 **C**. Quantification of mean OPP intensity in the STAT positive and STAT negative region within a
1300 *Ras^{V12}, scrib-RNAi* expressing wing discs. Mean and 95% CI are shown. Statistical significance was
1301 tested using the two-tailed Paired t-test, p-value = 0.0006 (control: n=6, experiment: n=6).
1302 **D, E.** Control wing disc and wing disc expressing *Ras^{V12}, scrib-RNAi* for 44h starting at Day6 AED.
1303 Expression of Pdk1-GFP (cyan or grey) in control (D) and *Ras^{V12}, scrib-RNAi* expressing wing disc
1304 (E) along with MMP1 staining to visualizes JNK-pathway activity (magenta or grey). Discs were
1305 stained with DAPI to visualize nuclei.
1306 **F**. Quantification of mean Pdk1-GFP intensity in the control disc pouch and *Ras^{V12}, scrib-RNAi*
1307 expressing wing discs pouch. Statistical significance was tested using the two-tailed Unaired t-test,
1308 p-value = 0.0004 (control: n=10, experiment: n=10). Mean and 95% CI are shown.
1309 **G, H**. Protein synthesis visualized by OPP incorporation in the notum of control wing disc (G) and
1310 wing disc expressing *Ras^{V12}, scrib-RNAi* (H) for 44h starting at Day6 AED. Discs were stained with
1311 DAPI to visualize nuclei.
1312 **I.** Quantification of mean OPP intensity in the notum of control wing disc and wing disc expressing
1313 *Ras^{V12}, scrib-RNAi*. Statistical significance was tested using the two-tailed Welch's t-test, p-value =
1314 0.0031 (control: n=6, experiment: n=6). Mean and 95% CI are shown.
1315
1316 Scale bars: 100 µm.
1317
1318
1319 **Figure 8. Pdk1 downregulation in peripheral discs correlates with systemic growth restriction**
1320
1321 **A, B.** Expression of Pdk1-GFP in the notum of control (A) and *egr*-expressing discs (B). Discs were
1322 stained with DAPI to visualize nuclei.
1323 **C**. Quantification of mean Pdk1-GFP intensity in the notum of control (A) and *egr*-expressing discs
1324 (B). Mean and 95% CI are shown. Statistical significance was tested using the two-tailed Mann-
1325 Whitney's test, p-value = 0.0007 (control: n=10, experiment: n=10).
1326 **D, E.** Expression of Pdk1-GFP in the eye imaginal disc, dissected from larvae with control (D) or *egr*-
1327 expressing (E) wing imaginal discs using *rn*-GAL4 driver. Discs were stained with DAPI to visualize
1328 nuclei.
1329 **F**. Quantification of mean Pdk1-GFP intensity in the eye imaginal disc, dissected from larvae with
1330 control (D) or *egr*-expressing (E) wing imaginal discs. Mean and 95% CI are shown. Statistical
1331 significance was tested using the two-tailed Unpaired t-test, p-value < 0.0001 (control: n=7,
1332 experiment: n=7).
1333 **G, H**. Expression of Pdk1-GFP in the notum of control wing disc (G) and wing disc expressing
1334 *Ras^{V12}, scrib-RNAi* (H) for 44h starting at Day6 AED. Discs were stained with DAPI to visualize
1335 nuclei.
1336 **I.** Quantification of mean Pdk1-GFP intensity in the notum of control wing disc and wing disc
1337 expressing *Ras^{V12}, scrib-RNAi*. Mean and 95% CI are shown. Statistical significance was tested
1338 using the two-tailed Unpaired t-test, p-value = 0.0022 (control: n=5, experiment: n=6).
1339 **J**. A model summary illustrating growth signaling mediated by S6K activation via canonical Insulin
1340 signaling (Insulin/AKT/FOXO and mTORC1) during normal developmental (left). On the right, growth

signaling in the proliferative domain is maintained in an insulin restricted environment through the JAK/STAT-Pdk1-S6K axis, supported by mTORC1 signaling.

K. A model summary depicting the interaction between local and systemic metabolism to support growth in the proliferative domain. Inter-organ signaling is initiated by senescent-like cells in the high JNK signaling domain at the center of tissue damage via secreted Dilp8, ImpL2 and Upd1,2,3. Dilp8 reduces insulin-like peptide expression by acting on IPCs, thereby restricting systemic insulin signaling in peripheral tissues. Additionally, ImpL2 acts on the fat body, and combined both mechanisms facilitates nutrient mobilization from fat body stores. Secreted Unpaired ligands activate JAK/STAT signaling in the nearby proliferative domain, upregulating Pdk1 and instructing S6K activation. Levels of Pdk1 in the proliferative and peripheral regions determines the tissues growth status in an insulin-restricted environment.

1355 **SUPPLEMENTARY FIGURE LEGENDS**
1356
1357
1358 **Figure S1. Cell cycle adaptations in response to inflammatory tissue damage**
1359
1360 **A, B.** Control wing disc (A) and a wing discs (B) after 24 hours of *egr*-expression within the wing pouch
1361 domain under the control of the *rn*-GAL4 driver (rn^{ts} and rn^{ts}>*egr*, respectively). A co-expressed UAS-
1362 GFP construct visualizes the *rn*-GAL4 expression domain. Staining for cleaved Dcp-1 visualizes
1363 apoptosis. Discs were stained with DAPI to visualize nuclei. Please note the GFP-expression domain
1364 in (B) which does not stain for cDcp-1 and represents surviving cells with high levels of JNK activity.
1365 Levels of Dcp-1 were previously quantified (La Fortezza, Schenk et al. 2016, Cosolo, Jaiswal et al.
1366 2019, Jaiswal, Egert et al. 2023).
1367
1368 **C, D.** Analysis of senescence-associated β-galactosidase (SA-β-gal) activity (cyan or grey) in control
1369 (C) and *egr*-expressing wing disc (D). TRE-RFP visualizes JNK-pathway activity. Discs were stained
1370 with DAPI to visualize nuclei (magenta or grey). SA-β-gal activity was already previously reported and
1371 quantified (Floc'hlay, Balaji et al. 2023, Jaiswal, Egert et al. 2023).
1372
1373 Scale bars: 100 µm.
1374
1375
1376 **Figure S2. Metabolic adaptation in peripheral tissues**
1377
1378 **A, B.** Nota of control (A) and wing disc expressing *egr* in the pouch (B). TRE-RFP visualizes JNK-
1379 pathway activity and staining for cleaved Dcp-1 visualizes apoptosis. Discs were stained with DAPI to
1380 visualize nuclei.
1381 **C, D.** EdU incorporation to visualize DNA replication in leg imaginal discs, dissected from larvae
1382 containing either control wing disc (C) or *egr*-expressing wing discs (D). Discs were stained with DAPI
1383 to visualize nuclei.
1384 **E.** Mean EdU intensity per EdU-positive area quantified in leg imaginal discs, dissected from larvae
1385 containing either control wing disc (C) or *egr*-expressing wing discs (D), serving as a proxy for DNA
1386 replication speed. Mean and 95% CI are shown. Statistical significance was tested using an two-tailed
1387 Unpaired t-test with a p-value = 0.0154 (control: n=6, *egr*-expressing disc: n=6).
1388 **F, G.** Protein synthesis visualized by O-proparyl-puromycin (OPP) incorporation into newly
1389 synthesized proteins in leg imaginal discs, dissected from larvae containing either control wing disc
1390 (F) or *egr*-expressing wing discs (G). Discs were stained with DAPI to visualize nuclei.
1391 **H, I.** EdU incorporation (cyan or grey) to visualizes DNA replication in eye imaginal discs, dissected
1392 from larvae with control (H) or *egr*-expressing (I) wing imaginal discs. Eye disc differentiating
1393 photoreceptors are marked with Elav staining (magenta or grey). Sum projection of multiple image
1394 slices to visualize the second mitotic wave (SMW) and the yellow arrowheads point to the expected
1395 location of the SMW.
1396 **J, K.** Protein synthesis visualized by OPP incorporation in the eye imaginal disc (same as **Fig 2.O and**
1397 **P**), dissected from larvae with control (J,) or *egr*-expressing (K) wing imaginal discs using *rn*-GAL4
1398 driver. TRE-RFP visualizes JNK-pathway activity and discs were stained with DAPI to visualize nuclei.
1399
1400 Scale bar: 100 µm.
1401
1402

1403 **Figure S3.1 Elevated levels of nutrient transporters and mTORC1 signaling support**
1404 **regenerative proliferation**
1405
1406 **A.** Quantification of roundness of lipid droplets in the fat body dissected from larvae with control
1407 (**Fig.3A**) or *egr*-expressing (**Fig.3B**) wing imaginal discs. Mean and 95% CI are shown. Roundness is
1408 measured as the ratio of the area to the square of the length of the major axis. A perfect circle has a
1409 roundness value of 1, while values approaching zero indicate a more elongated shape. Statistical
1410 significance of was tested using an two-tailed Unpaired t-test. Mean roundness, p-value < 0.0001.
1411 (control: n=15, *egr*-expression in discs: n=18).
1412 **B**. Protein expression levels of p-AKT (Ser473) and AKT by western blot in the fat body dissected from
1413 larvae with control or *egr*-expressing wing imaginal discs or 24 h starved larvae.
1414 **C, D.** Expression of dFOXO-GFP (cyan or grey) in fat body, dissected from larvae with control (I) or
1415 *egr*-expressing (J) wing imaginal discs. Fat bodies were stained with DAPI to visualize nuclei
1416 (magenta).
1417 **E.** Mean nuclear dFOXO-GFP intensity in fat body, dissected from larvae with control or *egr*-
1418 expressing wing imaginal discs. Statistical significance was tested using an two-tailed unpaired t-test,
1419 p-value = 0.0003 (control: n=10, *egr*-expressing disc: n=9).
1420 **F, G**. Expression of Upd3-lacZ in control (C) and *egr*-expressing discs (D). Discs were stained with
1421 DAPI to visualize nuclei.
1422 **H.** Upd3-lacZ intensity quantified in the pouch of control wing discs and in the JNK-signaling domain
1423 of *egr*-expressing discs. Mean and 95% CI are shown and statistical significance was tested using
1424 two-tailed Welch's t-test with p-value < 0.0001 (control: n=8, *egr*-expressing disc: n=9).
1425 **I.** Quantification of roundness of lipid droplets in the fat body dissected from larvae with either control
1426 discs or wing imaginal discs expressing ImpL2 for 24 h under the control of *rn*-GAL4. Roundness is
1427 measured as the ratio of the area to the square of the major axis. A perfect circle has a roundness
1428 value of 1, while values approaching zero indicate more elongated shape. Statistical significance was
1429 tested using the two-tailed Unpaired t-test, p-value=0.0088 (control: n=24, *egr*-expression in disc:
1430 n=18).
1431 **J, K.** Activity of the JAK/STAT reporter *STAT92E-GFP* in the fat body dissected from larvae with control
1432 (J) or *egr*-expressing (K) wing imaginal discs. DAPI visualizes nuclei.
1433 **L.** Quantification of *STAT92E-GFP* reporter intensity in the fat body dissected from larvae with control
1434 or *egr*-expressing wing imaginal discs. Mean and 95% CI are shown and statistical significance was
1435 tested using the two-tailed Mann-Whitney test, p-value < 0.0001 (control: n=12, *egr*-expression in disc:
1436 n=14).
1437 **M, N.** *Drosophila* larval body wall muscles dissected from larvae containing either control (M) or *egr*-
1438 expressing (N) wing discs. Actin was visualized using Phalloidin and TRE-RFP visualizes JNK-
1439 pathway activation. Muscles were stained with DAPI to visualize nuclei. Please note that muscles do
1440 not activate JNK-signaling in response to inflammatory cues.
1441 **O, P.** Nota of control (O) and *egr*-expressing wing disc (P) stained for the autophagy marker Ref(2)P.
1442 Discs were stained with DAPI to visualize nuclei.
1443 **Q, R.** Staining for the putative alanine, glycine and proline amino acid transporter Arcus (CG1139) in
1444 control (Q) and *egr*-expressing discs (R). TRE-RFP visualizes JNK-pathway activation. Discs were
1445 stained with DAPI to visualize nuclei.
1446 **S, T.** Expression of Tret1.1-GFP in control (S) and *egr*-expressing discs (T). TRE-RFP visualizes JNK-
1447 pathway activation. Discs were stained with DAPI to visualize nuclei.
1448 **U.** Mean Tret1.1-GFP intensity quantified in the pouch of control discs and the proliferative domain of
1449 *egr*-expressing discs. Mean and 95% CI are shown. Statistical significance was tested using the two-
1450 tailed Welch's t-test, p-value < 0.0001 (control: n=5, *egr*-expressing discs: n=9).
1451 **V, W.** Protein synthesis visualized by OPP incorporation in control (V) and larvae fed on food with
1452 rapamycin (200 μM) (W) for 24 h during the temperature shift.
1453 Scale bar: 100 μm. Fluorescence intensities are reported as arbitrary units.
1454

Figure S3.2 Elevated levels of nutrient transporters and mTORC1 signaling support regenerative proliferation

A.B UMAP plots generated using the Scope Wing Atlas created from control and *egr*-expressing discs analysed by single-cell RNA-Seq technology (Floc'hlay, Balaji et al. 2022). Different cell populations are color-coded. The analysis in (Floc'hlay, Balaji et al. 2022) indicating the emergence of a 'wound' cluster in *egr*-expressing discs, subdivided into two clusters with signatures characteristic of senescent cells (beta) and with characteristic of a cell and tissue damage response signature (alpha).

C. ScRNA-Seq UMAP plots showing the elevated transcript levels of secreted paracrine ligands with known interorgan signaling roles. Grey indicates low expression, and red indicates high expression of transcripts.

D. scRNA-Seq UMAP plot displaying significantly elevated transcript levels detected for different nutrient transporters and S6K (Floc'hlay, Balaji et al. 2023). Grey indicates low expression, and red indicates high expression of transcripts.

Figure S4. Insulin/PI3K/Akt signaling is low in the proliferative domain.

A,B. Expression of dFOXO-GFP (cyan or grey) in control (A) and *egr*-expressing discs (B). TRE-RFP visualizes JNK-pathway activity (magenta or grey) and DAPI visualizes nuclei (grey). dFOXO-GFP expression is visualized using BDSC 59766 fly line.
C. Mean nuclear dFOXO-GFP intensity quantified in the pouch of control discs or the proliferative domain of *egr*-expressing discs (PD^{egr}). Mean and 95% CI are shown and statistical significance was tested using the two-tailed Mann-Whitney test, p-value = 0.0006 (control: n=7, *egr*-expressing disc: n=7).
D-G. Control (D, F) and *egr*-expressing wing discs (E, G), expressing an Insulin receptor tagged with GFP (InR-GFP) (D, E) or stained for Akt (F, G) (cyan or grey). TRE-RFP visualizes JNK-pathway activity (magenta or grey). Discs were stained with DAPI to visualize nuclei.
H. Anti-phospho-Akt (S505) staining (cyan or grey) to test antibody specificity in UAS-Akt-overexpressing clones marked by co-expression of UAS-GFP (magenta or grey) in the wing imaginal disc. Discs were stained with DAPI to visualize nuclei.
I, J. Control (I) and *egr*-expressing wing discs (J), stained for phospho-Akt (S505) (cyan or grey). TRE-RFP visualizes JNK-pathway activity (magenta or grey). Discs were stained with DAPI to visualize nuclei.
K. Quantification of mean p-AKT intensity in the control pouch and proliferative domain of *egr*-expressing wing discs. Mean and 95% CI are shown and statistical significance was tested using a two-tailed Unpaired t-test , p-value =0.0156. (Control; n=4, *egr*-expressing discs; n=5).
L. Expression of Pdk1-GFP in the control wing imaginal disc corresponding to pro-apoptotic *hid*-expressing discs shown in **Fig4.K**. DAPI visualizes nuclei.
M. Protein synthesis visualized by OPP incorporation in the control wing imaginal disc corresponding to *hid*-expressing discs shown in **Fig4.L**. DAPI visualizes nuclei.
N, O. Expression of Pdk1-GFP in the control and pro-apoptotic gene Reaper (*rpr*) expressing discs. The yellow asterisk marks the damage or *rpr*-expressing region. DAPI visualizes nuclei.
P, Q. Protein synthesis visualized by OPP incorporation in the control and pro-apoptotic gene Reaper (*rpr*) expressing discs. The yellow asterisk marks the damage or *rpr*-expressing region. DAPI visualizes nuclei.

Scale bar: 100 µm.

1506 **Figure S5. Pdk1-GFP is necessary and sufficient to drive protein translation in the regenerative**
1507 **domain.**
1508
1509 **A, B.** Protein synthesis visualized by OPP incorporation in control (A) and discs expressing a
1510 constitutively active UAS-Pdk1 (B) for 24 h under the control of *rn*-GAL4. Discs were stained with DAPI
1511 to visualize nuclei. The dotted white line marks the border of the pouch using tissue fold landmarks.
1512 **C.** Quantification of mean OPP intensity in the pouch of control and $Pdk1^{CA}$-expressing wing discs.
1513 Mean and 95% CI are shown and statistical significance was tested using two-tailed Mann-Whitney
1514 test. p-value = 0.0062. (Control; n=8, $Pdk1^{CA}$-expressing discs; n=10).
1515 **D.** Quantification of the pouch area in control and $Pdk1^{CA}$-expressing wing discs. Mean and 95% CI
1516 are shown and statistical significance was tested using two-tailed Unpaired t-test. p-value = 0.0003.
1517 (Control; n=9, $Pdk1^{CA}$-expressing discs; n=8).
1518 **E.** Pdk1-GFP expression in the posterior compartment of the wing imaginal disc following Pdk1
1519 knockdown using *en*-GAL4 to test the efficiency of Pdk1-RNAi line (BL27725). *en*-GAL4 which also
1520 drives expression of UAS-RFP expression to mark the posterior compartment. DAPI stains nuclei.
1521 **F**. A simplified schematic representing DUAL control genetic ablation system (DCS). The genetically
1522 ablated region expresses *egr* under the control of *salm-lexADBD::p65 lexAOP* (marked in magenta),
1523 while *dve*-GAL4 is used to manipulate gene expression in the proliferative domain (cyan) surrounding
1524 the *egr* expressing region.
1525
1526 Scale bar: 100 µm. Fluorescence intensities are reported as arbitrary units.
1527
1528
1529 **Figures S6. Pdk1 is regulated by JAK/STAT signaling**
1530
1531 **A, B.** Control and *egr*-expressing discs stained for EdU to visualize DNA replication in discs also co-
1532 expressing a *Stat92E-GFP* activity reporter. Discs were also stained with DAPI to visualize nuclei. EdU
1533 intensity in *Stat92E-GFP* reporter-expressing domain was previously quantified (Jaiswal, Egert et al.
1534 2023).
1535 **C, D, E.** Corresponding control discs to the wing imaginal discs expressing UAS-STAT92E in the
1536 posterior compartment under the control *en*-GAL4 in **Fig 6.C, E and G**. Control discs were assayed
1537 for expression of Pdk1-GFP (C), levels of p-S6 (D), and protein synthesis using OPP incorporation
1538 assays (E). *en*-GAL4 also drives expression of UAS-RFP and DAPI staining visualizes nuclei. Yellow
1539 dotted box marks the inset region.
1540 **F,G.** Protein synthesis visualized by OPP incorporation in wing discs that were either wild type (F) or
1541 heterozygous mutant for the $Stat92E^{85C9}$ null allele (G). DAPI staining visualizes nuclei.
1542 **H, I.** Corresponding DAPI staining of wing imaginal discs expressing the DUAL Control genetic ablation
1543 system (DCS) shown in **Fig 6.P and Q**. Early third instar (L3) larvae were heat shocked at 37°C for
1544 75min and dissected after 40 h. A single heat shock activated both ablation (region inside the magenta
1545 dotted line) in the *salm* domain and gene manipulation in the proliferative domain via *dve*-GAL4 (*dve-*
1546 *GAL4* expressing region is marked with a cyan dotted line). Nuclei were visualized by DAPI staining
1547 in control (H) and *Stat92E* knockdown (I) wing imaginal disc.
1548 **J.** A model of the JAK/STAT-Pdk1-S6K axis active in proliferating cells of *egr*-expressing discs.
1549 Unpaired ligands provided by senescent-like cells in the high JNK signaling domain activating
1550 JAK/STAT in the surrounding proliferative domain, leading to Pdk1 upregulation and insulin-
1551 independent growth.
1552
1553 Scale bar: 100 µm. Fluorescence intensities are reported as arbitrary units.
1554
1555

1556 **Figures S7. Protein translation and JAK/STAT signaling are linked in tumor growth**
1557
1558 **A.** Wing disc expressing *Ras^{V12}, scrib-RNAi* for 44h starting at Day6 AED. The disc also expresses the
1559 JAK/STAT activity reporter *Stat92E-dGFP* (cyan or grey) and JNK/AP1 reporter TRE-RFP (magenta
1560 or grey). DAPI staining visualizes nuclei.
1561
1562 **B, C.** Control wing disc (B) and wing disc with mosaic clones mutant for the Polycomb family genes
1563 *Psc-Su(z)2^{XL26}* (GFP negative cells, C). Protein synthesis visualized by OPP incorporation (cyan or
1564 grey) and JAK/STAT activity assessed using *Stat92E-dGFP* reporter (magenta or grey). DAPI staining
1565 visualizes nuclei.
1566
1567 Scale bar: 100 µm.
1568
1569
1570
1571 **Figures S8. Pdk1 downregulation in peripheral discs correlates with systemic growth**
1572 **restriction**
1573
1574 **A, B.** Expression of Pdk1-GFP in the notum of control (A) and *egr*-expressing discs in discs expressing
1575 the DUAL control genetic ablation system driving *egr*-expression (B). JNK/AP1 activation assessed by
1576 MMP1 staining. DAPI staining visualizes nuclei.
1577 **C, D.** Expression of Pdk1-GFP in the leg imaginal disc, dissected from larvae with control (c) or *egr*-
1578 expressing (D) wing imaginal discs expressed using the *rn*-GAL4 driver.
1579 **E**. Quantification of mean Pdk1-GFP intensity in the leg imaginal disc, dissected from larvae with
1580 control (C) or *egr*-expressing (D) wing imaginal discs. Statistical significance was tested using the two-
1581 tailed Unpaired t-test, p-value = 0.0001 (control: n=5, experiment: n=5).
1582
1583
1584
1585
1586
1587
1588

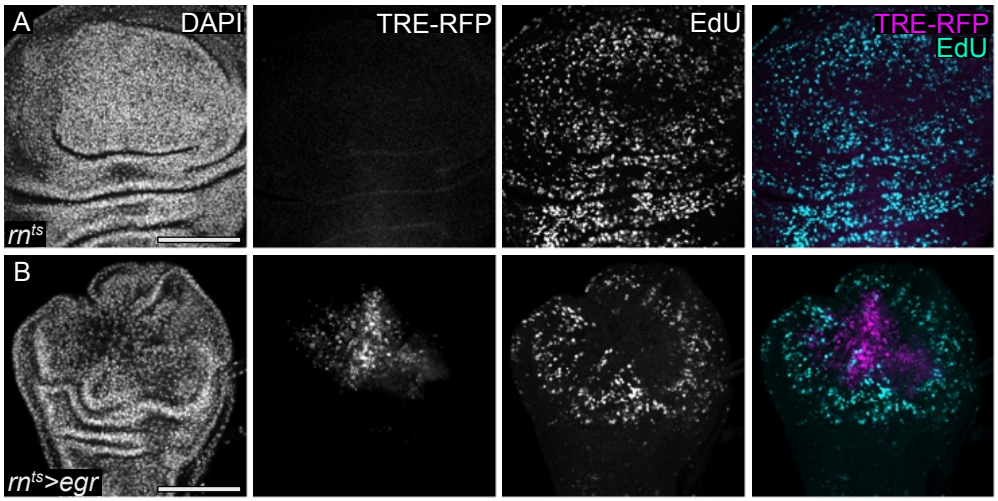
A
DAPI
TRE-RFP
EdU
TRE-RFP
EdU
rn^ts
B
rn^ts>egr

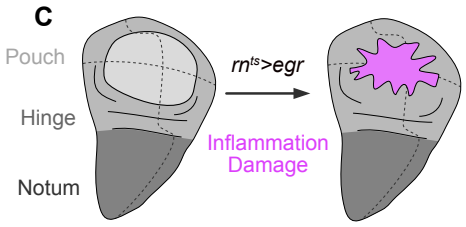
C
Pouch
Hinge
Notum
rn^ts>egr
Inflammation
Damage

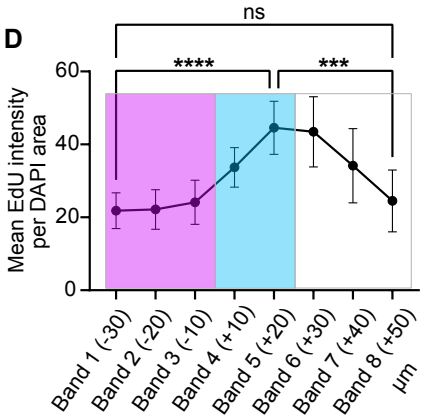
D
ns
****
***
Mean EdU intensity per DAPI area
60
40
20
0
Band 1 (-30)
Band 2 (-20)
Band 3 (-10)
Band 4 (+10)
Band 5 (+20)
Band 6 (+30)
Band 7 (+40)
Band 8 (+50)
µm

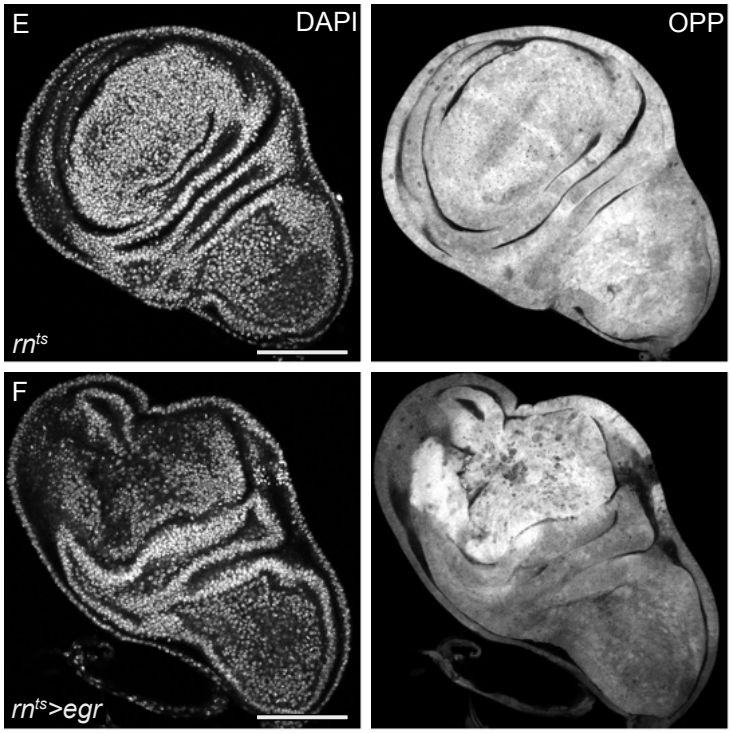
E
DAPI
OPP
rn^ts
F
rn^ts>egr

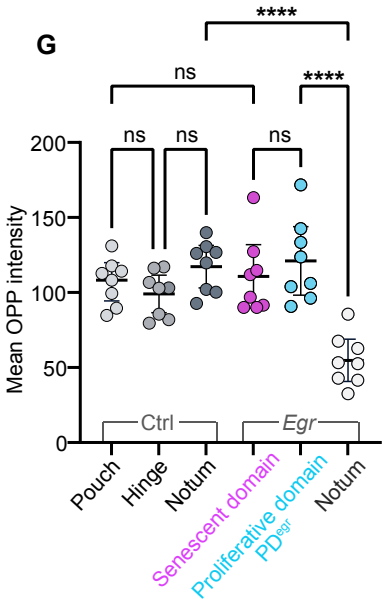
G
****
ns
****
ns
ns
ns
Mean OPP intensity
200
150
100
50
0
Ctrl
Egr
Pouch
Hinge
Notum
Senescent domain
Proliferative domain
PD^egr
Notum

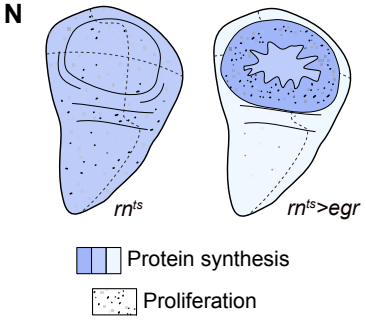
N
rn^ts
rn^ts>egr
Protein synthesis
Proliferation

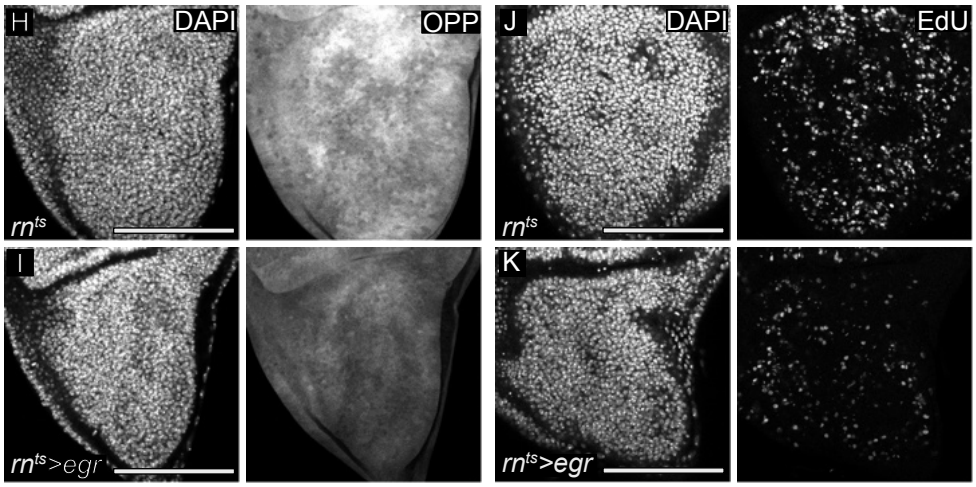
H
DAPI
OPP
rn^ts
I
rn^ts>egr
J
DAPI
EdU
rn^ts
K
rn^ts>egr

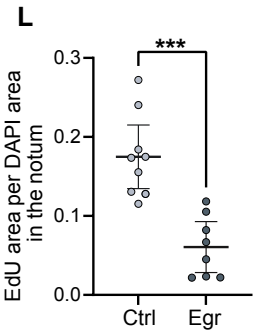
L
***
EdU area per DAPI area in the notum
0.3
0.2
0.1
0.0
Ctrl
Egr

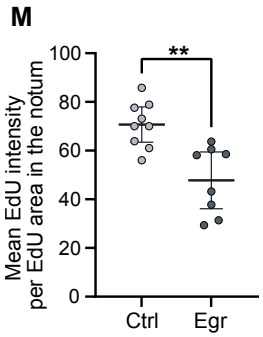
M
**
Mean EdU intensity per EdU area in the notum
100
80
60
40
20
0
Ctrl
Egr

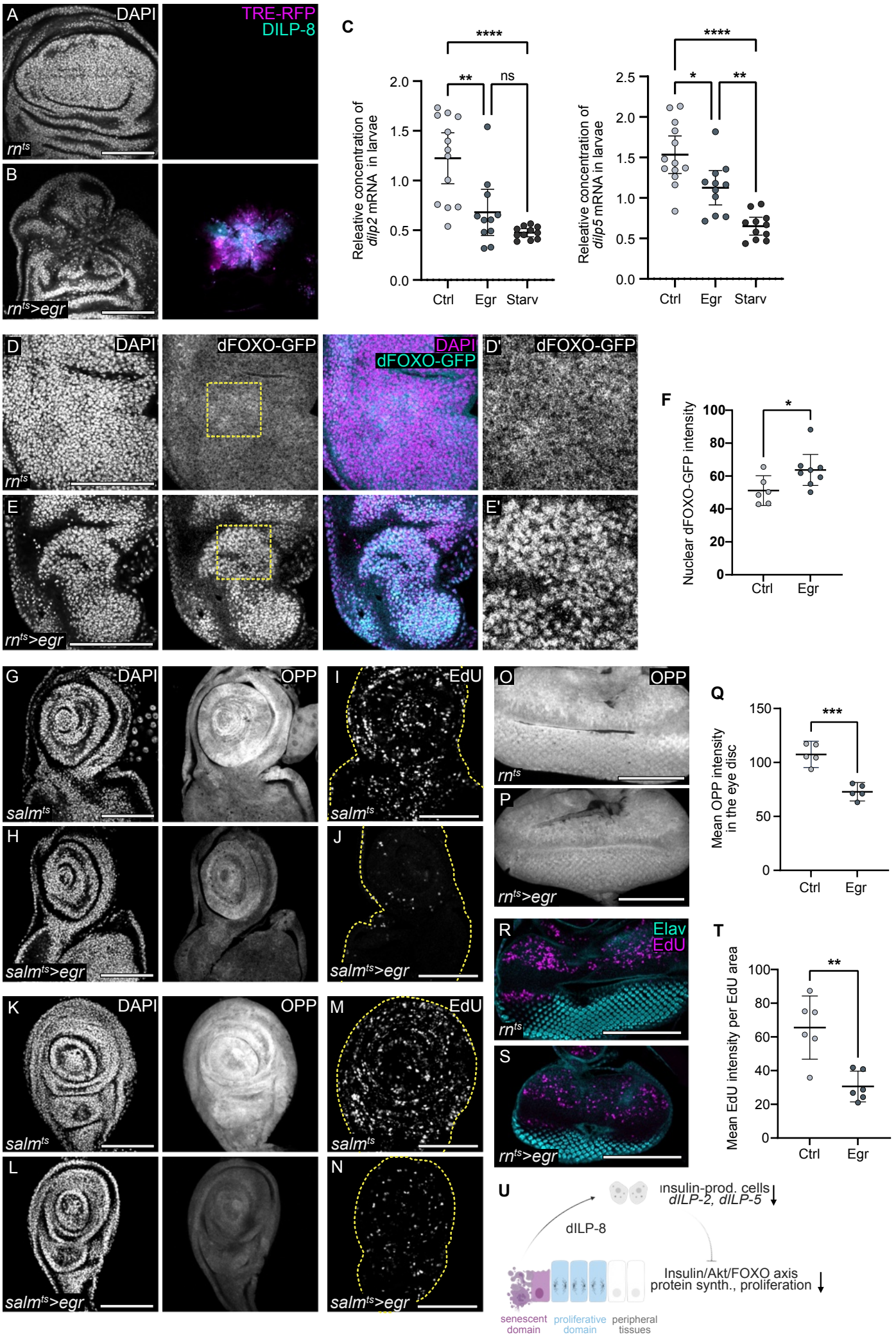
A
DAPI
TRE-RFP
DILP-8
rn^ts
B
rn^ts>egr
C
****
**
ns
Releative concentration of dilp2 mRNA in larvae
2.0
1.5
1.0
0.5
0.0
Ctrl
Egr
Starv
****
*
**
Releative concentration of dilp5 mRNA in larvae
2.5
2.0
1.5
1.0
0.5
0.0
Ctrl
Egr
Starv
D
DAPI
dFOXO-GFP
rn^ts
E
rn^ts>egr
DAPI
dFOXO-GFP
D'
dFOXO-GFP
E'
F
*
Nuclear dFOXO-GFP intensity
100
80
60
40
20
0
Ctrl
Egr
G
DAPI
salm^ts
H
salm^ts>egr
OPP
I
EdU
salm^ts
J
salm^ts>egr
K
DAPI
salm^ts
L
salm^ts>egr
OPP
M
EdU
salm^ts
N
salm^ts>egr
O
OPP
rn^ts
P
rn^ts>egr
Q
***
Mean OPP intensity in the eye disc
150
100
50
0
Ctrl
Egr
R
Elav
EdU
rn^ts
S
rn^ts>egr
T
**
Mean EdU intensity per EdU area
100
80
60
40
20
0
Ctrl
Egr
U
insulin-prod. cells
dILP-2, dILP-5
dILP-8
Insulin/Akt/FOXO axis
protein synth., proliferation
senescent domain
proliferative domain
peripheral tissues

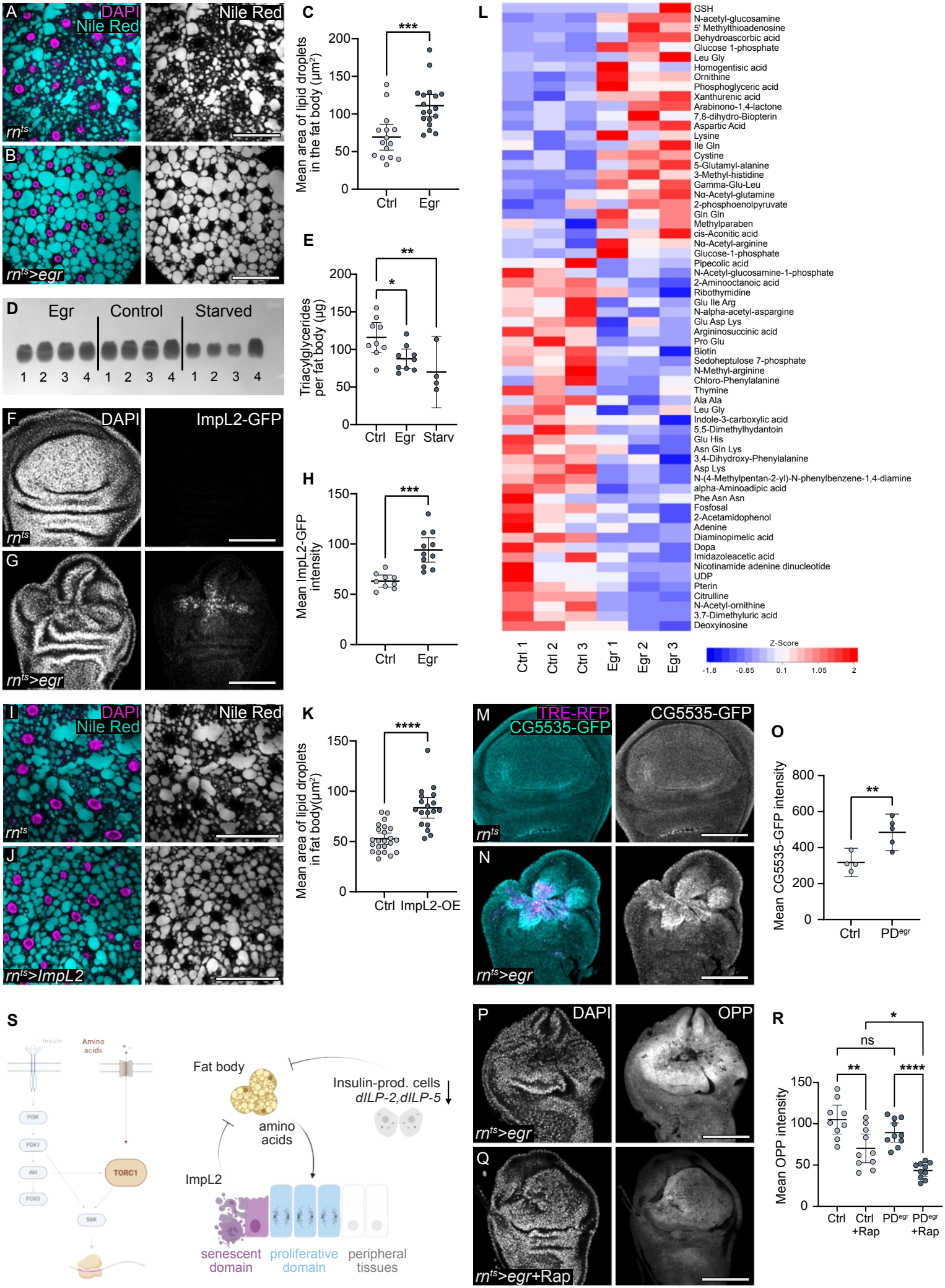
A
DAPI
Nile Red
Nile Red
rnts
B
rnts>egr
C
Mean area of lipid droplets in the fat body (µm²)
***
Ctrl
Egr
D
Egr
Control
Starved
1 2 3 4 1 2 3 4 1 2 3 4
E
Triacylglycerides per fat body (µg)
**
*
Ctrl
Egr
Starv
F
DAPI
ImpL2-GFP
rnts
G
rnts>egr
H
Mean ImpL2-GFP intensity
***
Ctrl
Egr
L
GSH
N-acetyl-glucosamine
5' Methylthioadenosine
Dehydroascorbic acid
Glucose 1-phosphate
Leu Gly
Homogentisic acid
Ornithine
Phosphoglyceric acid
Xanthurenic acid
Arabinono-1,4-lactone
7,8-dihydro-Biopterin
Aspartic Acid
Lysine
Ile Gln
Cystine
5-Glutamyl-alanine
3-Methyl-histidine
Gamma-Glu-Leu
Nα-Acetyl-glutamine
2-phosphoenolpyruvate
Gln Gln
Methylparaben
cis-Aconitic acid
Nα-Acetyl-arginine
Glucose-1-phosphate
Pipecolic acid
N-Acetyl-glucosamine-1-phosphate
2-Aminooctanoic acid
Ribothymidine
Glu Ile Arg
N-alpha-acetyl-aspargine
Glu Asp Lys
Argininosuccinic acid
Pro Glu
Biotin
Sedoheptulose 7-phosphate
N-Methyl-arginine
Chloro-Phenylalanine
Thymine
Ala Ala
Leu Gly
Indole-3-carboxylic acid
5,5-Dimethylhydantoin
Glu His
Asn Gln Lys
3,4-Dihydroxy-Phenylalanine
Asp Lys
N-(4-Methylpentan-2-yl)-N-phenylbenzene-1,4-diamine
alpha-Aminoadipic acid
Phe Asn Asn
Fosfosal
2-Acetamidophenol
Adenine
Diaminopimelic acid
Dopa
Imidazoleacetic acid
Nicotinamide adenine dinucleotide
UDP
Pterin
Citrulline
N-Acetyl-ornithine
3,7-Dimethyluric acid
Deoxyinosine
Ctrl 1
Ctrl 2
Ctrl 3
Egr 1
Egr 2
Egr 3
Z-Score
-1.8
-0.85
0.1
1.05
2
I
DAPI
Nile Red
Nile Red
rnts
J
rnts>ImpL2
K
Mean area of lipid droplets in fat body(µm²)
****
Ctrl
ImpL2-OE
M
TRE-RFP
CG5535-GFP
CG5535-GFP
rnts
N
rnts>egr
O
Mean CG5535-GFP intensity
**
Ctrl
PDegr
S
Insulin
Amino acids
PI3K
PDK1
Akt
FOXO
TORC1
S6K
Fat body
Insulin-prod. cells
dILP-2,dILP-5
amino acids
ImpL2
senescent domain
proliferative domain
peripheral tissues
P
DAPI
OPP
rnts>egr
Q
rnts>egr+Rap
R
Mean OPP intensity
*
ns
**
****
Ctrl
Ctrl +Rap
PDegr
PDegr +Rap

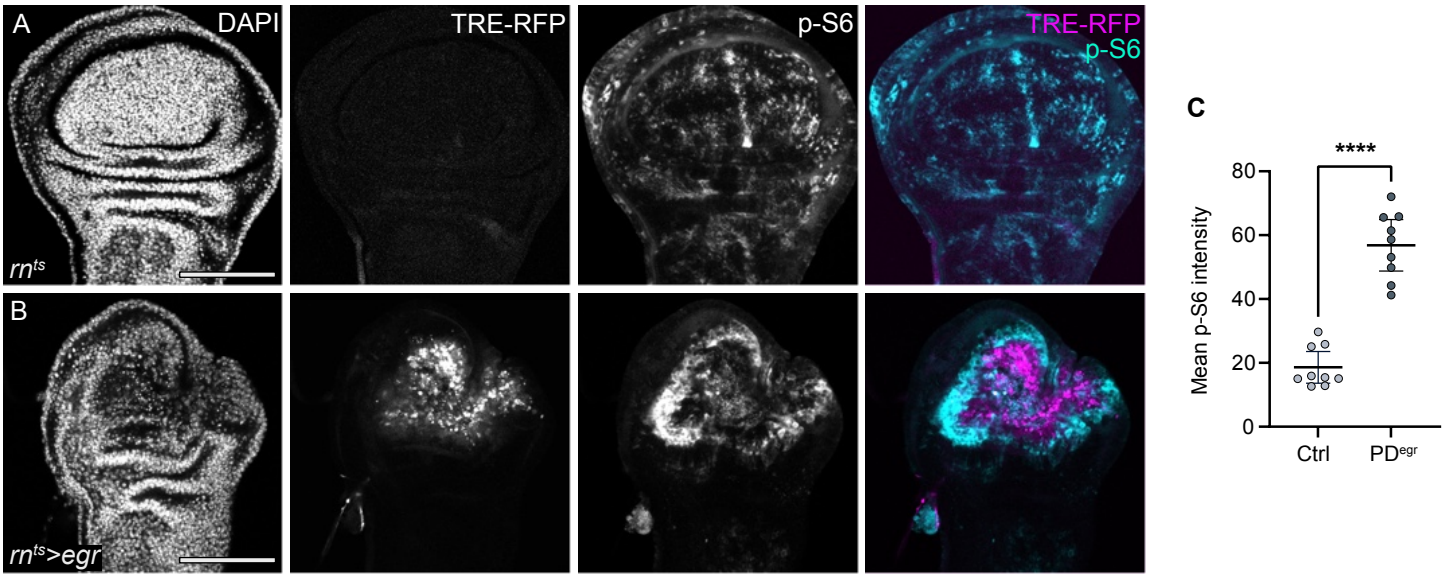
A
DAPI
TRE-RFP
p-S6
TRE-RFP
p-S6
rn^ts
B
rn^ts>egr

C
****
Mean p-S6 intensity
80
60
40
20
0
Ctrl
PD^egr

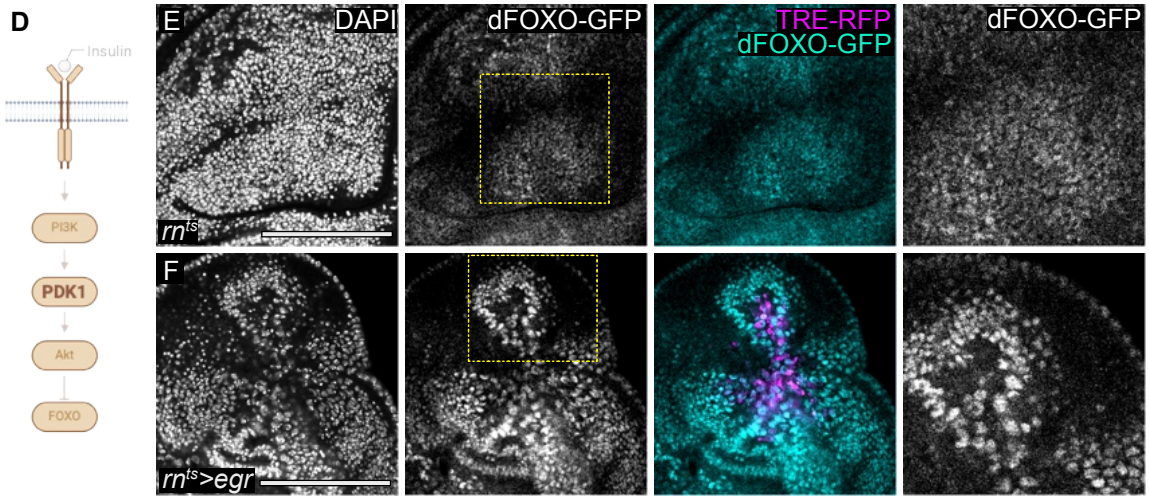
D
Insulin
PI3K
PDK1
Akt
FOXO
E
DAPI
dFOXO-GFP
TRE-RFP
dFOXO-GFP
dFOXO-GFP
rn^ts
F
rn^ts>egr

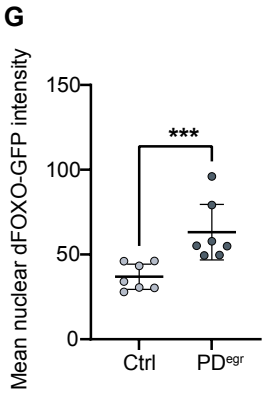
G
***
Mean nuclear dFOXO-GFP intensity
150
100
50
0
Ctrl
PD^egr

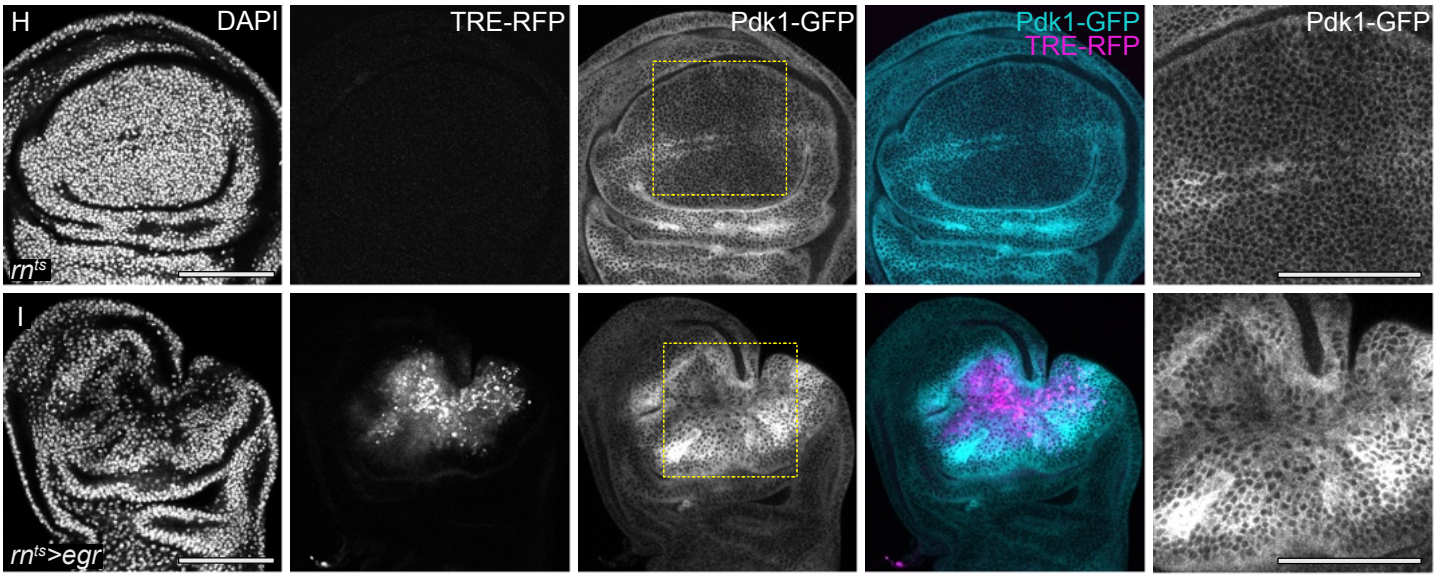
H
DAPI
TRE-RFP
Pdk1-GFP
Pdk1-GFP
TRE-RFP
Pdk1-GFP
rn^ts
I
rn^ts>egr

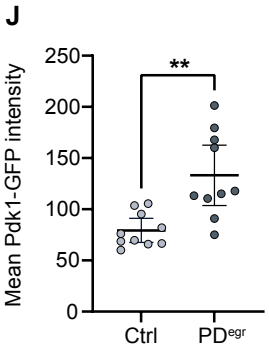
J
**
Mean Pdk1-GFP intensity
250
200
150
100
50
0
Ctrl
PD^egr

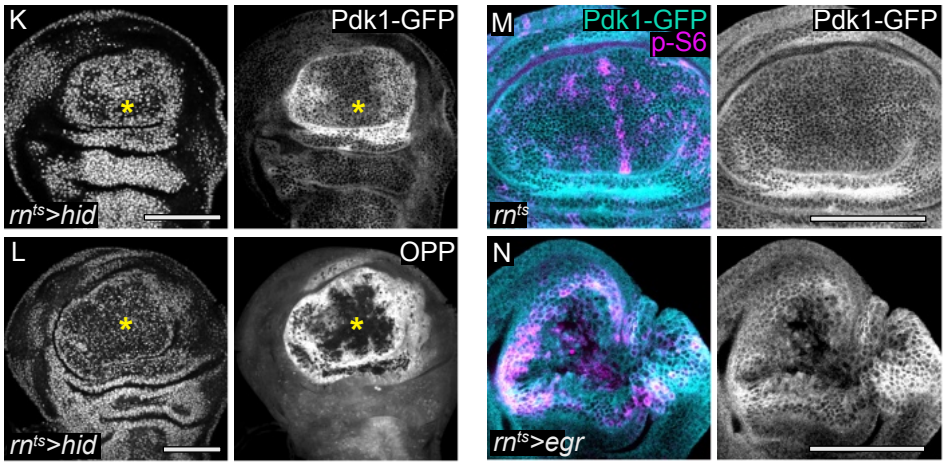
K
Pdk1-GFP
rn^ts>hid
L
OPP
rn^ts>hid
M
Pdk1-GFP
p-S6
Pdk1-GFP
rn^ts
N
rn^ts>egr

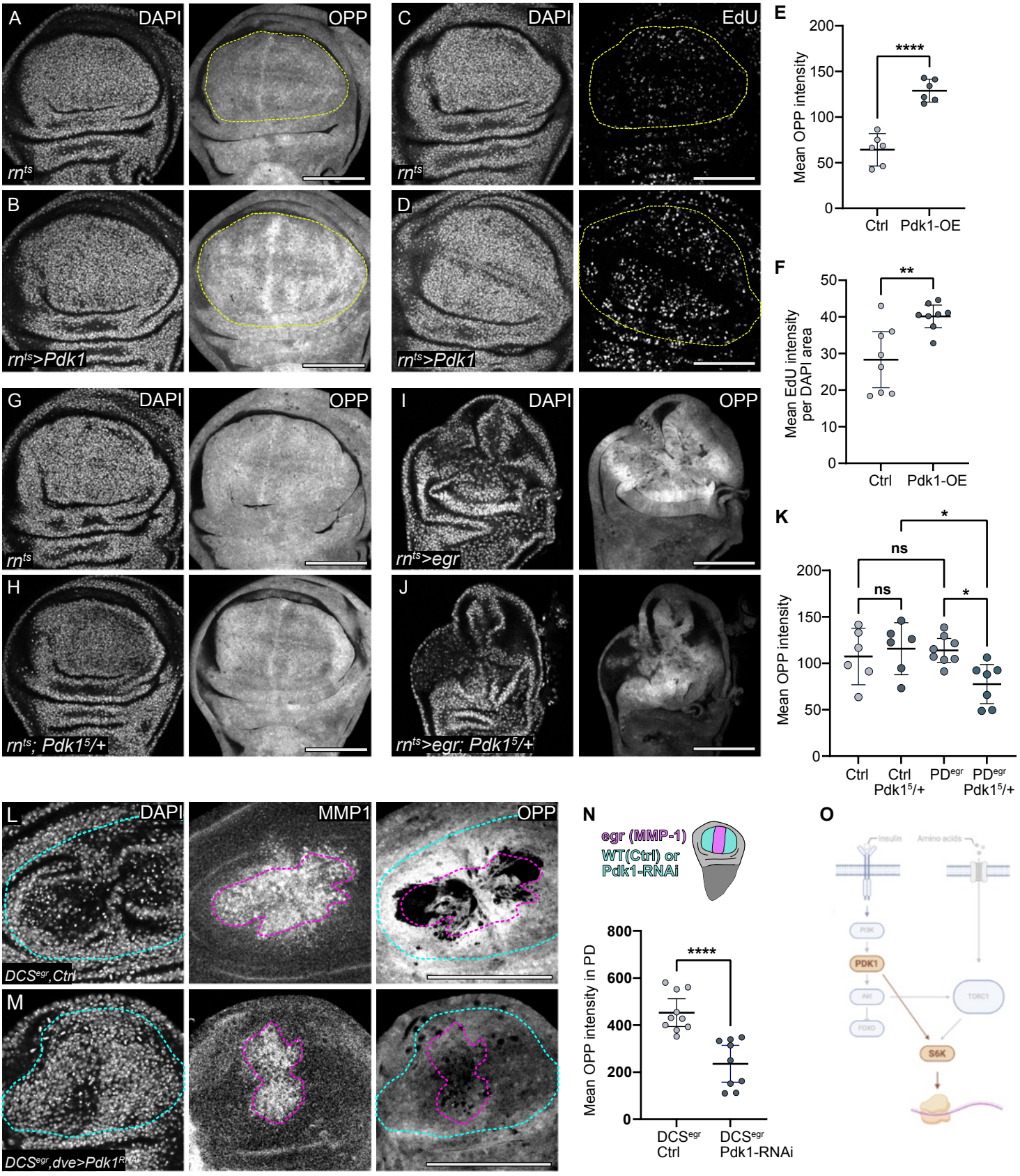
A
DAPI
OPP
rn^ts
B
rn^ts>Pdk1
C
DAPI
EdU
rn^ts
D
rn^ts>Pdk1
E
Mean OPP intensity
****
Ctrl
Pdk1-OE
F
Mean EdU intensity per DAPI area
**
Ctrl
Pdk1-OE
G
DAPI
OPP
rn^ts
H
rn^ts; Pdk1^5/+
I
DAPI
OPP
rn^ts>egr
J
rn^ts>egr; Pdk1^5/+
K
Mean OPP intensity
ns
ns
*
*
Ctrl
Ctrl Pdk1^5/+
PD^egr
PD^egr Pdk1^5/+
L
DAPI
MMP1
OPP
DCS^egr,Ctrl
M
DCS^egr,dve>Pdk1^RNAi
N
egr (MMP-1)
WT(Ctrl) or Pdk1-RNAi
Mean OPP intensity in PD
****
DCS^egr Ctrl
DCS^egr Pdk1-RNAi
O
Insulin
Amino acids
PI3K
PDK1
Akt
FOXO
TORC1
S6K

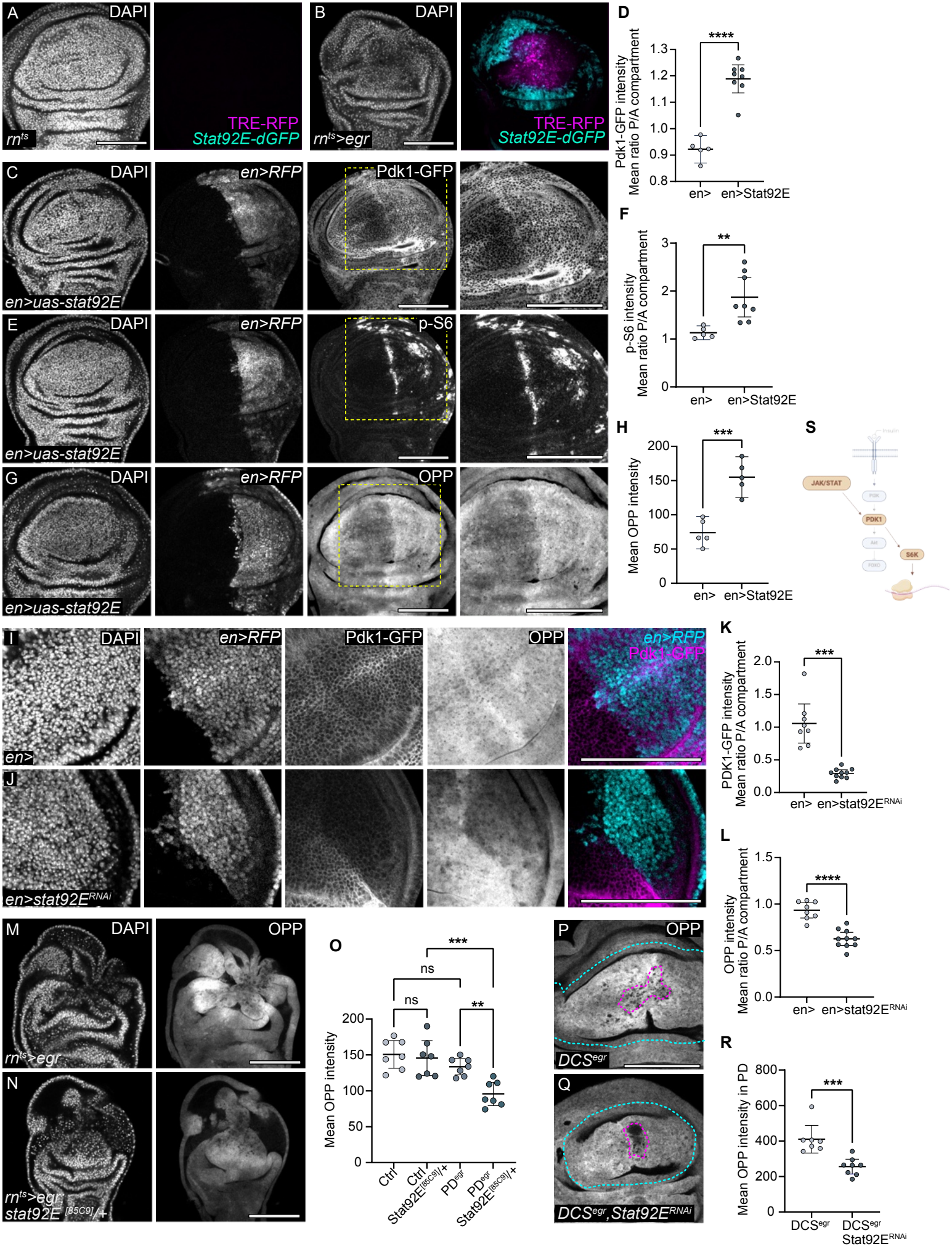
A
DAPI
rn^ts
TRE-RFP
Stat92E-dGFP
B
DAPI
rn^ts>egr
TRE-RFP
Stat92E-dGFP
D
Pdk1-GFP intensity
Mean ratio P/A compartment
****
en>
en>Stat92E
C
DAPI
en>RFP
Pdk1-GFP
en>uas-stat92E
E
DAPI
en>RFP
p-S6
en>uas-stat92E
F
p-S6 intensity
Mean ratio P/A compartment
**
en>
en>Stat92E
G
DAPI
en>RFP
OPP
en>uas-stat92E
H
Mean OPP intensity
***
en>
en>Stat92E
S
JAK/STAT
PDK1
S6K
I
DAPI
en>RFP
Pdk1-GFP
OPP
en>RFP
Pdk1-GFP
en>
J
en>stat92E^RNAi
K
PDK1-GFP intensity
Mean ratio P/A compartment
***
en>
en>stat92E^RNAi
L
OPP intensity
Mean ratio P/A compartment
****
en>
en>stat92E^RNAi
M
DAPI
OPP
rn^ts>egr
N
rn^ts>egr;
stat92E [85C9]/+
O
Mean OPP intensity
***
ns
ns
**
Ctrl
Ctrl Stat92E[85C9]/+
PD^egr
PD^egr Stat92E[85C9]/+
P
OPP
DCS^egr
Q
DCS^egr,Stat92E^RNAi
R
Mean OPP intensity in PD
***
DCS^egr
DCS^egr Stat92E^RNAi

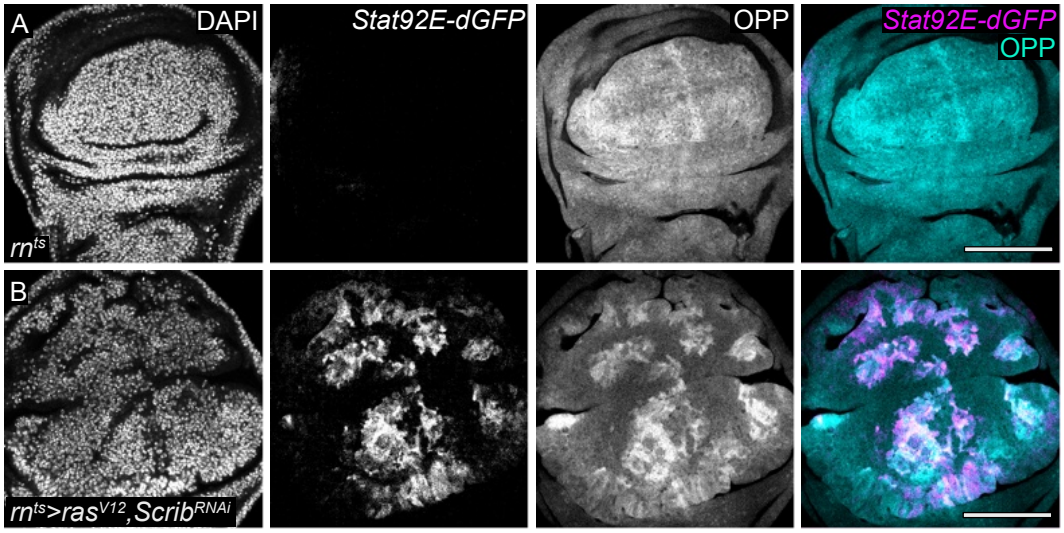
A
DAPI
Stat92E-dGFP
OPP
Stat92E-dGFP
OPP
rn^ts
B
rn^ts>ras^V12,Scrib^RNAi

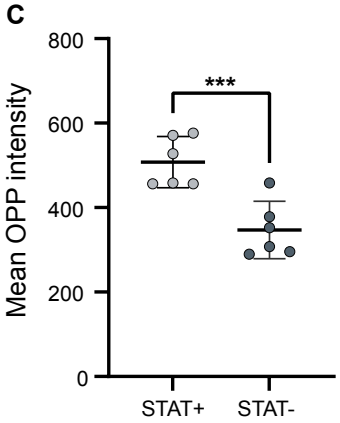
C
Mean OPP intensity
800
600
400
200
0
***
STAT+
STAT-

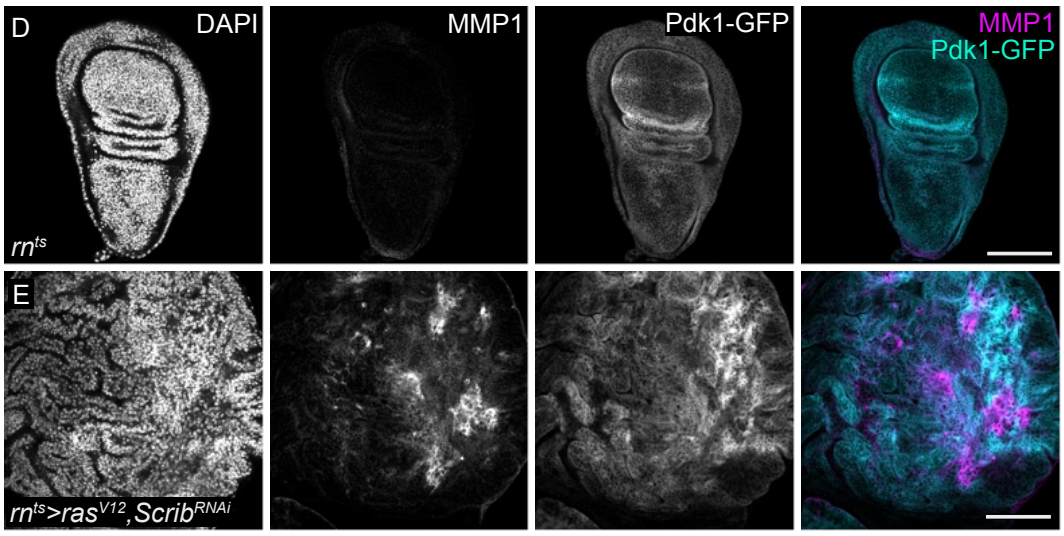
D
DAPI
MMP1
Pdk1-GFP
MMP1
Pdk1-GFP
rn^ts
E
rn^ts>ras^V12,Scrib^RNAi

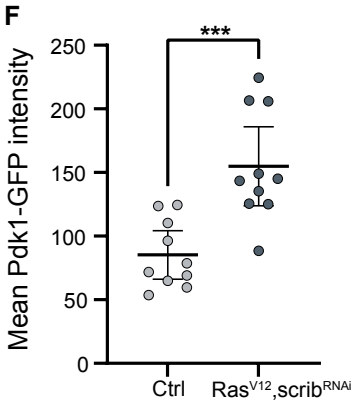
F
Mean Pdk1-GFP intensity
250
200
150
100
50
0
***
Ctrl
Ras^V12,scrib^RNAi

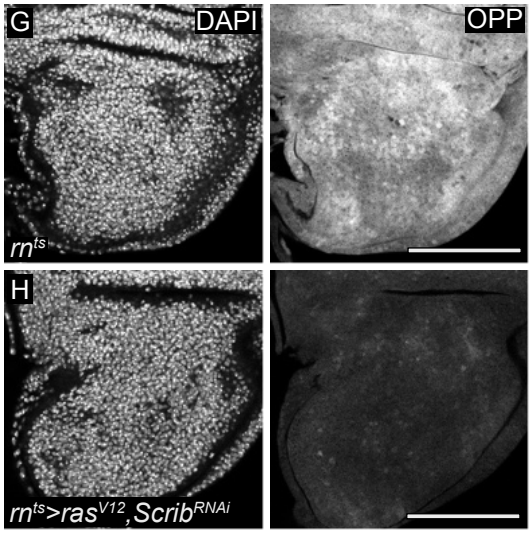
G
DAPI
OPP
rn^ts
H
rn^ts>ras^V12,Scrib^RNAi

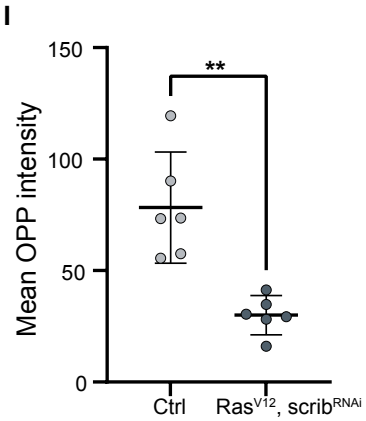
I
Mean OPP intensity
150
100
50
0
**
Ctrl
Ras^V12, scrib^RNAi

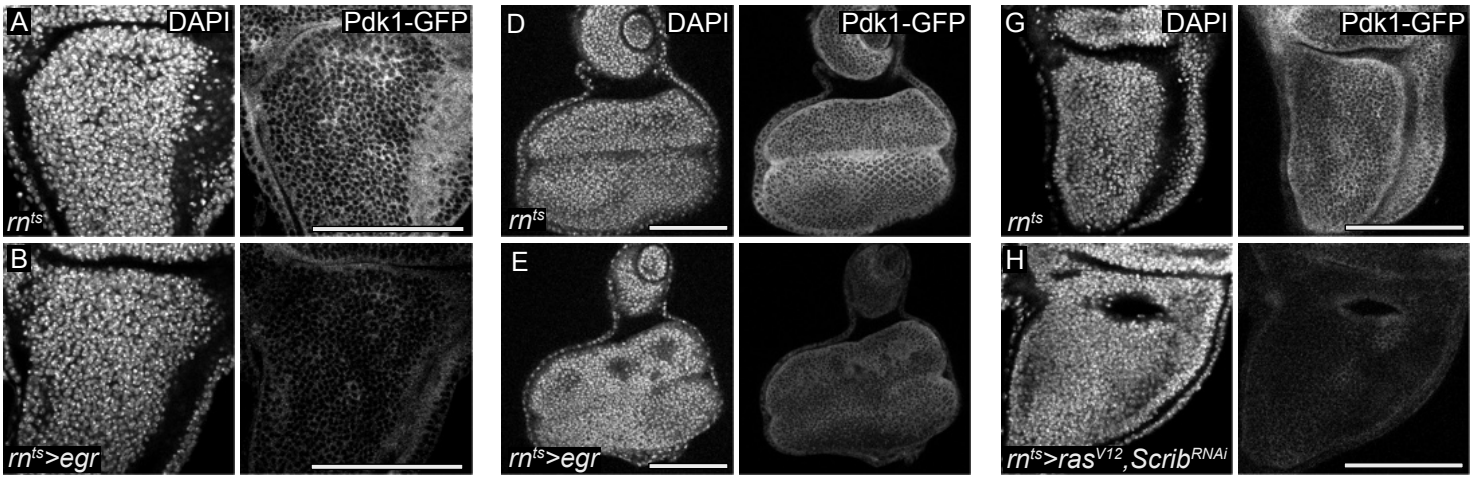
A
DAPI
Pdk1-GFP
rn^ts
B
rn^ts>egr
D
DAPI
Pdk1-GFP
rn^ts
E
rn^ts>egr
G
DAPI
Pdk1-GFP
rn^ts
H
rn^ts>ras^V12,Scrib^RNAi

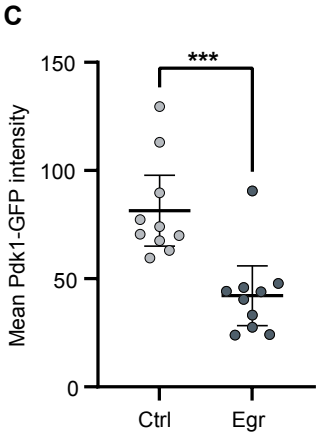
C
Mean Pdk1-GFP intensity
150
100
50
0
***
Ctrl
Egr

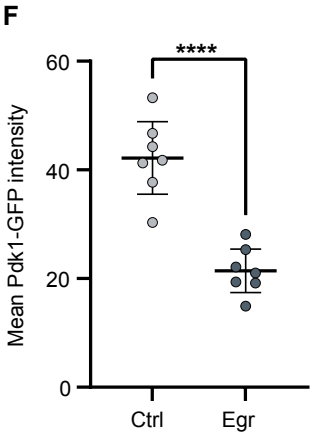
F
Mean Pdk1-GFP intensity
60
40
20
0
****
Ctrl
Egr

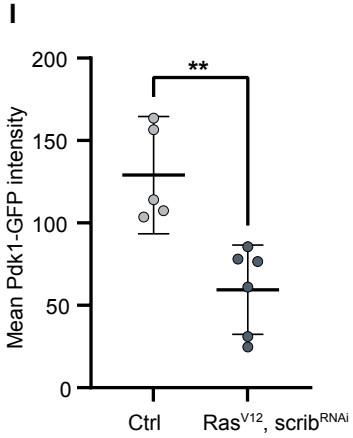
I
Mean Pdk1-GFP intensity
200
150
100
50
0
**
Ctrl
Ras^V12, scrib^RNAi

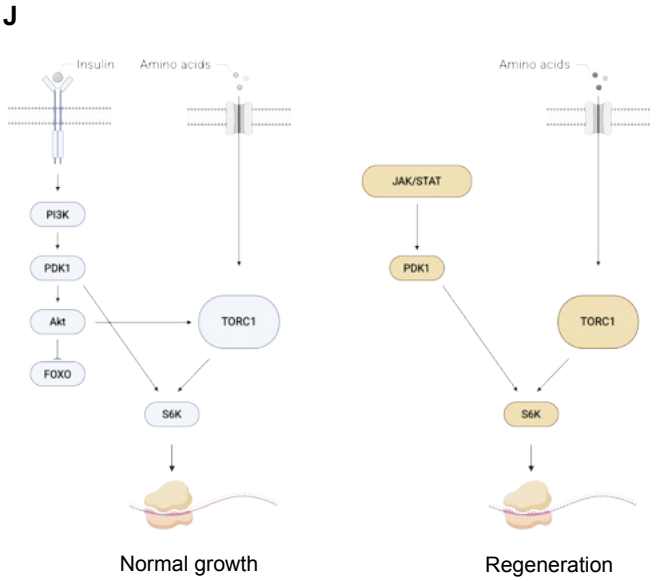
J
Insulin
Amino acids
PI3K
PDK1
Akt
FOXO
TORC1
S6K
Normal growth
Amino acids
JAK/STAT
PDK1
TORC1
S6K
Regeneration

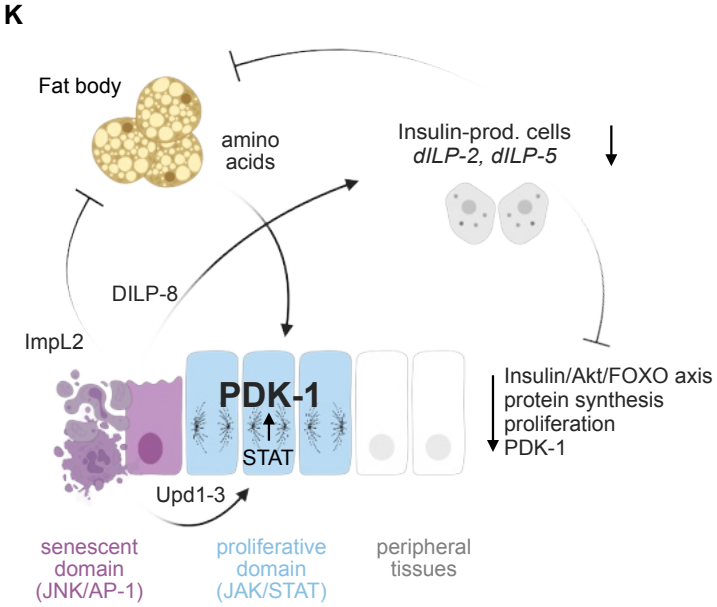
K
Fat body
amino acids
Insulin-prod. cells
dILP-2, dILP-5
DILP-8
ImpL2
PDK-1
STAT
Upd1-3
Insulin/Akt/FOXO axis
protein synthesis
proliferation
PDK-1
senescent domain (JNK/AP-1)
proliferative domain (JAK/STAT)
peripheral tissues

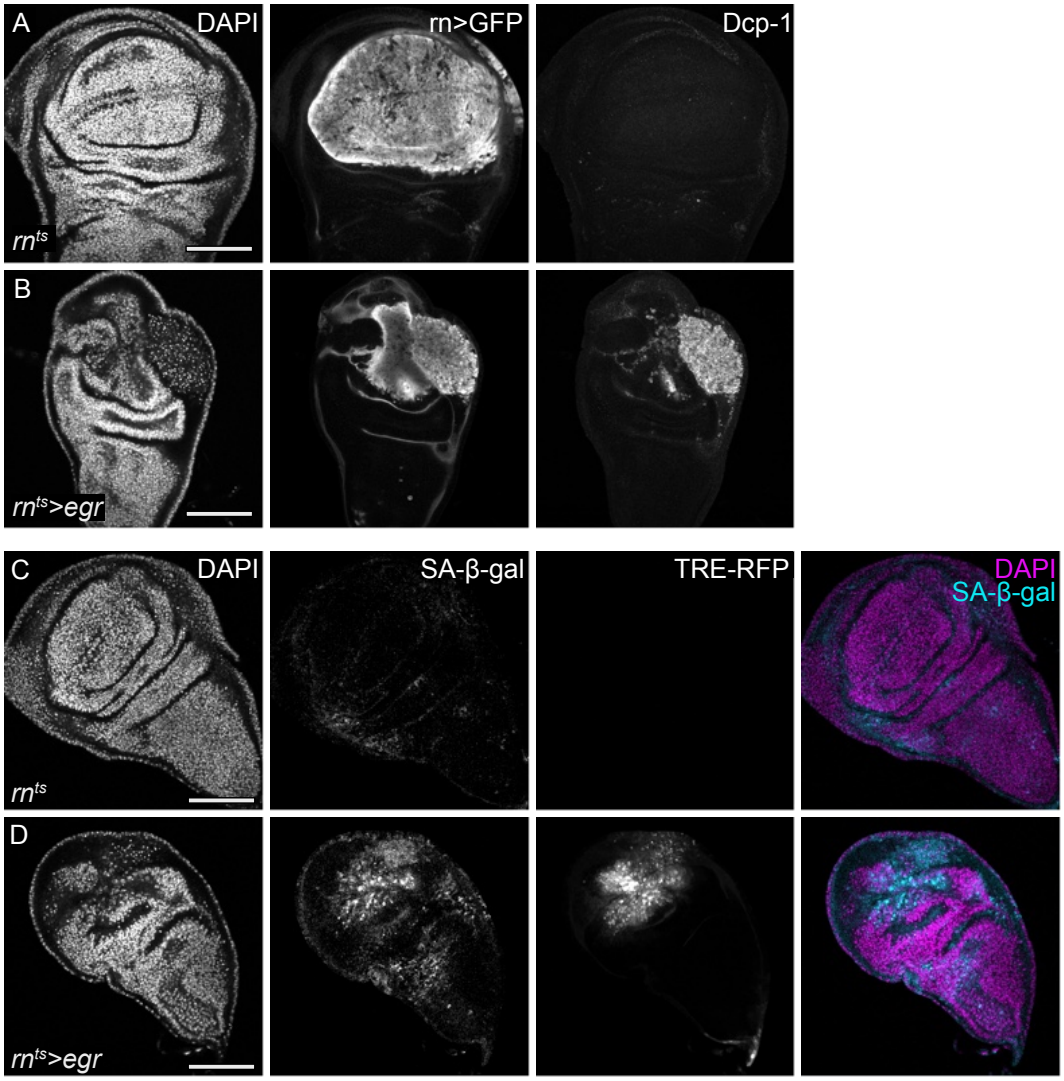
A
DAPI
rn>GFP
Dcp-1
rnts
B
rnts>egr
C
DAPI
SA-β-gal
TRE-RFP
DAPI
SA-β-gal
rnts
D
rnts>egr

S1

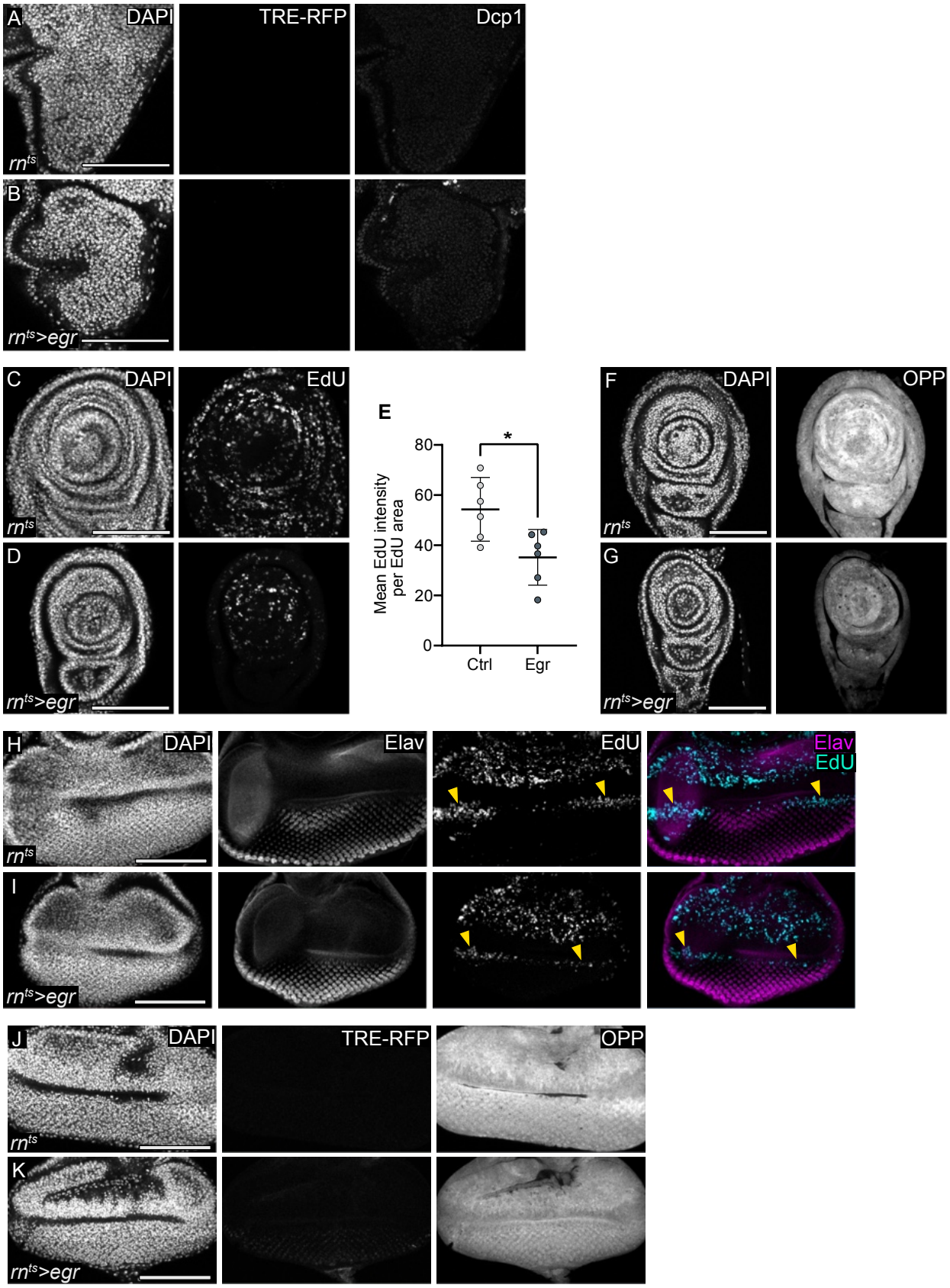
A
DAPI
TRE-RFP
Dcp1
rnts
B
rnts>egr
C
DAPI
EdU
rnts
D
rnts>egr
E
Mean EdU intensity per EdU area
80
60
40
20
0
*
Ctrl
Egr
F
DAPI
OPP
rnts
G
rnts>egr
H
DAPI
Elav
EdU
Elav
EdU
rnts
I
rnts>egr
J
DAPI
TRE-RFP
OPP
rnts
K
rnts>egr

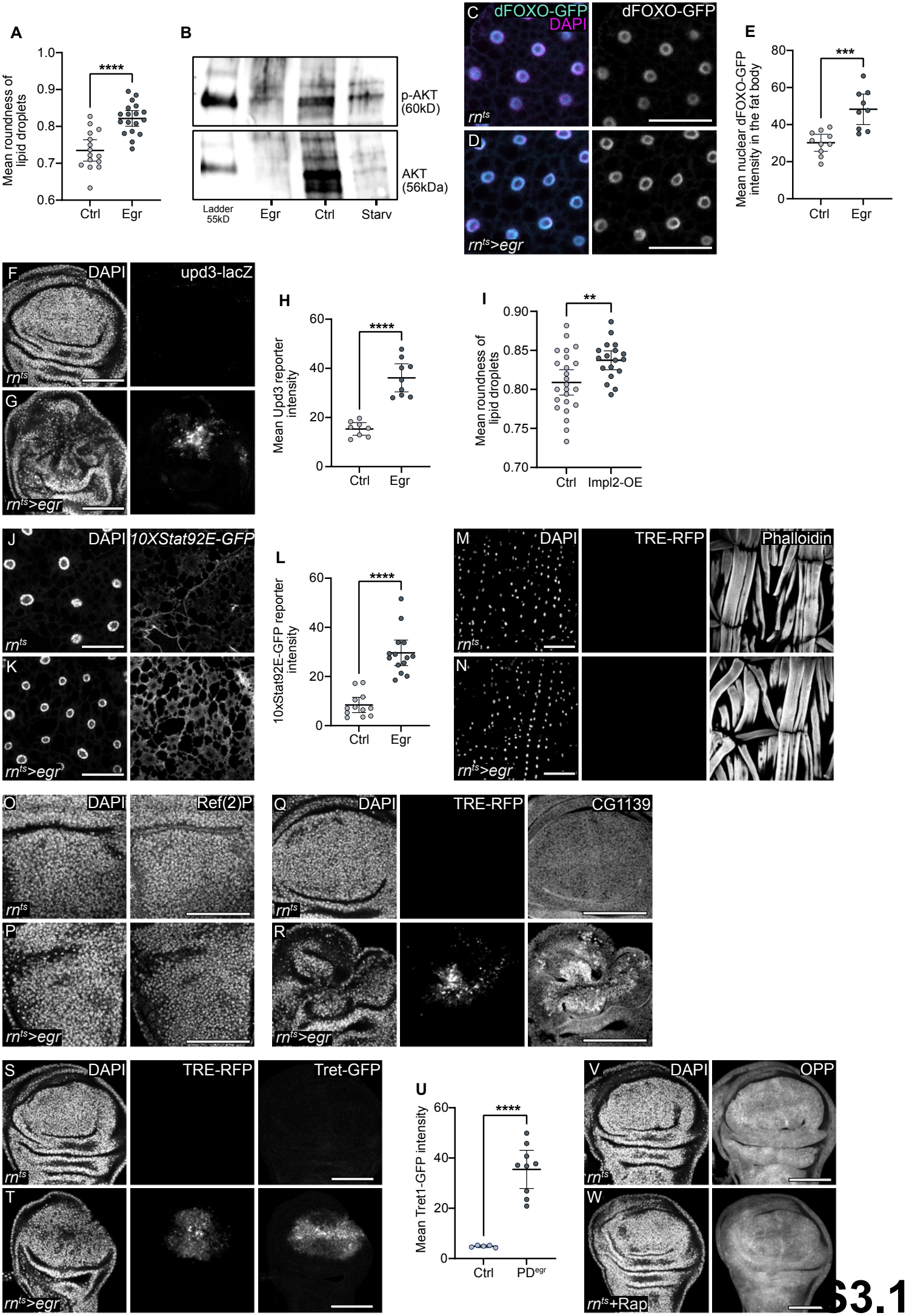
A
Mean roundness of lipid droplets
1.0
0.9
0.8
0.7
0.6
****
Ctrl
Egr
B
p-AKT (60kD)
AKT (56kDa)
Ladder 55kD
Egr
Ctrl
Starv
C
dFOXO-GFP
DAPI
dFOXO-GFP
rnts
D
rnts>egr
E
Mean nuclear dFOXO-GFP intensity in the fat body
80
60
40
20
0
***
Ctrl
Egr
F
DAPI
upd3-lacZ
rnts
G
rnts>egr
H
Mean Upd3 reporter intensity
60
40
20
0
****
Ctrl
Egr
I
Mean roundness of lipid droplets
0.90
0.85
0.80
0.75
0.70
**
Ctrl
Impl2-OE
J
DAPI
10XStat92E-GFP
rnts
K
rnts>egr
L
10xStat92E-GFP reporter intensity
60
40
20
0
****
Ctrl
Egr
M
DAPI
TRE-RFP
Phalloidin
rnts
N
rnts>egr
O
DAPI
Ref(2)P
rnts
P
rnts>egr
Q
DAPI
TRE-RFP
CG1139
rnts
R
rnts>egr
S
DAPI
TRE-RFP
Tret-GFP
rnts
T
rnts>egr
U
Mean Tret1-GFP intensity
60
40
20
0
****
Ctrl
PDegr
V
DAPI
OPP
rnts
W
rnts+Rap

S3.1

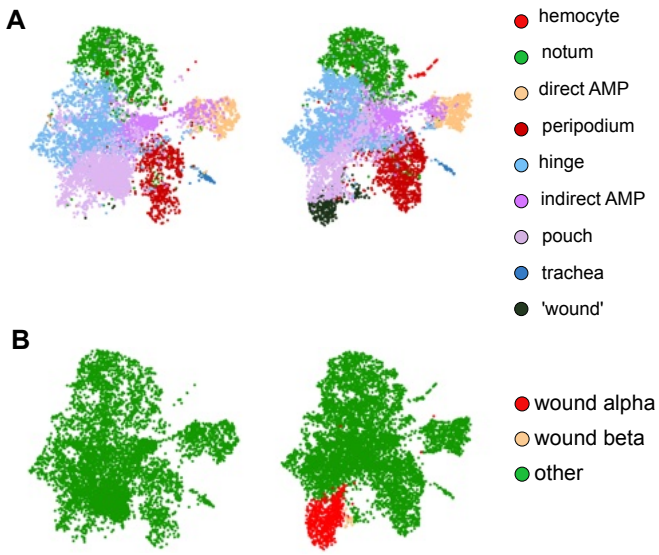

Floc'hlay et.al, *eLife*, 2023

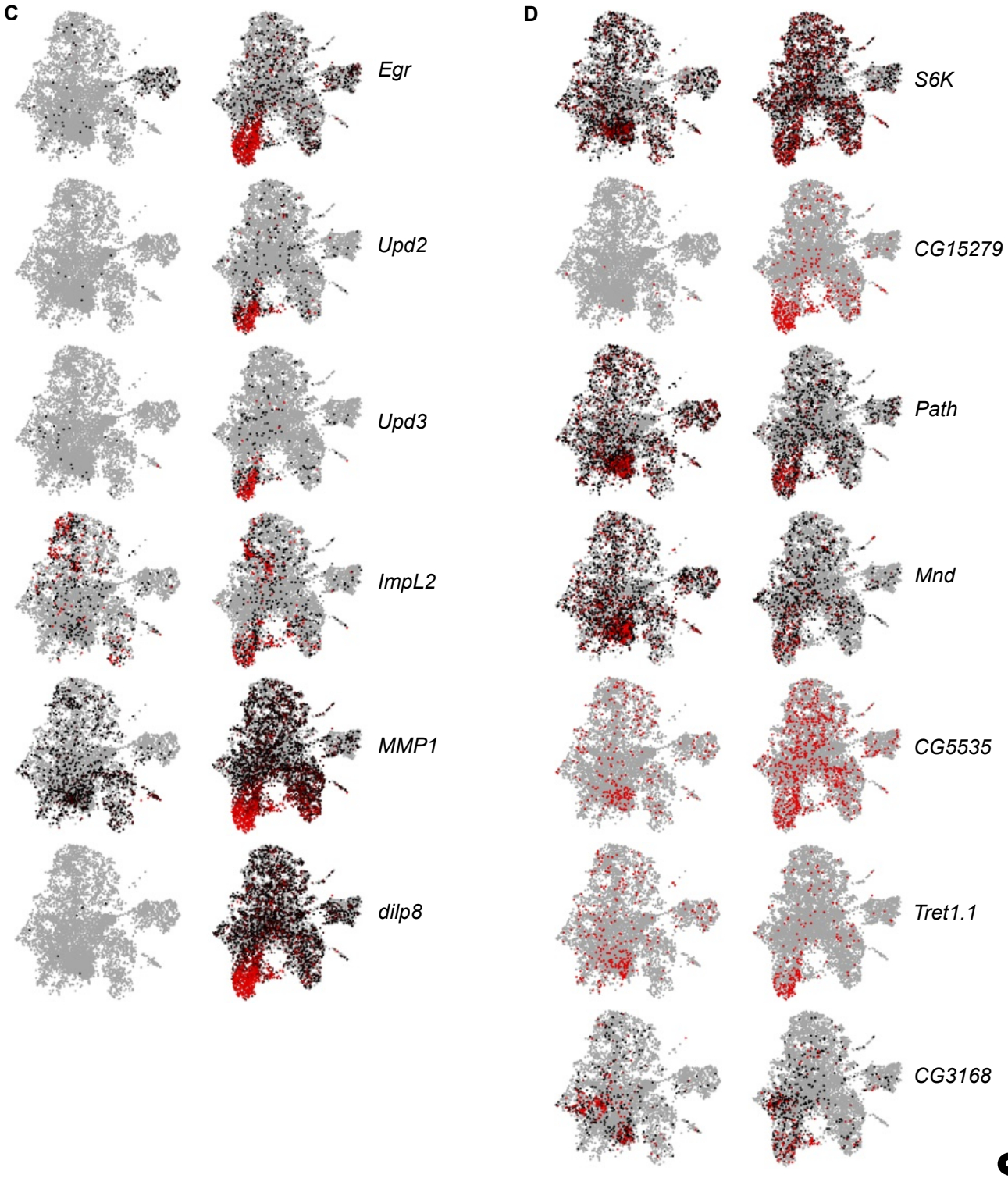

S3.2

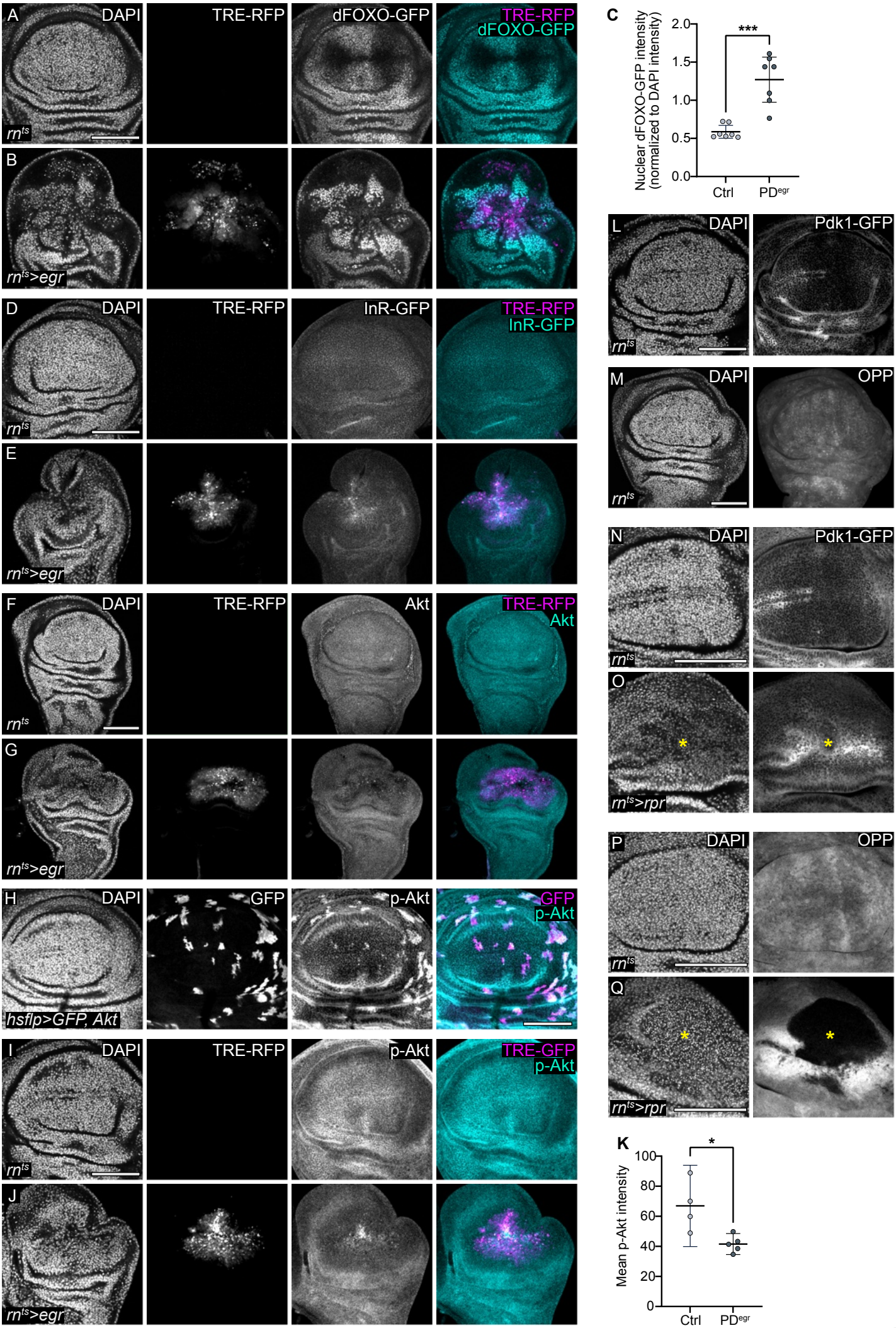
A
DAPI
TRE-RFP
dFOXO-GFP
TRE-RFP
dFOXO-GFP
rn^ts
B
rn^ts>egr
C
Nuclear dFOXO-GFP intensity (normalized to DAPI intensity)
2.0
1.5
1.0
0.5
0.0
***
Ctrl
PD^egr
D
DAPI
TRE-RFP
InR-GFP
TRE-RFP
InR-GFP
rn^ts
E
rn^ts>egr
F
DAPI
TRE-RFP
Akt
TRE-RFP
Akt
rn^ts
G
rn^ts>egr
H
DAPI
GFP
p-Akt
GFP
p-Akt
hsflp>GFP, Akt
I
DAPI
TRE-RFP
p-Akt
TRE-GFP
p-Akt
rn^ts
J
rn^ts>egr
L
DAPI
Pdk1-GFP
rn^ts
M
DAPI
OPP
rn^ts
N
DAPI
Pdk1-GFP
rn^ts
O
rn^ts>rpr
P
DAPI
OPP
rn^ts
Q
rn^ts>rpr
K
Mean p-Akt intensity
100
80
60
40
20
0
*
Ctrl
PD^egr

S4

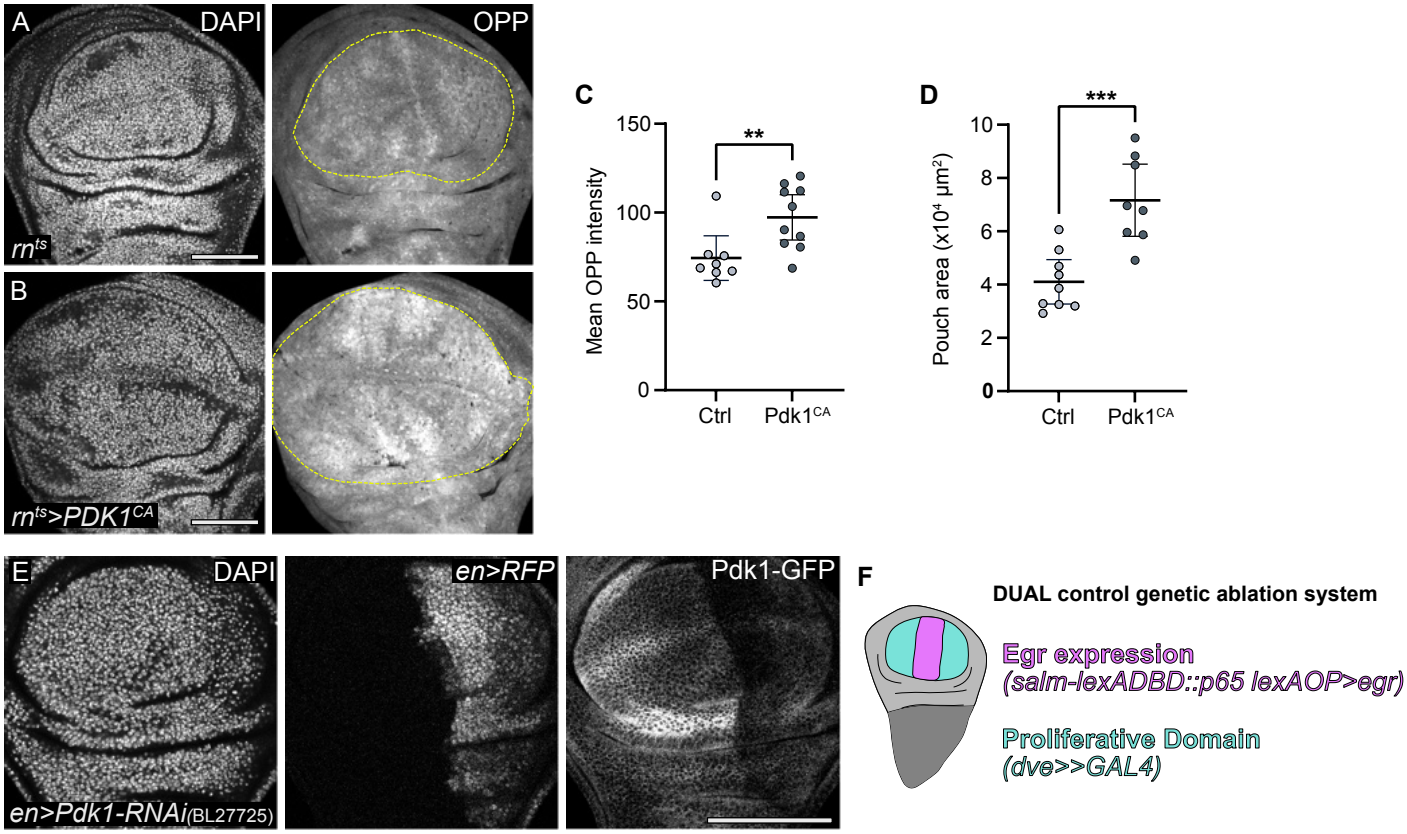
A
DAPI
OPP
rn^ts
B
rn^ts>PDK1^CA
C
Mean OPP intensity
150
100
50
0
**
Ctrl
Pdk1^CA
D
Pouch area (x10^4 µm^2)
10
8
6
4
2
0
***
Ctrl
Pdk1^CA
E
DAPI
en>RFP
Pdk1-GFP
en>Pdk1-RNAi(BL27725)
F
DUAL control genetic ablation system
Egr expression
(salm-lexADBD::p65 lexAOP>egr)
Proliferative Domain
(dve>>GAL4)

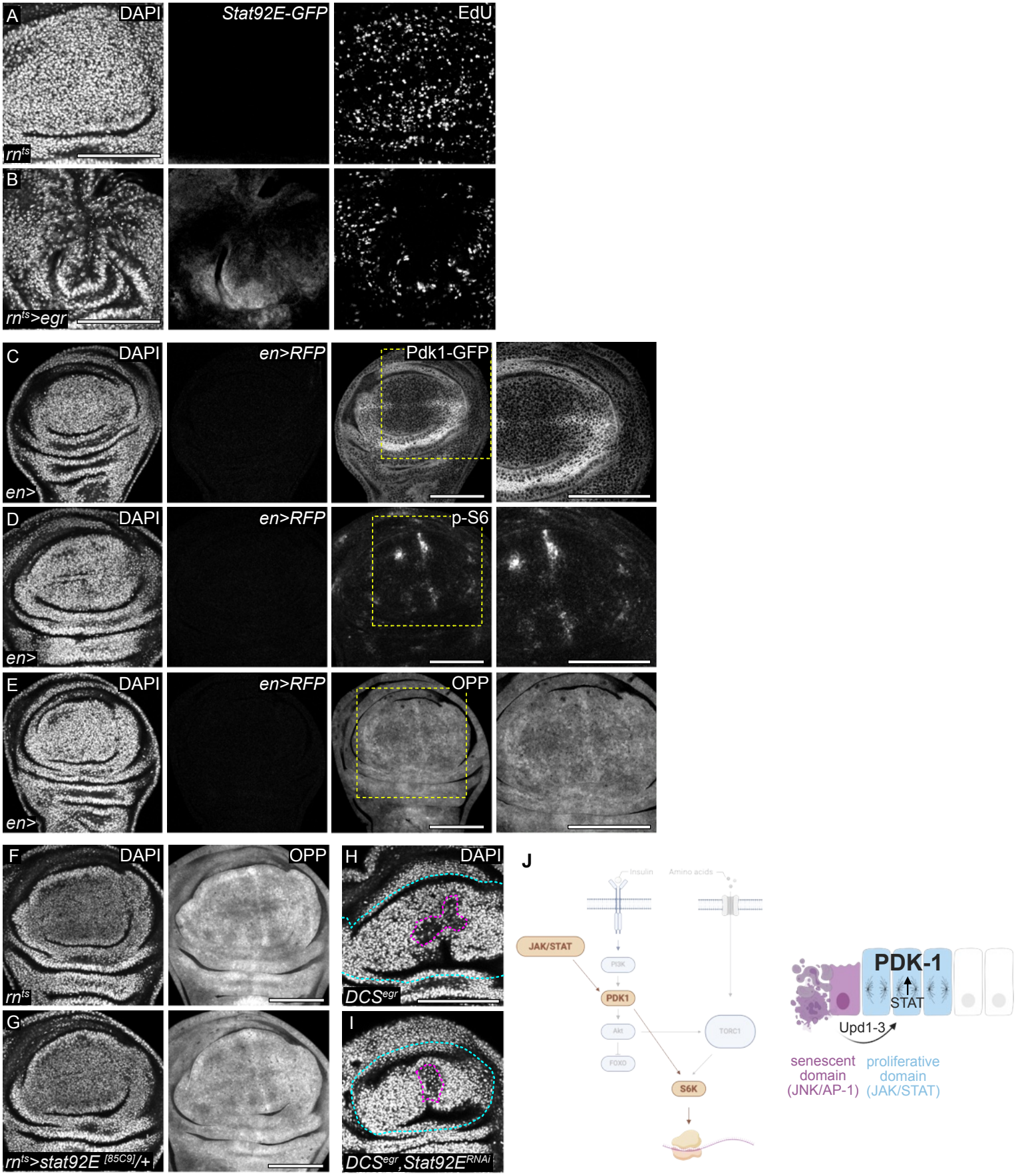
A
DAPI
Stat92E-GFP
EdU
rnts
B
rnts>egr
C
DAPI
en>RFP
Pdk1-GFP
en>
D
DAPI
en>RFP
p-S6
en>
E
DAPI
en>RFP
OPP
en>
F
DAPI
OPP
rnts
G
rnts>stat92E [85C9]/+
H
DAPI
DCSegr
I
DCSegr,Stat92ERNAi
J
Insulin
Amino acids
JAK/STAT
PI3K
PDK1
Akt
FOXO
TORC1
S6K
PDK-1
STAT
Upd1-3
senescent domain (JNK/AP-1)
proliferative domain (JAK/STAT)

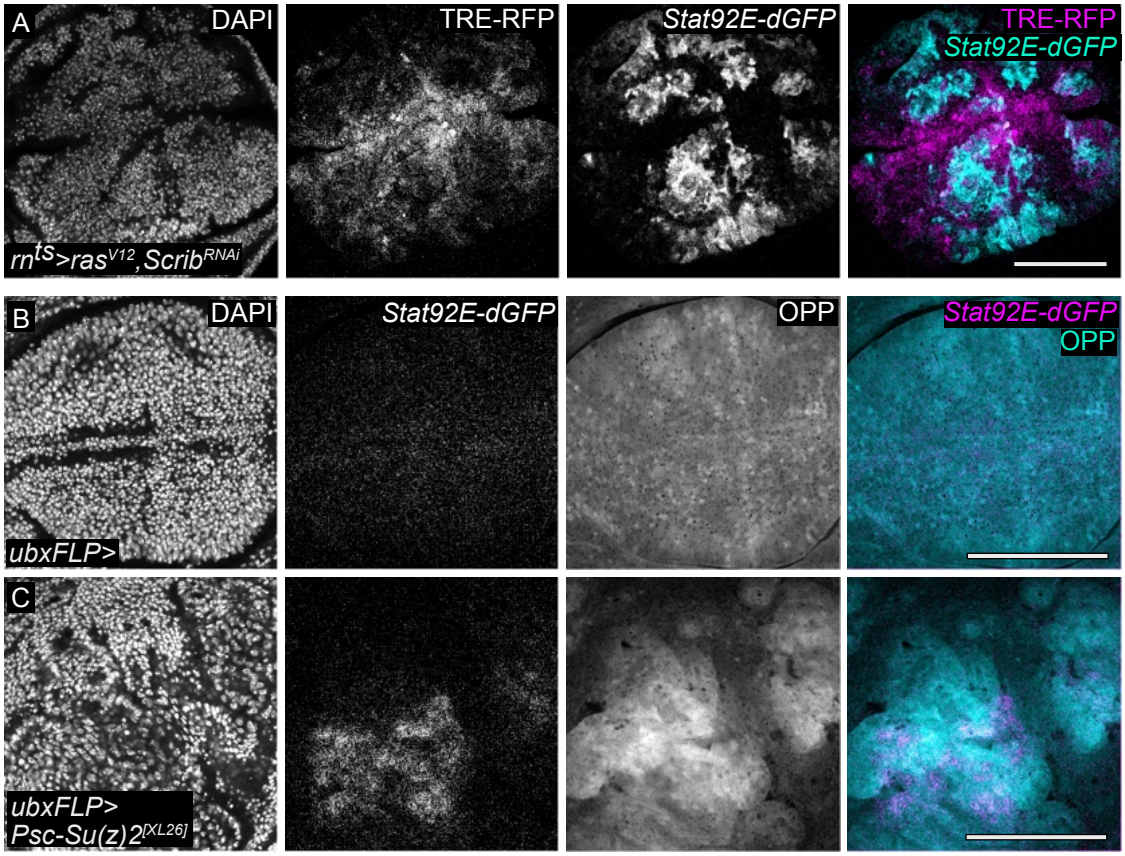
A
DAPI
TRE-RFP
Stat92E-dGFP
TRE-RFP
Stat92E-dGFP
rn^ts>ras^V12,Scrib^RNAi
B
DAPI
Stat92E-dGFP
OPP
Stat92E-dGFP
OPP
ubxFLP>
C
ubxFLP>
Psc-Su(z)2^[XL26]

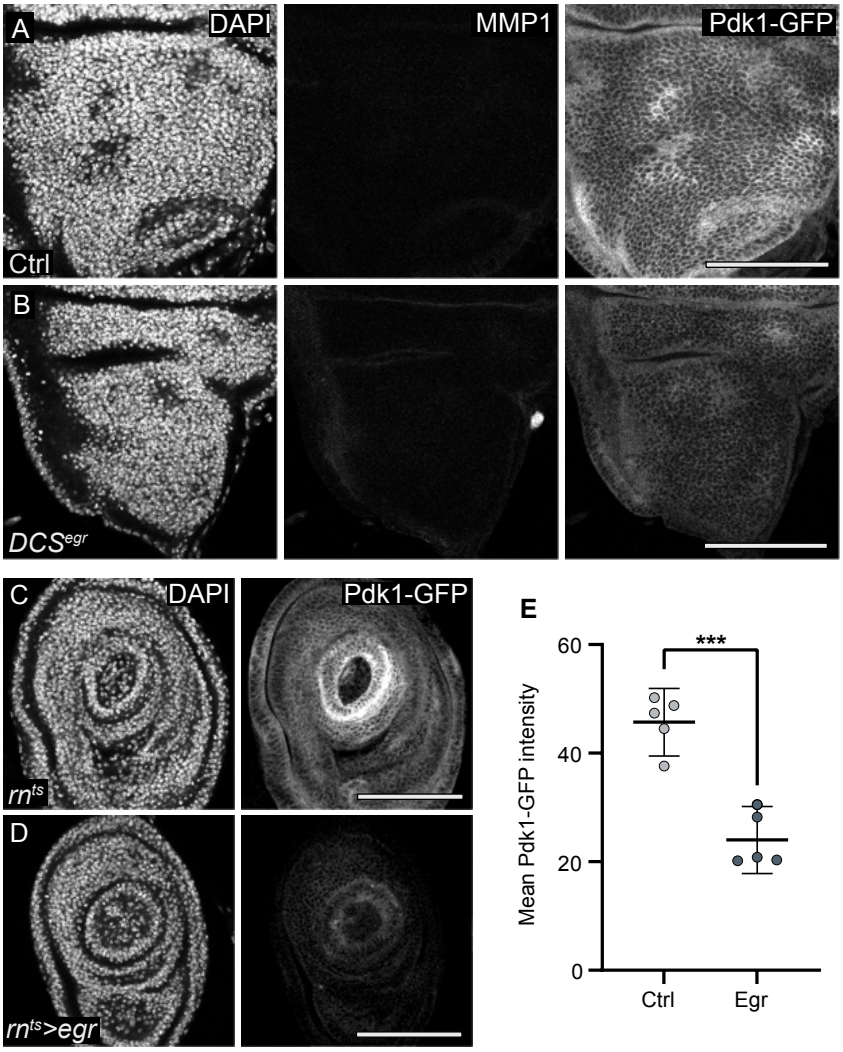
A
DAPI
MMP1
Pdk1-GFP
Ctrl
B
DCS^egr
C
DAPI
Pdk1-GFP
rn^ts
D
rn^ts>egr
E
Mean Pdk1-GFP intensity
60
40
20
0
***
Ctrl
Egr

Table S1 *Drosophila* strains

Genotype	Source
Dilp8-GFP	BDSC: 33079
ImpL2-GFP	BDSC: 59778
UAS-ImpL2-3xHA	Fly-ORF F001712
Upd3.1-3 LacZ	Ishwar Hariharan lab
dFOXO-GFP	BDSC: 59766 (FigS3.1C, D ; Fig S4 A, B)
dFOXO-GFP	BDSC 38644 (Fig 2D, E ; Fig4E, F)
salm-GAL4 / CyO,ubi-GFP	FBti0002632
tub-GAL80[ts], UAS-egr	Iswar Hariharan
UAS-hid/CyO	Gines Morata
UAS-rpr	BDSC: 5823
en2.4-GAL4, UAS-mRPF.NLS/CyO	BDSC: 30557
Tret1-GFP	BDSC: 66367
Pdk1-GFP	BDSC: 59836
InR-eGFP	Hong Xu lab DOI: 10.7554/eLife.49309
tGPH-GFP	Yohanns Bellaiche
UAS-Akt1	BDSC: 8192
CG5535-GFP	BDSC: 64096
UAS-GFP^{S56T}	BDSC: 1521
rn$^{GAL4\text{-}DeltaS}$, tubGAL80^{ts}	BDSC: 8142, 7012
rn$^{GAL4\text{-}5}$, UAS-egr, tubP-GAL80^{ts}	Iswar Hariharan
10xStat92E-dGFP	Erica Bach PMID: 17008134
10xStat92E-GFP	Erica Bach PMID: 17008134
UAS-Stat92E.ORF.3xHA	Fly-ORF F000750 PMID: 23583758
'TRE-RFP': TRE-DsRed.T4	Dirk Bohmann PMID: 22509270
upd3.1-3-LacZ	Iswar Hariharan
UAS-dPdk1	Hugo Stocker
UAS-dPdk1(A467V)	Hugo Stocker https://doi.org/10.1073/pnas.011318098
dPdk1(5)ΔEP	Hugo Stocker lab https://doi.org/10.1073/pnas.011318098
yw, hsflp[122]; hs-p65::zip, lexAOp-egrNI /CyO-GFP; salm-zip::LexADBD, Dve>stop>GAL4/TM6c	Robin Harris PMID: 32490812
UAS-Pdk1-RNAi	BDSC: 27725 (Fig.5L, M: Fig. S5G: FigS6.F, G)
UAS-Pdk1-RNAi	BDSC: 34936 (used additionally to validate *Pdk1-GFP* line, BDSC: 59836)
UAS-Pdk1-RNAi	BDSC: 36071 (used additionally to validate *Pdk1-GFP* line, BDSC: 59836)
UAS-stat92E RNAi	BDSC: 33637
stat 92E [85c9]	Erica Bach
UAS-Ras^{V12}, scrib-RNAi	FBtp0001705, VDRC: 105412
ubxFLP; FRT42D ubi-mRFP	FBti0150334, FBti0147338

FRT42D Psc-Su(z)2[XL26]	Rongwen Xi PMID: 20439432
w^{1118}	

Table S2 Immunohistochemistry reagents

Reagent	Source	
Mouse polyclonal anti-β-Galactosidase (1:1000)	Promega	Cat. #: Z3782
Mouse monoclonal anti-MMP-1 (1:30)	Developmental Studies Hybridoma Bank	Cat. #: 3A6B4
Mouse monoclonal anti-MMP-1 (1:30)	Developmental Studies Hybridoma Bank	Cat. #: 3B8D12
Mouse monoclonal anti-MMP-1 (1:30)	Developmental Studies Hybridoma Bank	Cat. #: 5H7B11
Mouse monoclonal anti-Nubbin (1:100)	Developmental Studies Hybridoma Bank	Cat. #: 2D4
Rat monoclonal anti-elav (1:50)	Developmental Studies Hybridoma Bank	Cat. #: 7E8A10
Rabbit polyclonal anti-CG1139 (1:200)	Susumu Hirabayashi, Imperial College London Faculty of Medicine.	https://pubmed.ncbi.nlm.nih.gov/32938923/
Rabbit polyclonal anti-p-AKT (S505) (1:500)	Cell Signaling	Cat. #: 4084s
Rabbit polyclonal anti-p-AKT (S473) (1:500)	Cell Signaling	Cat. #: 4060s
Rabbit polyclonal anti-AKT (1:500)	Cell Signaling	Cat. #: 9272s
Rat monoclonal anti-RFP (1:1000)	Chromotek	Cat. #: 5F8
Rabbit polyclonal anti-Drosophila p-S6 (1:200)	Aurelio Telemann, DKFZ	https://doi.org/10.1016/j.devcel.2017.07.019
Rabbit polyclonal anti-Ref(2)p	Abcam	Cat. #: Ab178440
Rabbit anti-cleaved Dcp-1	Cell Signaling	Cat. #: 9578s
Rabbit monoclonal anti-GFP	Invitrogen	Cat. #: G10362
Goat anti-mouse IgG Alexa Flour 488	Invitrogen	Cat. #: A-11001
Goat anti-rabbit IgG Alexa Flour 488	Invitrogen	Cat. #: A-11008
Goat anti-mouse IgG Alexa Flour 555	Invitrogen	Cat. #: A-21422
Goat anti-rat IgG Alexa Flour 555	Invitrogen	Cat. #: A-21434
Goat anti-mouse Alexa Flour 647	Invitrogen	Cat. #: A-21235
Goat anti-rabbit Alexa Flour 647	Invitrogen	Cat. #: A-21244
HRP-conjugated anti-rabbit IgG	Promega	Cat. #: W4011
Click-iT Plus EdU Alexa Fluor 647 Imaging Kit	Invitrogen	Cat. #: C10340
Phalloidin 488	Invitrogen	Cat #: A12379
Phalloidin 647	Invitrogen	Cat #: A22287
DAPI	Sigma Aldrich	Cat #: D9564
CellEvent Senescence Green Detection Kit	Invitrogen	Cat. #: C10850
Rapamycin	Thermo Fisher Scientific	Cat. #: J62473.MC
Click-iT Plus OPP Alexa Fluor 647 Imaging Kit	Invitrogen	Cat. #: C10458
Leptomycin	Sigma-Aldrich	Cat. #: L2913
Nile Red	Invitrogen	Cat. #: N1142
Trichlormethan/ Chloroform	Roth	Cat. #: 7331.2
2-Propanol	Merck	CAS-Nr. 67-63-0
TRIzol™ Reagent	Thermo Fisher	Cat. #: 15596026

Random Hexamer Primer	Thermo Fisher	Cat. #: N8080127
DNase I, RNase-free	Thermo Fisher	Cat. #: ENO521
RevertAid Reverse Transcriptase	Thermo Fisher	Cat. #: EP0441
RiboLock RNase Inhibitor	Thermo Fisher	Cat. #: EO0381
dNTP-Set	Thermo Fisher	Cat. #: R0182
Blue S'Green qPCR Kit Separate ROX	Biozym	Art. #: 331416
TLC Silica gel 60, 50 Glass plates 10 x 20 cm	Merck	Cat. #: 10526
Methanol	Roth	Art. #: 8388.6
n-Hexan	Roth	Art. #: 7339.1
Diethylether	Roth	Art. #: 5920.2
Sulfuric acid	Sigma-Aldrich	Art.#: 339741
Ammonium heptamolybdate tetrahydrate	Merck	Cat. #: 101180
Cerium (IV) sulfate hydrate, complex	Sigma-Aldrich	Art.#: 945512345
2-Mercaptoethanol	Sigma Aldrich	Art.#:M6250
Mini-PROTEAN TGX gels	Bio-Rad	Cat. #: 4561083
Turbo Midi 0.2 µM Nitrocellulose Transfer Packs	Bio-Rad	Cat. #: 1704159
Bio-Rad Trans-Blot Turbo Transfer System	Bio-Rad	Cat. #: 1704150
SuperSignal West Femto Maximum Sensitivity Substrate	Thermo Fisher	Cat. #: 34095